Spring 1-1-2011

Impact of Atmospheric Intraseasonal Oscillations on Multi-Timescale Variability in the Upper Indian Ocean

Benet Elizabeth Duncan
University of Colorado at Boulder, benet.duncan@colorado.edu

Impact of Atmospheric Intraseasonal Oscillations on Multi-Timescale Variability in the Upper Indian Ocean

by

Benét Elizabeth Duncan

B.S., University of California Davis, 2005

M.S., University of Colorado Boulder, 2011

A thesis submitted to the

Faculty of the Graduate School of the

University of Colorado in partial fulfillment

of the requirements for the degree of

Doctor of Philosophy

Department of Atmospheric and Oceanic Sciences

2011

This thesis entitled:
Impact of Atmospheric Intraseasonal Oscillations on Multi-Timescale Variability in the Upper Indian Ocean
written by Benét Elizabeth Duncan
has been approved for the Department of Atmospheric and Oceanic Sciences

_____

Dr. Weiqing Han

_____

Dr. Baylor Fox-Kemper

Date _____

The final copy of this thesis has been examined by the signatories, and we find that both the content and the form meet acceptable presentation standards of scholarly work in the above mentioned discipline.

Duncan, Benét Elizabeth (Ph.D., Atmospheric and Oceanic Science)

Impact of Atmospheric Intraseasonal Oscillations on Multi-Timescale Variability in the Upper Indian Ocean

Thesis directed by Associate Professor Dr. Weiqing Han

An ocean general circulation model (the Hybrid Coordinate Ocean Model, HYCOM) is used to examine the impact of atmospheric intraseasonal oscillations (ISOs) on intraseasonal sea surface temperature (SST) during boreal summer, and on seasonal to interannual SST, mixed layer thickness (hm) and upper ocean heat content (uoheat) in the Indian Ocean (IO).

In evaluating the intraseasonal SST impacts of atmospheric ISOs, the effects of the Madden-Julian Oscillation (MJO; 30-90 days) and submonthly ISOs are separately examined. The maximum summertime SST variability occurs in the Arabian Sea, the Bay of Bengal, and the eastern equatorial IO. Intraseasonal wind has a much larger impact on intraseasonal SSTs than either shortwave radiation or precipitation. Surface turbulent heat fluxes (THF) and entrainment due to changing intraseasonal wind speeds have a larger impact on SSTs than upwelling or horizontal advection due to changing intraseasonal wind stress in the Arabian Sea and in the Bay of Bengal, while the impacts of wind speed and wind stress are relatively equal in the eastern equatorial IO.

Existing studies have shown that ISOs rectify onto low-frequency equatorial surface currents and cross-equatorial transport, suggesting that they may also have important impacts on low-frequency upper ocean variability. Results indicate that rectification of ISOs onto seasonal and interannual upper ocean variability can be significant, and that it is highly regional. The regions displaying maximum rectification vary between SST, hm, and uoheat, and between seasonal and interannual timescales. Intraseasonal wind speed and wind stress have a much larger impact on seasonal and interannual SST, hm, and uoheat than either intraseasonal shortwave radiation or precipitation. The relative importance of entrainment and THF due to intraseasonal wind speed, and of upwelling and horizontal advection due to intraseasonal wind stress, varies by region.

Dedication

To my family and friends, whom I can never thank enough.

Acknowledgements

My experience in graduate school has been greatly shaped by my advisor, Dr. Weiqing Han. I am so lucky to have benefited from the guidance of such a strong female scientist, and her generosity, patience, and honesty all helped me to become the strongest scientist that I can be. Acknowledgement also goes the members of my thesis committee: Dr. Baylor Fox-Kemper, Dr. Lakshmi Kantha, Dr. Bill Large, and Dr. Ralph Milliff. They have always been willing to share their expertise, and their questions always improve my work. Fellow members of Dr. Han's research group, Laurie Trenary, Jih-Wang Wang, and Wei Yu, have all been so honest in their feedback and happy to share their knowledge, and my work and graduate school experience have benefited from it.

My family and friends continue to support me, encourage me, and lift me to be the best person that I can be. I would be nowhere without the incredible support system that they form, and I love and appreciate them more than I can ever fully express.

Funding for this work was provided by the National Science Foundation grant OCE-0452917, and by the NASA Ocean Vector Wind Science Team award 1283568. The Argo data used in this thesis were collected and made freely available by the International Argo Project and the national programs that contribute to it (http://www.argo.ucsd.edu; http://argo.jcommops.org). Argo is a pilot program of the Global Ocean Observing System. I also thank ECMWF and NCAR for the ERA-40 fields used in this work, the NOAA-CIRES Climate Diagnostics Center for CMAP precipitation, Yuanchong Zhang for ISCCP flux data, and W. Timothy Liu for preparing the QuickSCAT wind fields. QuikScat data are produced by Remote Sensing Systems and sponsored by the NASA Ocean Vector Winds Science Team. Data are available at www.remss.com.

Contents

Chapter

Tables

Table

Figures

Figure

Chapter 1

Introduction

The Indian Ocean (IO) is unique among world oceans because its unusual geography and strong seasonal winds result in circulation patterns that are quite different from those found in the Atlantic and Pacific Oceans. Historically, geographical logistics have prevented it from being as widely studied as the other major world oceans, which led to a lack of observations that has significantly improved in the last decade. Ocean, atmosphere, and coupled global circulation models (GCMs) are valuable tools to help interpret the observations and study the dynamics of variability in the IO.

1.1 Indian Ocean Geography and Wind Circulation

Because the IO is bounded by land to the north of 25°N, heat cannot travel northward beyond that latitude. Unlike the Atlantic and Pacific Oceans, the IO has a permeable eastern boundary at the Indonesian Throughflow (ITF) region. An estimated mean of 10Sv of Pacific Ocean water enters the IO through the ITF, with a peak during June and July, and a minimum during February [Gordon, 2005; Schott et al., 2009].

Circulation in the north IO is dominated by seasonally reversing monsoon winds that are shown in Figure 1.1. During the Indian summer monsoon season from May through September, winds in the northern hemisphere travel from the southwest to the northeast in the Arabian Sea (Figure 1.1b). The strong southwest monsoon winds result in increased upwelling of cool subsurface waters along the northwest coast of the IO, which in turn cause strong sea surface temperature

(SST) cooling in the region (Figure 1.2b). Winds reverse to northeasterlies during the winter monsoon season from November through March (Figure 1.1d). Under the strong seasonally reversing monsoon wind forcing, the upper IO circulation has a strong annual cycle (Figures 1.3 and 1.4). Typical patterns of IO currents are shown for the summer (July and August) and winter (January and February) monsoon seasons in Figures 1.3 and 1.4, respectively. The Somali Current is a seasonally reversing western boundary current that flows meridionally along the northeast coast of Africa. During the peak months of the summer monsoon season, the Somali Current flows from south to north before turning offshore to the east near 4°N. It reverses to flow southward from 10°N to 4°S during the peak months of the northeast winter monsoon season.

During the monsoon transition seasons, in late spring (April-May) and fall (October-November), winds along the equator are westerlies, and they drive the eastward spring and fall Wyrtki Jets [O'Brien and Hurlburt, 1974; Han et al., 1999]. These jets are believed to be important sources of low frequency eastward mass transport in the IO, bringing warm surface water eastward from the African coast to the Sumatran coast [Wyrtki, 1973; Nagura and McPhaden, 2010]. Associated with this mass transport are measurable increases in sea level off the coast of Sumatra, and decreases near Africa [Wyrtki, 1973].

Different from the Pacific and Atlantic Oceans, annual mean winds along the IO equator are westerlies, with easterly winds occurring only during winter (December-February). The mean equatorial westerlies, together with the southeasterly trade winds, cause negative wind stress curl and positive Ekman pumping velocities, which drive mean open ocean upwelling in the southwest tropical IO [Woodberry et al., 1989; McCreary et al., 1993; Donguy and Meyers, 1995; Masumoto and Meyers, 1998; Hermes and Reason, 2008, and references therein]. This mean upwelling zone is referred to as the Thermocline Ridge of the IO and is suggested to be climatically important [e.g. Goddard and Graham, 1999; Webster et al., 1999; Murtugudde et al., 2000; Harrison and Vecchi, 2001; Annamalai et al., 2005; Saji et al., 2006; Han et al., 2007; Hermes and Reason, 2008; Halkides and Lee, 2011, and references therein].

The South Equatorial Current and the South Equatorial Countercurrent are both found year-

Figure 1.1: Seasonal wind patterns in the Indian Ocean (IO), calculated from monthly climatologies of QuickSCAT wind data. Shading indicates wind speed, while vectors indicate wind speeds and strength of wind stress. Units are in ms^{-1} for wind speed and dyn cm^{-2} for wind stress.

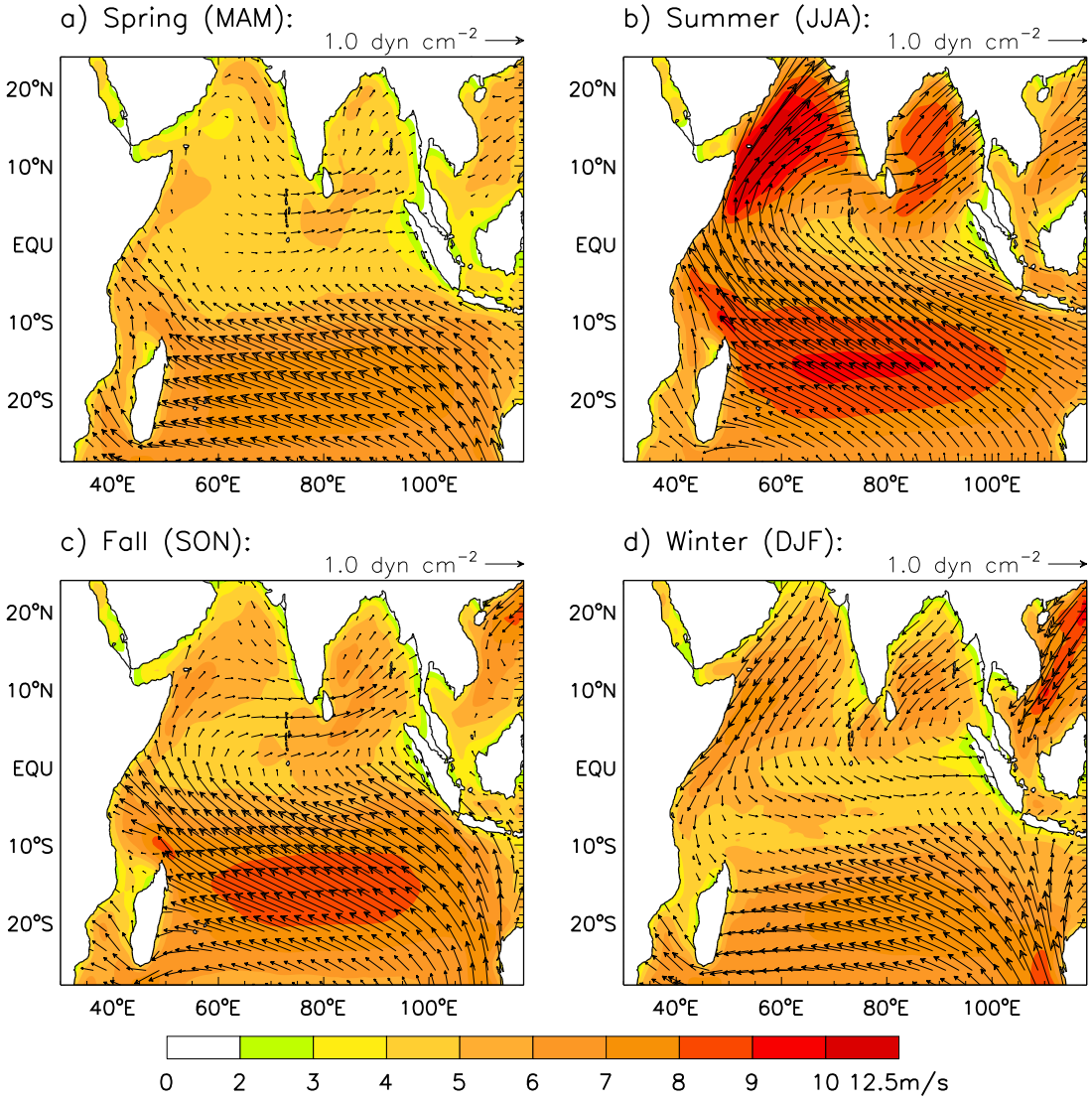

Figure 1.2: Seasonal sea surface temperature (SST) patterns in the IO, calculated from monthly climatologies of TRMMv4 2.5° × 2.5° SST data. Units are °C.

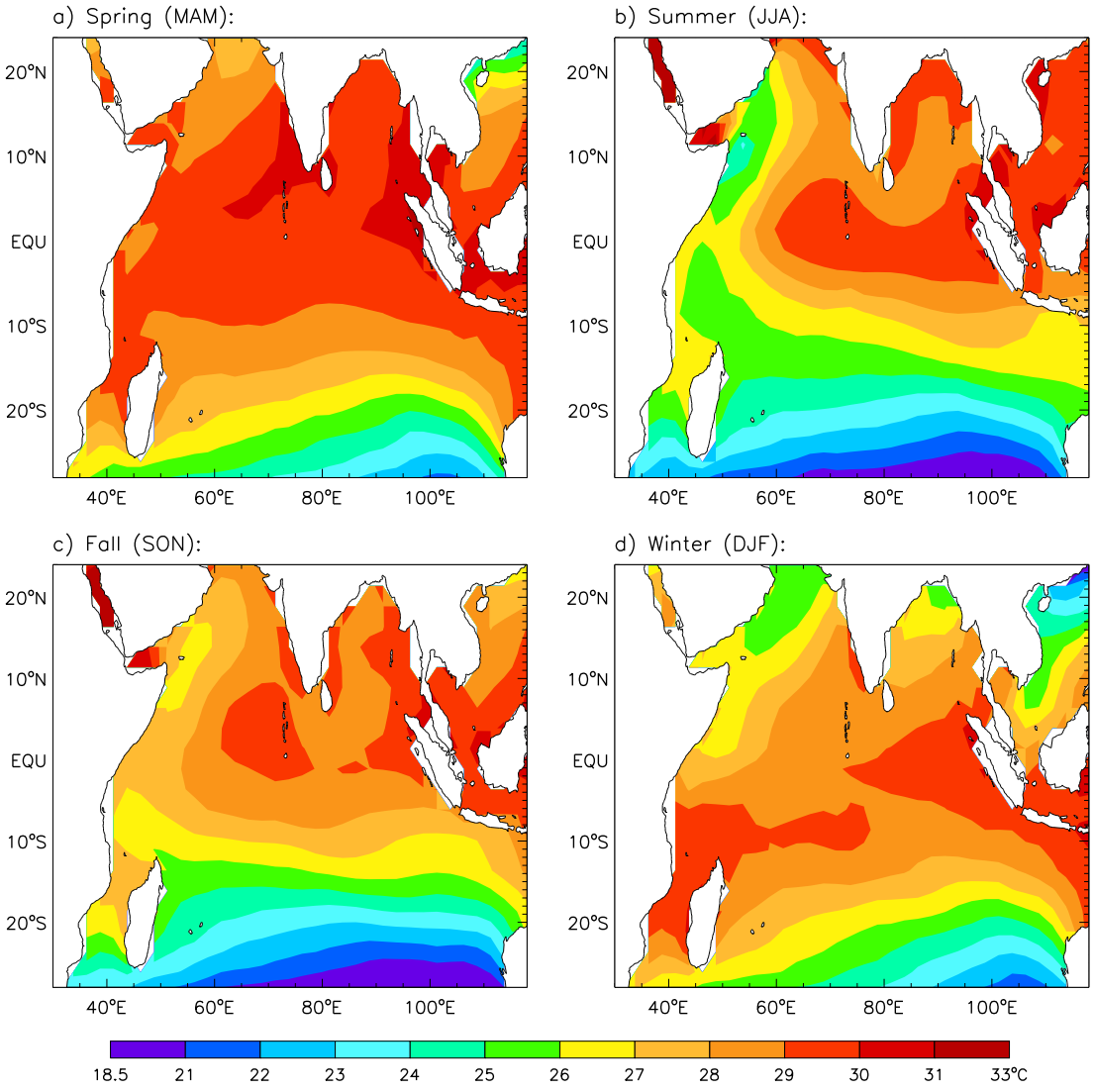

Figure 1.3: Current branches (blue and purple arrows), upwelling (green arrows), and meridional Ekman transports (red arrows) in the IO during the peak summer monsoon months (July-August). Figure from Schott et al. [2009].

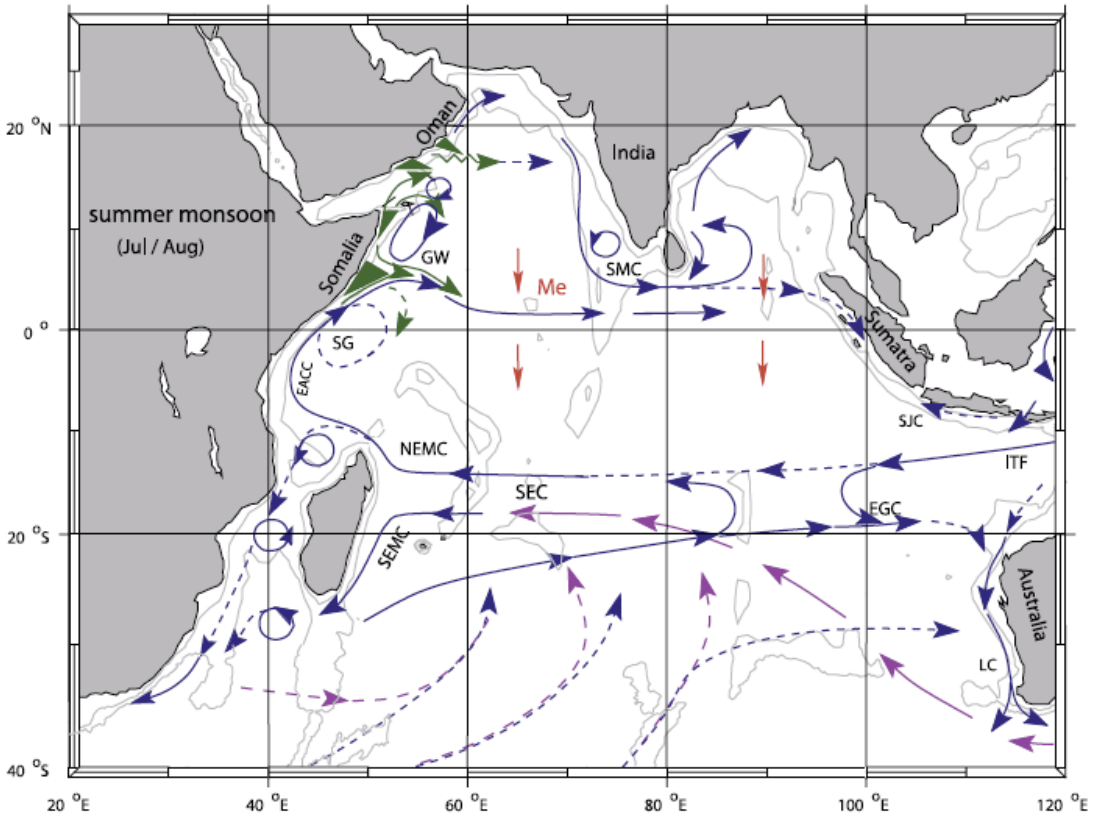

Figure 1.4: Current branches (blue and purple arrows) and meridional Ekman transports (red arrows) in the IO during the peak winter monsoon months (January-February). Figure from Schott et al. [2009].

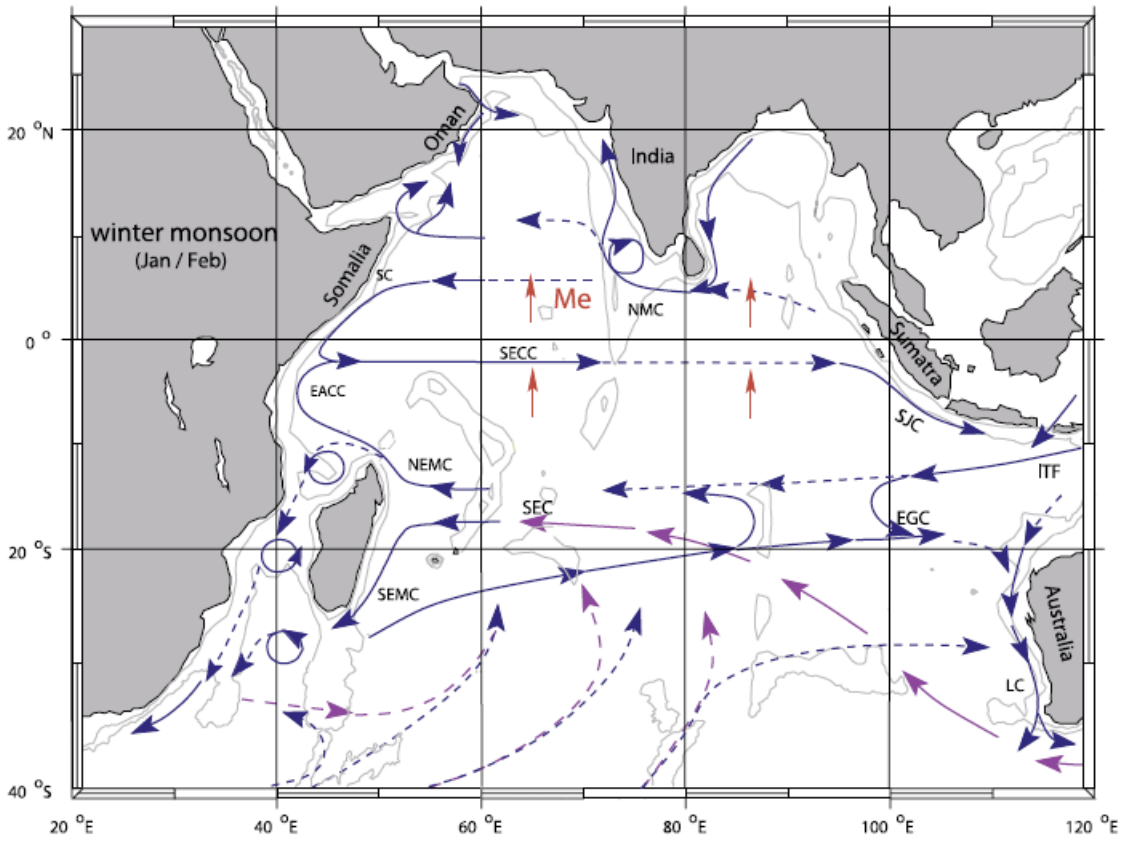

round. Located to the south of 8S, the South Equatorial Current is strongest during the summer monsoon season. The South Equatorial Countercurrent is located just to the south of the equator, and it shifts from a surface to a subsurface current during the summer monsoon. The Agulhas Current is a strong western boundary current in the southern IO, and it is suggested to be a major connection between the IO and the Atlantic Ocean and an important part of global thermohaline circulation.

1.2 Introduction to Atmospheric Intraseasonal Oscillations (ISOs)

Atmospheric variability on a range of timescales interacts with these seasonal background wind and ocean circulation patterns to establish much of the climate observed in the IO. Of particular interest are atmospheric intraseasonal oscillations (ISOs), which are oscillating modes of wind and convection with periods that range from 10-90 days. ISOs are often subdivided into longer-timescale variability (30-90 days), which is dominated by the Madden-Julian Oscillation (MJO) [Madden and Julian, 1971, 1972, 1994], and short timescale submonthly variability (10-30 days), which is dominated by the Quasi-Biweekly Mode (QBM) [Kiladis and Weickmann, 1997; Chatterjee and Goswami, 2004]. Wang and Xie [1997] noted that boreal summer ISOs are weaker than those in winter, with an oscillation period of about 35 days (versus 50 days in winter), and with more frequent north and northwestward propagation. The MJO travels as a series of active and break convection cells superimposed on a coupled Kelvin-Rossby wave packet with global zonal wave numbers 1-3 [Hendon and Salby, 1996; Wang and Xie, 1997]. These convection cells develop over the central equatorial IO before propagating eastward and northward (southward) across the IO and the Pacific Ocean during boreal summer (winter) [Li and Wang, 1994; Wang and Xie, 1997; Webster et al., 2002].

On submonthly (10-30 day) timescales, ISOs are dominated by convectively coupled, equatorially trapped Kelvin and Rossby waves with global zonal wave numbers 5 and 6 [Kiladis and Weickmann, 1997], a zonal wavelength of approximately 6000km, and a westward zonal speed of $4.5ms^{-1}$ [Wheeler and Kiladis, 1999; Chatterjee and Goswami, 2004]. The QBM propagates west-

ward [Murakami and Frydrych, 1974; Chen and Chen, 1993; Numaguti, 1995], and it is suggested to be a convectively coupled, first meridional mode Rossby wave that is displaced by the mean flow northward (southward) by about 5° during summer (winter) [Chatterjee and Goswami, 2004]. The QBM is strongest over the Indian Ocean and the west Pacific warm pool during summer, and over the central and western Pacific during winter [Chatterjee and Goswami, 2004]. Many submonthly ISOs are generated over the northern Bay of Bengal (BOB) during the summer monsoon [Bhat et al., 2001]. At the beginning of QBM events, the west-central IO and northern BOB warm, while the east equatorial IO and south BOB cool. This pattern slowly reverses over the course of an event. In contrast, MJO events cause basin-wide warming before events and cooling after [Schiller and Godfrey, 2003; Han et al., 2007].

Several observational and modeling studies have compared submonthly and MJO-scale atmospheric ISOs. Vincent et al. [1998] analyzed data from 20 years of the ISO record (July 1974 - April 1994) to identify the interannual cycles and variability of high and low frequency variations. Summertime (JJA) submonthly convective events had an all-season maximum over the northern BOB, while the MJO-timescale maximum was located 15° to the south of the BOB. In contrast, the winter season (DJF) MJO maximum was in the eastern IO. The same study also found that during seasons when the MJO-scale signal was weaker than normal, the submonthly events had uncharacteristically large power, and vice versa [Vincent et al., 1998]. Results from the Bay of Bengal Monsoon Experiment (BOBMEX) showed that convection and winds on submonthly timescales are much stronger than those of the MJO [Bhat et al., 2001]. This led Bhat et al. to speculate that submonthly ISOs could have a larger impact on SSTs than the MJO in the IO. A study using satellite and in situ observations with an OGCM found that the SST response forced by MJOs is stronger than that forced by submonthly ISOs [Han et al., 2007]. The authors suggested that it is the duration, rather than the strength, of atmospheric forcing that determines its impact on the SST. The weaker MJO forcing acts on the IO for a longer period of time than the stronger submonthly forcing, which allows MJOs to have a larger impact on SSTs.

1.3 Impacts of Atmospheric ISOs

Because both the QBM and the MJO travel northward (southward) during boreal (austral) summer, it is not a stretch to imagine that they might impact the summer monsoon seasons in both hemispheres. In fact, a number of studies have suggested that the timing and phase of the QBM and the MJO together determine the amplitude and phase of the wet and dry spells of the Indian, Asian, and Australian summer monsoons [Sikka and Gadgil, 1980; Yasunari, 1981; Krishnamurti and Subrahmanyam, 1982; Webster, 1983; Chen and Chen, 1993; Chatterjee and Goswami, 2004]. The monsoon rains can have profound impacts on affected regions. For example, 70-80% of the Indian subcontinent's annual rainfall occurs during the Indian summer monsoon [Ashok et al., 2001; Gadgil et al., 2004; Kumar et al., 2004], and the timing of crop planting depends on accurate predictions of the timing of the monsoon rains [Selvaraju, 2003; Kumar et al., 2004]. Improved understanding of the impacts of the QBM and the MJO on the IO can help with improved modeling and prediction of these monsoon rains.

Atmospheric ISOs, especially the MJO, have also been shown to impact the timing, formation, strength, and termination of low frequency El Nino Southern Oscillation (ENSO) [Luther et al., 1983; Lau and Chan, 1985, 1988; Kessler et al., 1995; Moore and Kleeman, 1999; Takayabu et al., 1999; Kessler and Kleeman, 2000; Zavala-Garay et al., 2005] and Indian Ocean Dipole (IOD) events [Saji et al., 1999; Webster et al., 1999; Murtugudde et al., 2000; Yu and Rienecker, 2000; Rao and Yamagata, 2004; Han et al., 2006b; Rao et al., 2009]. Studies of 40-50 day variability in observed outgoing longwave radiation (OLR) revealed that the 1982-1983 El Nino event was preceded by MJO events that may have triggered and then amplified its development [Lau and Chan, 1985, 1988]. A study of ENSO using a coupled ocean-atmosphere GCM showed that MJO-induced westerly and easterly wind bursts in the tropical west Pacific Ocean may contribute to the triggering and development of El Nino events [Moore and Kleeman, 1999]. Another OGCM study showed that including MJO-forced low frequency SST patterns improved the modeled strength of an El Nino event [Kessler and Kleeman, 2000].

The IOD is a coupled ocean-atmosphere mode of variability at interannual timescales that has large and widespread impacts on convection and precipitation in the IO and beyond. Figure 1.5 shows the typical evolution of an IOD event. During a positive (negative) IOD event, SSTs are anomalously warm (cool) in the west (east) IO, which leads to increased (decreased) convection and precipitation in the west (east) IO. Positive IOD years typically begin to develop and grow in May and June, peak in October, and decay and end in December [Saji et al., 1999; Webster et al., 1999]. A number of studies have shown that the zonal wind, convection, and wave structure associated with MJOs is the most likely source of their impacts on the IOD [Yu and Rienecker, 2000; Rao and Yamagata, 2004; Han et al., 2006b]. During positive dipole years, the intensity of submonthly variability is greatly reduced, while submonthly convection is active in the southeast Indian Ocean during negative dipole years [Shinoda and Han, 2005]. This region of convection corresponds with the location of the maximum convergence of moist air associated with negative IOD events. Shinoda and Han [2005] found that the equatorial westerlies generated by cyclonic circulation in the southeast IO can cause an increase in sea level, and thus downwelling, in the region. These processes can then enhance the warm SSTs in the area and provide a positive feedback during negative IOD years. Providing further evidence of an ISO-IOD connection, the termination of pure IOD events dating from the 1960s (which do not co-occur with El Nino events) consistently coincides with the presence of MJO events [Rao and Yamagata, 2004; Han et al., 2006b; Rao et al., 2009].

1.4 Air-Sea Interactions and ISOs: Current Knowledge

Given the important connections between ISOs, the summer monsoons, ENSO, and the IOD, improved simulation of ISOs in coupled and atmospheric climate models is needed [Slingo et al., 1996; Sperber et al., 2005; Lin et al., 2006; Kim et al., 2010; Klingaman et al., 2011]. ISO propagation can be greatly affected by air-sea interactions over the IO [Flatau et al., 1997; Wang and Xie, 1998; Waliser et al., 1999; Kemball-Cook and Wang, 2001; Woolnough et al., 2001; Fu et al., 2003; Inness and Slingo, 2003; Sperber et al., 2005]. For example, Fu et al. [2003] used a cou-

Figure 1.5: Winds (bold filled arrows), SSTs (shading), convection, Ekman transport, and cross-section vertical structures associated with the Indian Ocean Dipole (IOD) event during (a) Summer 1997, (b) Autumn 1997, (c) Autumn-Winter 1997, and (d) Summer 1998. In (a), bold arrows E and F represent the climatological winds, and G and H represent the observed winds. Figure from Webster et al. [1999].

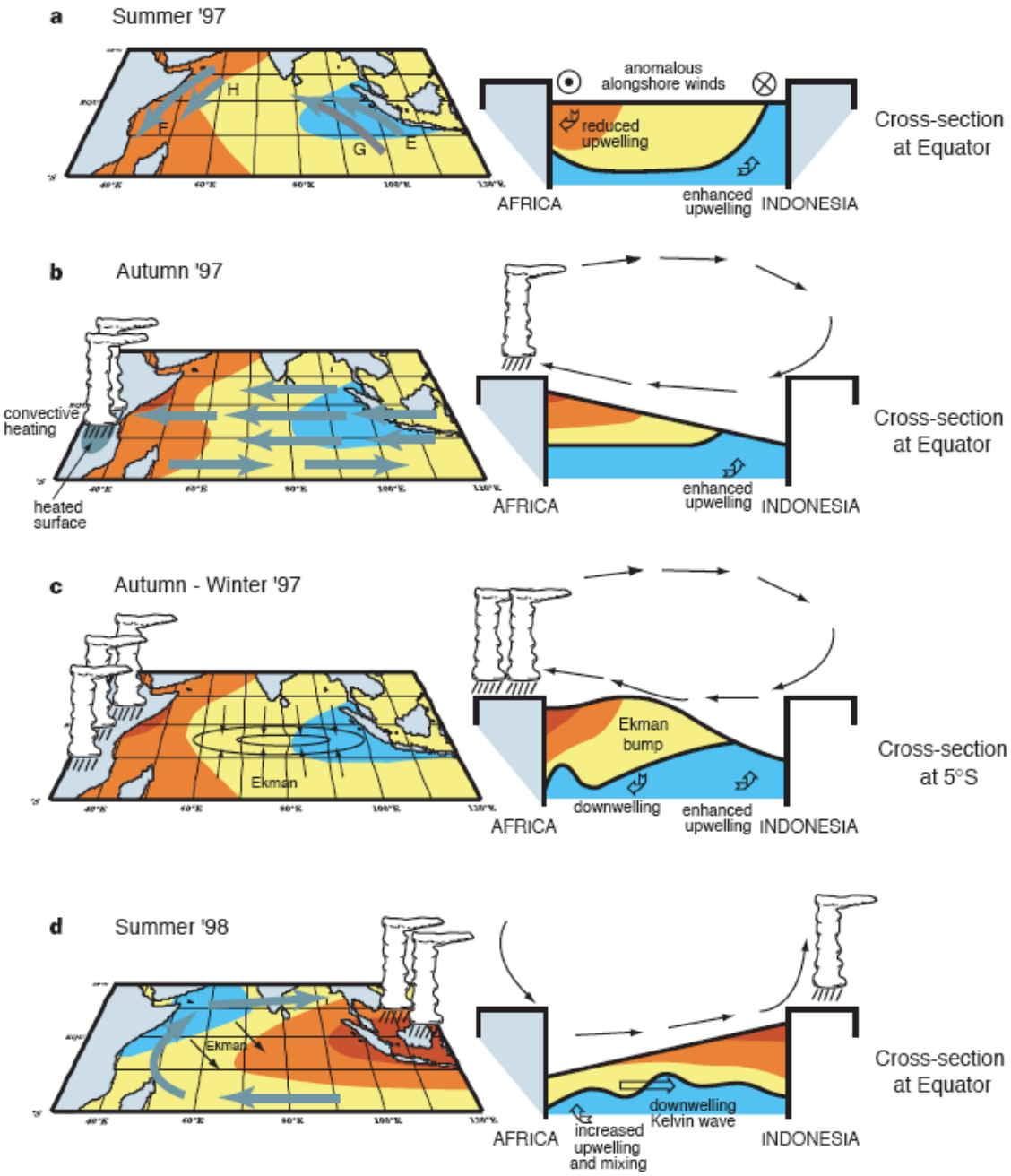

pled atmosphere-ocean model to perform experiments with and without air-sea interactions. The authors found that northward ISO propagation was not well simulated when the interactions were not allowed. When air-sea interactions were allowed, the northward propagation of modeled ISOs was much improved. Increased understanding of these air-sea interactions, which connect atmospheric ISOs to intraseasonal (high frequency) and seasonal-to-interannual (low frequency) ocean responses, is greatly needed.

1.4.1 Intraseasonal Ocean Response to ISOs

Extensive research evaluating intraseasonal SST variability exists, but these studies have divergent conclusions about the processes that control this variability [McPhaden, 1982; Krishnamurti et al., 1988; Hendon and Glick, 1997; Jones et al., 1998; Shinoda and Hendon, 1998; Shinoda et al., 1998; Woolnough et al., 2000; Harrison and Vecchi, 2001; Sengupta et al., 2001; Schiller and Godfrey, 2003; Waliser et al., 2003, 2004; Duvel et al., 2004; Kessler, 2005; Han et al., 2006a; Saji et al., 2006; Han et al., 2007]. In an early study, Krishnamurti et al. [1988] used global experiment heat flux and daily SST, together with two 10-day averaged SST observations, to study MJO-scale moisture and heat fluxes in the IO. The authors found that zonal wind oscillations dominated moisture and heat fluxes in the BOB, Arabian Sea, and west Pacific Ocean, while surface humidity fluxes were not important in most regions. In addition, air temperature fluctuations did not have a large impact on sensible heat fluxes anywhere except the Arabian Sea.

Increasing interest in Indian Ocean ISOs has exposed the need for more oceanic observational data in the region. In response to this information gap, field experiments have been launched, particularly in the east IO. Two such experiments are the Bay of Bengal Monsoon Experiment (BOBMEX) [Bhat et al., 2001] and the Joint Air-Sea Monsoon Experiment (JASMINE) [Webster et al., 2002]. Both studies were implemented during the boreal spring-summer monsoon season in 1999, and they recorded oceanic and atmospheric variables that included radiative and latent heat fluxes, SST, wind speed, and OLR. Both noted coherent patterns in the evolution of atmospheric ISOs and SST, with OLR leading SST changes on the scale of days [Bhat et al., 2001; Webster

et al., 2002].

More recent satellite observation-based studies have also examined the processes that dominate intraseasonal SST variability. Sengupta et al. [2001] used Tropical Rainfall Measuring Mission (TRMM) data to find that net surface heat fluxes cause SST changes during boreal summer in the central and eastern tropical IO, and in the open South China Sea. Boreal winter SST cooling events mostly occur due to decreased solar radiation associated with increased convection, and due to the effect of increased wind anomalies on turbulent heat fluxes and ocean mixing [Saji et al., 2006]. In another study of boreal winter, TRMM Microwave Imager (TRMM-TMI) observed ISOs were analyzed, and the rapid rate of SST change associated with a cooling event in the region from 10°S-EQ, 75°E-95°E could not be fully explained by air-sea fluxes [Harrison and Vecchi, 2001]. This led the authors to suggest that changes in vertical mixing, entrainment, or Ekman suction contributed to the cooling there.

Data analysis techniques have been used to evaluate the processes that control the SST response to ISOs in the IO. Shinoda et al. [1998] created composites of intraseasonally filtered OLR, SST, surface heat and momentum fluxes, and freshwater flux anomalies associated with the MJO. The resulting heat flux dataset demonstrated that anomalous insolation made a slightly larger contribution to net heat flux than anomalous latent heat flux in the IO. Coherent net surface flux anomalies preceded the resulting SST anomaly by 10 days. The authors thus concluded that SST variability in the IO and the west Pacific Ocean may be driven by surface heat flux variability [Shinoda et al., 1998]. A more recent study [Woolnough et al., 2000] also used data analysis to find that intraseasonal convection, surface fluxes, and SST share a coherent relationship in the IO, the Indian subcontinent, and the west Pacific. Changing surface fluxes due to ISOs altered the period of SST changes [Woolnough et al., 2000].

In the past decade, a number of modeling studies of ISOs have sought to identify and understand the physical processes that control intraseasonal SST variability. Shinoda and Hendon [1998] used a one-dimensional mixed layer model to study MJO-scale ISOs in the tropical Indian and west Pacific Oceans. Confirming the results of Shinoda et al. [1998], the authors found that

latent heat flux changes are less important than shortwave radiative fluxes in causing SST changes in the IO. Linear horizontal advection, they concluded, is of secondary importance for SST anomalies, while freshwater flux variability has little impact on SST because of its phasing with wind stress [Shinoda and Hendon, 1998]. The presence of a barrier layer in the east IO means that mixed layer processes and surface forcing can play an even larger role in determining ISO-induced SST variations [Shinoda and Hendon, 1998; Schiller and Godfrey, 2003; Duvel et al., 2004].

Duvel et al. [2004] used an ocean general circulation model (OGCM), data analysis, and observations to evaluate the MJO during boreal winter (in January and March 1999) from 0 -10°S. In contrast with Harrison and Vecchi [2001], IO SST changes in this study were dominated by surface heat flux variations, rather than by advection or exchanges with the subsurface. These surface flux variations were, in turn, found to be due to decreasing insolation associated with increased convective cloudiness, and to increasing evaporation during westerly wind events [Duvel et al., 2004; Saji et al., 2006; Duvel and Vialard, 2007; Vialard et al., 2008]. In agreement with Woolnough et al. [2000], the authors reasoned that the phasing between convective and dynamic surface flux variability determined the anomalous SST amplitudes during ISOs.

In an OGCM study of tropical boreal spring and summer MJOs, Schiller and Godfrey [2003] found that the dominant processes controlling the composite mixed layer heat budget were, in order of descending importance: net surface heat flux, horizontal advection, and entrainment through the mixed layer base. In contrast, the authors found that the salinity budget is controlled by entrainment, surface freshwater fluxes, and horizontal advection [Schiller and Godfrey, 2003].

Waliser et al. [2003, 2004] used OGCM experiments forced with canonical MJOs to separately examine the ocean response to boreal summer and winter MJOs. As with Schiller and Godfrey [2003], the authors found that net surface heat flux was the sole major factor in SST variability during boreal summer and winter in the south-equatorial West Pacific and near the maritime continent (i.e. near Indonesia). Wind speed (via impacts on evaporation), wind stress, and cloudiness (via impacts on incoming shortwave radiation) dominated the net surface heat budget, while rainfall, cloud effects on longwave flux, and sensible heat flux were less of a factor. One signifi-

cant difference found between boreal summer and winter MJO-scale events was that entrainment variability is large during boreal summer in the Bay of Bengal. The authors found no regions of large entrainment variability in the boreal winter Indo-Pacific Oceans [Waliser et al., 2004]. These results contradict Harrison and Vecchi [2001] because they suggest that vertical entrainment is less important than meridional advective processes in altering SST [Waliser et al., 2003].

Han et al. [2007] used an OGCM to separately evaluate the impacts of boreal winter MJO (30-90 day) and submonthly (10-30 day) ISOs on intraseasonal SST in the IO. The strongest intraseasonal SST variability was found in the Intertropical Convergence Zone, due mostly to MJO-scale ISOs. The SST impacts of MJO and submonthly entrainment and turbulent heat fluxes due to wind speed, and upwelling and horizontal advection due to wind stress, were much greater than the SST changes forced by intraseasonal shortwave (SW) radiation and precipitation.

While there has clearly been a large amount of work done to determine the processes by which MJO events affect SSTs, far less attention has been paid to submonthly ISOs and their impact on SSTs. The structure and propagation of submonthly ISOs are very different than those of MJO events, and the former cannot be expected to have the same impact on SST as the latter [Han et al., 2007]. In modeling studies, Han et al. [2006a, 2007] found that submonthly ISO-induced SST changes in the Indian Ocean are strongly forced by submonthly wind speed and wind stress, with short- and long-wave radiative fluxes affecting SST in some regions for some events.

1.4.2 Seasonal-to-Interannual Ocean Response to ISOs

Much less work has been done to determine the seasonal-to-interannual ocean response to atmospheric ISOs, which largely occurs through nonlinearities in the system. Observational and OGCM studies have shown that atmospheric ISOs can have significant impacts on seasonal-to-interannual SST, mixed layer thickness (hm), zonal surface currents and heat transport in the equatorial IO and the tropical Pacific Ocean, and on meridional heat transport in the tropical IO [Kessler and Kleeman, 2000; Waliser et al., 2003, 2004; Han et al., 2004; Halkides et al., 2007]. In a modeling study forced by atmospheric ISOs from 1988-2001, Han et al. [2004] found that ISO rec-

tification onto seasonal-to-interannual zonal equatorial transport and equatorial surface currents is mostly due to nonlinear processes that include entrainment and momentum upwelling, and the mixed layer depth's asymmetric response to easterly and westerly winds. In addition, the authors found that ISOs reduce the strength of seasonal eastward Wyrtki Jets (westward surface currents) by 15-25cm/s in boreal spring and autumn (January - March). Wyrtki Jets are an important source of zonal heat transport in the IO, and changes in their strength can be important in the region. A similar modeling study found that ISO-forced seasonal and interannual meridional heat transport can be significant (up to 30% of interannual heat transport is due to ISOs), and it is mostly forced by wind processes that include turbulent heat fluxes, entrainment, and momentum upwelling [Halkides et al., 2007].

The impacts of atmospheric ISOs on seasonal-to-interannual SST, hm, and upper ocean heat content in the IO have not been extensively evaluated. In their series of papers discussed above, Waliser et al. [2003, 2004] also considered MJO rectification onto low frequency SSTs, hm, and zonal currents and transport by examining the effects of a canonical MJO. Results indicated that MJOs do rectify onto the low frequency ocean hm, SST, zonal current, and zonal heat transport. During austral summer, MJOs caused cooling of $\sim$0.15°C and hm shoaling of $\sim$4m in the IO, which was largely attributed to SW radiation and wind anomalies, although upwelling and vertical temperature gradients also contributed. The authors noted that strong SW radiation forcing co-occurs with weak wind anomalies, so the two forcings act together to shoal (thicken) the hm and increase warming (cooling) during suppressed (active) phases of the MJO. Austral summer MJOs also contributed to a zonal SST gradient in the IO, mostly due to surface heat fluxes, that occured during the same time as typical IOD growth. They hypothesized that surface heat fluxes associated with austral summer MJOs may contribute to the formation and growth of IOD events. Different from austral summer, the authors found that boreal summer MJOs can cause warming of 0.2°C and hm shoaling of 7m in the north IO, and an eastward rectified zonal equatorial current. The rectified SSTs forced by boreal summer MJOs were due mostly to SW radiation, while the rectified hm was due to nonlinear mixed layer processes, and the rectified current was most strongly due to

wind stress forcing. In agreement with Han et al. [2004], the rectified current was related to the mixed layer's asymmetric response to easterly and westerly winds. Again, the studies of Waliser et al. [2003, 2004] examined the effects of canonical MJO events. The observed, realistic MJO impacts on seasonal-to-interannual SST, hm, and upper ocean heat content have yet to be assessed.

1.5 Current Work

The divergent conclusions about the processes that control intraseasonal SST variability in the IO, combined with the lack of research about submonthly SST variability, underline the need for additional work about the intraseasonal ocean response to ISOs. There is also a clear lack of research that evaluates the presence of ISO rectification onto seasonal-to-interannual upper IO variability, and the processes that control this rectification. The existing IO SST rectification study did not use real (non-composite) atmospheric ISOs as forcing fields in an OGCM, it did not include the QBM in the ISO forcing fields, and it did not separately consider the seasonal and interannual ocean response. There is a clear need for detailed work that utilizes the best available satellite and in situ observations in combination with model simulations to evaluate the impacts of atmospheric ISOs on the intraseasonal, seasonal, and interannual variability of the upper layers of the IO, and the processes that control these impacts.

The work in this dissertation is intended to address the following gaps in the current level of knowledge about air-sea interactions between atmospheric ISOs and the upper layers of the IO:

(1) How strongly do atmospheric ISOs (the MJO and submonthly ISOs) impact the intraseasonal SST and hm in the IO during boreal summer? How do these impacts occur?

(2) Do atmospheric ISOs exhibit significant rectification onto the seasonal cycle of the upper IO? What forcing processes control this rectification?

(3) Do atmospheric ISOs rectify onto the interannual variability of the upper IO? What forcing processes control this rectification?

An OGCM, the Hybrid Coordinate Ocean Model (HYCOM), is used in combination with a number of satellite and ground-based observations to evaluate the above issues. Chapter 2 provides detailed information about HYCOM, including how some rectification processes can be estimated using the model's core equations. Unlike Chapters 3 and 4, Chapter 2 is not intended to be a stand-alone research paper. Chapter 3 focuses on evaluating Topic 1: the intraseasonal upper ocean impacts of atmospheric ISOs. Extending from Chapter 3, Chapter 4 combines Topics 2 and 3 to determine the impact of atmospheric ISOs on the seasonal cycle and interannual variability of the upper IO. Chapter 5 provides a discussion of the completed work and suggests topics for future research that extend from the results.

Chapter 2

HYCOM Introduction

2.1 General Model Overview

It is prohibitively difficult to use only observational data to evaluate the processes that control air-sea interactions between atmospheric ISOs and the upper layers of the IO, simply because regularly gridded depth profiles do not exist for the basin. Instead, the Hybrid Coordinate Ocean Model (HYCOM) [Bleck, 2002; Halliwell, 2004], an oceanic general circulation model, is used to obtain the full upper ocean response to intraseasonal atmospheric forcing. The model has been applied in studies of a wide range of regions and timescales including the Indian Ocean [Han, 2005; Han et al., 2006a,b; Yuan and Han, 2006; Han et al., 2007], the Atlantic Ocean [Han et al., 2004, 2008], the Black Sea [Kara et al., 2005a,b], the tropical Pacific Ocean [Shaji et al., 2005], and the Gulf of Mexico [Prasad and Hogan, 2007].

HYCOM utilizes terrain-following sigma coordinates in coastal regions, isopycnal coordinates in the interior open ocean, and z coordinates in weakly stratified and in very shallow waters [Bleck, 2002; Halliwell, 2004]. The isopycnal coordinates used in the interior open ocean follow lines of constant potential density (ρ_{pot}). Potential density is used because it can also be viewed as a proxy for entropy, which under adiabatic conditions reduces flow to two dimensions in (x,y,ρ_{pot}) space. In ρ_{pot} space, it is also simpler to distinguish between eddy-driven isopycnal (horizontal) stirring and diapycnal (vertical) mixing [Bleck, 2002]. HYCOM has a set of vertical mixing schemes to choose from: the K-Profile Parameterization (KPP), Mellor-Yamada 2.5, NASA-GISS, Price-Weller-Pinkel, and Krauss-Turner A, B, and C. The KPP is used in the modeling experiments

in Chapters 3 and 4, and a detailed review of this mixing scheme follows in Section 2.3. After configuring HYCOM to the IO, it is spun up using monthly mean climatologies of air temperature, specific humidity, shortwave and net radiative fluxes, precipitation, and winds that are constructed from the model forcing fields, and then a series of seven experiments is run. Details of the configuration process and the model forcing fields follow in Chapters 3 and 4. The model domain, shown in Figure 2.1, is consistent in Chapters 3 and 4, with the Persian Gulf, Red Sea, and Indonesian Throughflow (ITF) removed with a land-sea mask (Figure 2.1, black lined shading). Near the southern boundary (25°S-30°S), a 5°-wide sponge layer is applied to relax model temperature and salinity fields to Levitus and Boyer [1994] and to Levitus et al. [1994] climatology (Figure 2.1, gray lined shading). Lateral boundary forcing due to the ITF and BOB rivers is included by relaxing model temperature and salinity to Levitus data in the corresponding regions (Figure 2.1, gray lined shading). Model sensitivity is likely reduced in these relaxation regions, which may reduce model-data correlations there. The full set of experiments is detailed in Table 2.1, and the ocean responses isolated by model difference solutions are listed in Table 2.2.

Table 2.1: Hybrid Coordinate Ocean Model experiments and forcings used[a]

Experiment Number	Forcings Used
MR	All 3-day mean forcing fields: winds, fluxes, precipitation
EXP1	Low-passed (removed less than) 105 days
EXP2	Low-passed (removed less than) 30 days
EXP3	Low-passed wind stress
EXP4	Low-passed wind stress and speed
EXP5	Low-passed shortwave flux
EXP6	Low-passed precipitation

[a]Low-pass frequency is 105 days, unless otherwise noted.

For Chapters 3 and 4, the first experiment, a main run (MR), contains full 3-day mean forcing fields. At least one forcing product in the other six experiments is low-pass filtered with a Lanczos filter [Duchon, 1979] to help isolate the model response to specific timescales of forcing. In experiment 1 (EXP1), all of the forcing fields are low-pass filtered to 105 days to remove in-

Figure 2.1: HYCOM model domain. Continents are shaded in solid black and regions removed with a land-sea mask are shaded with black lines. Gray lines indicate regions where model temperature and salinity are relaxed to Levitus and Boyer [1994] and to Levitus et al. [1994] climatology.

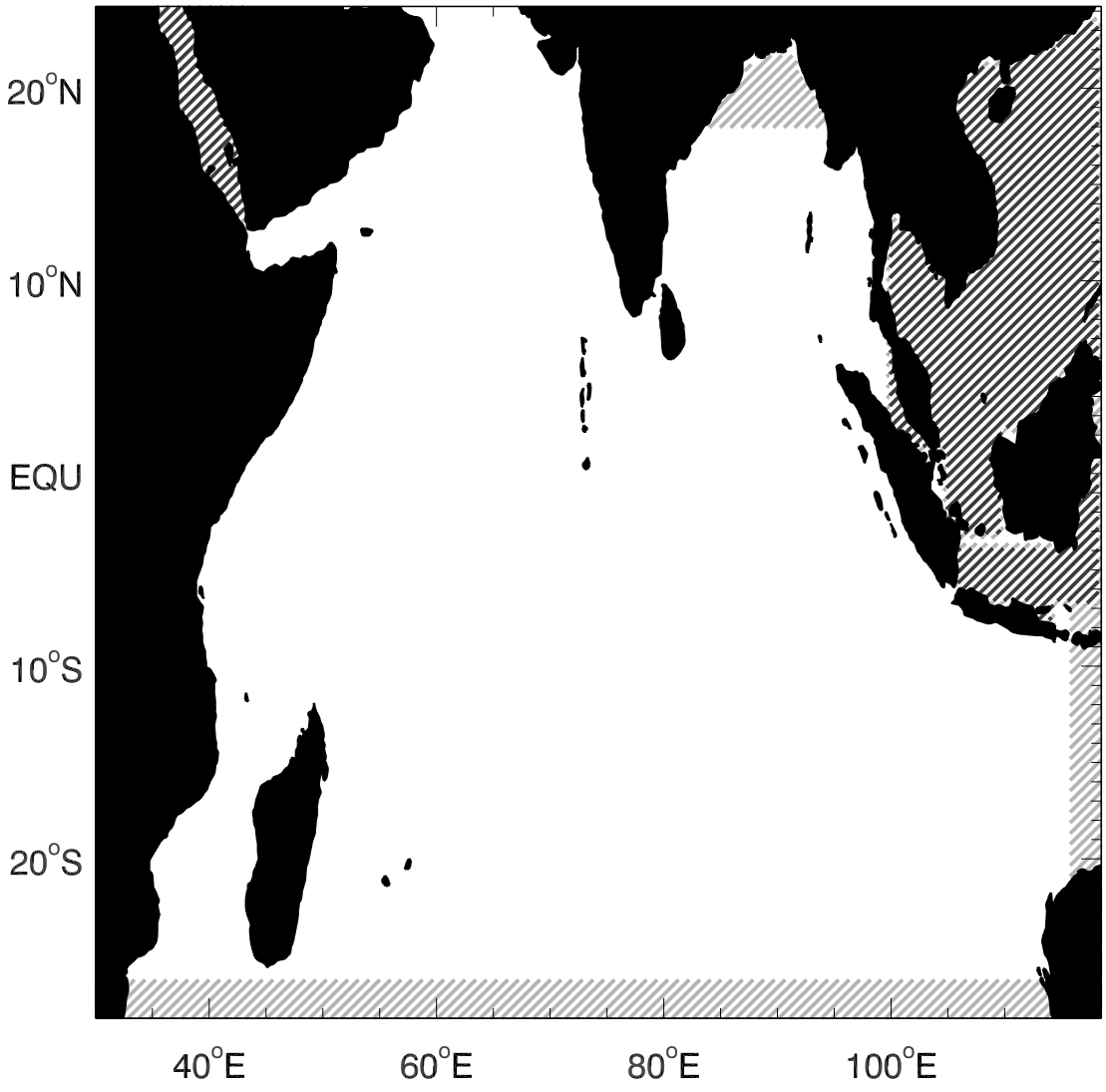

Table 2.2: Hybrid Coordinate Ocean Model difference solutions and processes isolated

Difference Solution	Isolates Ocean Response To
MR-EXP1	All intraseasonal forcing fields: winds, fluxes, precipitation
MR-EXP2	All submonthly forcing fields
EXP2-EXP1	All MJO forcing fields
MR-EXP3	Intraseasonal wind stress
MR-EXP4	Intraseasonal wind stress and speed
EXP3-EXP4	Intraseasonal wind speed
MR-EXP5	Intraseasonal shortwave flux
MR-EXP6	Intraseasonal precipitation

traseasonal periods from the data (Table 2.1). The model difference solution MR-EXP1 isolates the ocean response to ISOs (Table 2.2). Similarly, experiment 2 (EXP2) is forced with data that has been low-pass filtered to 30 days. Model difference solutions MR-EXP2 and EXP2-EXP1 isolate the ocean's response to 10-30 day and 30-105 day atmospheric variability, which are dominated by the QBM and the MJO, respectively. In experiments 3 and 4 (EXP3 and EXP4), all forcing fields are left unfiltered with the exception of wind stress and total wind (wind stress and speed), respectively, which are low-pass filtered to 105 days. EXP3, then, excludes the effects of intraseasonal Ekman convergence and divergence (which causes downwelling and upwelling), vertical current shear (which affects mixing), and horizontal advection due to wind stress. EXP4 excludes the above processes in addition to intraseasonal wind speed, which can affect the SST via turbulent heat fluxes (THF) and entrainment cooling in the model. Further discussion about the representation of these processes in the model code follows in Sections 2.2, 2.3, 2.5, and 2.6. Experiment 5 (EXP5) is forced by low-passed 105 day shortwave (SW) flux, and Experiment 6 (EXP6) is forced by low-passed 105 day precipitation. The difference solutions MR-EXP3, MR-EXP4, EXP3-EXP4, MR-EXP5, and MR-EXP6 isolate the ocean's response to intraseasonal wind stress, wind stress plus speed, wind speed, SW radiation, and precipitation, respectively.

Note that this approach assumes that the oceanic responses to different forcing fields do not interact. In reality, they may interact due to the nonlinearity of the system, and thus the sum of the oceanic responses to individual forcing fields may not exactly equal the response to the total forcing fields. These nonlinear effects, however, are apparent in specific regions such as the Somali coast [e.g. Han et al., 2007; Duncan and Han, 2009]. Consequently, the approach of separating the forcing and processes is generally valid and essential for an in-depth understanding of the processes that control air-sea interactions.

2.2 Governing Model Equations

HYCOM contains five core prognostic equations: two momentum equations, a continuity equation, and two conservation equations [Bleck, 2002]. They are:

$$\underbrace{\frac{\partial}{\partial t_s}\left(\frac{\partial p}{\partial s}\right)}_{A}+\underbrace{\nabla\cdot\left(\vec{v}\frac{\partial p}{\partial s}\right)}_{B}+\underbrace{\frac{\partial}{\partial s}\left(\dot{s}\frac{\partial p}{\partial s}\right)}_{C}=0 \tag{2.1}$$

$$\underbrace{\frac{\partial\vec{v}}{\partial t_s}}_{A}+\underbrace{\nabla_s\frac{\vec{v}^2}{2}}_{B}+\underbrace{(\xi+f)\,\vec{k}\times\vec{v}}_{C}+\underbrace{\left(\dot{s}\frac{\partial p}{\partial s}\right)\frac{\partial\vec{v}}{\partial p}}_{D}+\underbrace{\nabla_s M-p\nabla_s\alpha}_{E}=\underbrace{-g\frac{\partial\vec{\tau}}{\partial p}}_{F}+\underbrace{\left(\frac{\partial p}{\partial s}\right)^{-1}\nabla_s\cdot\left(\nu\frac{\partial p}{\partial s}\nabla_s\vec{v}\right)}_{G} \tag{2.2}$$

$$\underbrace{\frac{\partial}{\partial t_s}\left(\frac{\partial p}{\partial s}\theta\right)}_{A}+\underbrace{\nabla_s\cdot\left(\vec{v}\frac{\partial p}{\partial s}\theta\right)}_{B}+\underbrace{\frac{\partial}{\partial s}\left(\dot{s}\frac{\partial p}{\partial s}\theta\right)}_{C}=\underbrace{\nabla_s\cdot\left(\nu\frac{\partial p}{\partial s}\nabla_s\theta\right)}_{D}+\underbrace{H_\theta}_{E} \tag{2.3}$$

Equations 2.1, 2.2, and 2.3 are mass continuity (or layer thickness tendency), momentum, and conservation equations, respectively. Because two thermodynamic variables are conserved and there are two components to the horizontal velocity vector, equations 2.2 and 2.3 are used to write two equations each. In all of the equations above and to follow, $\vec{v}=(u,v)$ is the horizontal velocity vector, $M\equiv gz+p\alpha$ is the Montgomery potential, $\vec{k}$ is a vertical unit vector, ν is a variable eddy viscosity/diffusivity coefficient, and $\vec{\tau}$ is the wind- and/or bottom drag-induced shear stress vector. The variable $\dot{s}$ is an unspecified vertical coordinate, and subscripts indicate the variables that are held constant during partial differentiation. $\xi\equiv\frac{\partial v}{\partial x_s}-\frac{\partial u}{\partial y_s}$ is relative vorticity, α is the potential specific volume, and p is pressure. In addition, $gz\equiv\phi$ is the geopotential and f is the Coriolis parameter. The quantity $\dot{s}\frac{\partial p}{\partial s}$ is the vertical mass flux term, and it is positive in the downward, +p, direction [Bleck, 2002]. θ represents any two of three thermodynamic variables to be chosen from temperature (T), salinity (s), and density (ρ). For all of the work to follow, salinity and density are conserved.

Each of equations 2.1 through 2.3 can be vertically integrated to obtain the governing equations for each layer. Two of the terms in equation 2.2 change after it is multiplied by $\frac{\partial p}{\partial s}$, integrated over (s_{top}, s_{bottom}), and then divided by $\frac{\Delta p}{\Delta s}$. The shear stress term (F) becomes $\frac{g}{\Delta p}\left(\vec{\tau}_{top}-\vec{\tau}_{bottom}\right)$, while the lateral momentum mixing term (G) becomes $(\Delta p)^{-1}\nabla_s\cdot(\nu\Delta p\nabla_s\vec{v})$. The other terms in equation 2.2 remain the same. When equation 2.1 is vertically integrated over a layer bounded

by two s-surfaces, it becomes a prognostic equation for the layer weight per unit area (equation 2.4). Here, the ocean surface, interior layer interfaces, and seafloor can all be s-surfaces. The layer weight per unit area is defined as $\Delta p = p_{bot} - p_{top}$.

$$\underbrace{\frac{\partial}{\partial t_s}\Delta p}_{A} + \underbrace{\nabla_s \cdot (\vec{v}\Delta p)}_{B} + \underbrace{\left(\dot{s}\frac{\partial p}{\partial s}\right)_{bottom} - \left(\dot{s}\frac{\partial p}{\partial s}\right)_{top}}_{C} = 0 \tag{2.4}$$

Equation 2.3 (HYCOM's conservation equation) can be vertically integrated over an s-layer (s_{top}, s_{bot}) to yield:

$$\underbrace{\frac{\partial}{\partial t}\theta\Delta p}_{A} + \underbrace{\nabla_s \cdot (\vec{v}\theta\Delta p)}_{B} + \underbrace{\left(\dot{s}\frac{\partial p}{\partial s}\theta\right)_{bottom} - \left(\dot{s}\frac{\partial p}{\partial s}\theta\right)_{top}}_{C} = \underbrace{\nabla_s \cdot (\nu\Delta p\nabla_s\theta)}_{D} + \underbrace{H_\theta}_{E} \tag{2.5}$$

Here, H_θ is the sum of all diabatic source terms that act on θ. The diabatic source terms involve a transfer of heat and include diapycnal mixing, heat fluxes due to latent and sensible heating, precipitation, and net surface radiative fluxes.

SST changes due to wind stress curl-induced upwelling are parameterized in these core HYCOM equations, while those due to entrainment can be found in the vertical mixing scheme (Section 2.3). Positive surface wind stress curl (equation 2.2, term F) causes surface Ekman divergence in the ocean currents (equations 2.1 and 2.4, term B). This divergence causes vertical motion (equation 2.1 and 2.4, term C), which results in upwelling cooling of the SST (equation 2.5, term A). Horizontal advection, which is also forced by wind stress, is calculated via term D of equations 2.3 and 2.5.

In addition to the above three prognostic equations, diagnostic equations such as the hydrostatic equation (equation 2.6) and an equation of state (with density as a function of salinity, temperature, and pressure) are used to help solve the system of equations. The vertical mass flux term $\dot{s}\frac{\partial p}{\partial s}$ found in equations 2.2 and 2.3 is described by a diagnostic equation, which in turn is used as the basis of the algorithm for the grid generator [Bleck, 2002].

$$\frac{\partial M}{\partial \alpha} = p \tag{2.6}$$

2.3 Vertical Mixing Scheme: KPP in HYCOM

The KPP is an upper ocean vertical mixing parameterization that determines the surface boundary layer depth of a fluid and simulates mixing through the fluid layers. Different physical processes are parameterized depending on the location within the fluid [Large et al., 1994]. Essentially, the KPP parameterizes the fundamental physical processes that govern vertical mixing in the surface boundary layer and in the interior ocean. Because these fundamental processes are not the same in the two fluid regions, calculations of diffusivities and viscosities compose two separate parts of the KPP algorithm, which in HYCOM are divided by the diagnosis of the surface boundary layer depth (h_b). In the surface boundary layer, the KPP parameterizes mixing due to wind, destabilizing convective instabilities, and surface buoyancy fluxes [Halliwell, 2004; Large et al., 1994]. In the stratified ocean interior, it parameterizes mixing due to internal wave breaking, shear instability, and double diffusion. Diffusivities and viscosity in the surface boundary layer are calculated with a shape function, which is chosen so that the layer diffusivity profile smoothly transitions to that in the interior ocean. The shape function is also chosen so that the surface boundary layer satisfies Monin-Obukhov similarity theory, which says that the distance from the boundary and the surface kinematic fluxes are the only important turbulence parameters in the surface layer near the boundary [Large et al., 1994; Large and Gent, 1999]. Today, the KPP is commonly used to simulate vertical mixing in OGCMs.

Initially, HYCOM model variables are stored in momentum (u,v), and vertical (p) grid spaces. The KPP is a one-dimensional vertical mixing scheme, so the first step within the algorithm is to horizontally interpolate model variables from the (u,v) grid points to p grid points [Halliwell, 2004]. Total diffusivities in both regions are determined by the sum of the contributions of potential temperature and salinity diffusivities, and momentum diffusivity (viscosity).

Interior ocean temperature, salinity, and momentum diffusivities are first calculated with

equation 2.7:

$$\nu_\theta(d) = \nu_\theta{}^s(d) + \nu_\theta{}^w(d) + \nu_\theta(d)^d \tag{2.7}$$

Here, s, w, and d represent the contributions of resolved shear instability, unresolved shear instability due to the background internal wave field, and double diffusion, respectively. Each of these diffusivities is parameterized by KPP, as detailed below. Unless otherwise noted, θ can be temperature, salinity, or momentum in this and all equations to follow. Equation 2.7 can also be used to calculate the gradient of interior diffusivity at the boundary layer depth and to force the interior ocean. The interior ocean diffusivities given in equation 2.7 are used to determine the turbulent vertical heat fluxes in the interior via equation 2.8.

$$\overline{w\theta}(d) = -\nu_\theta(d)\frac{\partial\theta}{\partial z} \tag{2.8}$$

Shear instability in the interior ocean (equation 2.7) is characterized by the local gradient Richardson number (Ri_g; equation 2.9), which is calculated at model interfaces [Large et al., 1994].

$$Ri_g = \frac{N^2}{\left(\frac{\partial\overline{u}}{\partial z}\right)^2 + \left(\frac{\partial\overline{v}}{\partial z}\right)^2} \tag{2.9}$$

Here, $\overline{u}$ and $\overline{v}$ are the mean eastward and northward velocities, and N^2 is the local buoyancy frequency, squared. For values of Ri_g less than the critical Richardson number $Ri_o = 0.7$, the vertical velocity shear overcomes the stabilizing buoyancy gradient, and turbulent mixing is triggered [Large et al., 1994].

Interior ocean diffusivities due to shear instability are then calculated using a set of functions (equation 2.10) that depend on the value of Ri_g relative to Ri_o. These functions are the same for temperature, salinity, and momentum diffusion, so that the contribution of resolved shear instabilities (ν_θ^s) is the same for all three interior ocean diffusivities ($\nu_\theta\,(d)$). Here, $p_1 = 3$, and $\nu^0 = 50 \times 10^{-4} m^2 s^{-1}$.

$$\frac{{\nu_\theta}^s}{\nu^0} = \begin{cases} 1, & Ri_g < 0 \\ \left[1 - \left(\frac{Ri_g}{Ri_o}\right)^2\right]^{p_1}, & 0 < Ri_g < Rio \\ 0, & Ri_o < Ri_g \end{cases} \tag{2.10}$$

The contributions of internal wave breaking to the interior diffusivities and viscosity are set as the following experimentally determined constants [Large et al., 1994]: $\nu_m^w = 1.0 \times 10^{-4} m^2 s^{-1}$ and $\nu_{S,T}^w = 0.1 \times 10^{-4} m^2 s^{-1}$.

Double diffusion (ie: salt fingering and diffusive convection) in the interior ocean is parameterized using the double diffusion density ratio (R_ρ) calculated at model interfaces with equation 2.11:

$$R_\rho = \frac{\alpha \frac{\partial \overline{\theta}}{\partial z}}{\beta \frac{\partial \overline{S}}{\partial z}} \tag{2.11}$$

Note that double diffusion only contributes to interior potential temperature and salinity diffusivities, and not to viscosity. The effects of salt fingering and diffusive convection on salinity and temperature diffusivities are calculated differently (equations 2.12 - 2.13 and 2.14 - 2.15, respectively), but they are always functions of R_ρ [Large et al., 1994]. In equation 2.12, $\nu_f = 10 \times 10^{-4} m^2 s^{-1}$, $R_\rho^0 = 1.9$, $p_2 = 3$, and θ and s refer to temperature and salinity, respectively. In equation 2.15, ν is the molecular viscosity for temperature.

$$\frac{\nu_s^d(R_p)}{\nu_f} = \begin{cases} 0, & R_\rho \geq R_\rho^0 \\ \left[1 - \left(\frac{R_\rho - 1}{R_\rho^0 - 1}\right)^2\right]^{p_2}, & 1 < R_\rho < R_\rho^0 \end{cases} \tag{2.12}$$

$${\nu_\theta}^d(R_\rho) = 0.7{\nu_s}^d \tag{2.13}$$

$$\nu_s^d = \begin{cases} {\nu_\theta}^d(1.85 - 0.85{R_\rho}^{-1})R_\rho, & 0.5 \leq R_\rho < 1.0 \\ {\nu_\theta}^d 0.15 R_\rho, & R_\rho < 0.5 \end{cases} \tag{2.14}$$

$$\frac{\nu_\theta^d}{\nu} = 0.909exp\left(4.6exp\left[-0.54\left(R_\rho^{-1}-1\right)\right]\right) \tag{2.15}$$

Once the interior temperature and salinity diffusivities and viscosity are calculated, the bulk Richardson number (Ri_b; equation 2.16) is used to solve for h_b. Surface boundary layer thickness is defined in KPP as the depth range over which turbulent boundary layer eddies can penetrate before they become stable relative to the local buoyancy and velocity [Large and Gent, 1999]. In HYCOM, it is estimated as the minimum depth at which Ri_b exceeds a critical Richardson number $Ri_c = 0.3$. Beginning with the surface and moving down, Ri_b is calculated for each model layer until the KPP reaches the first layer where it is greater than 0.3. Surface boundary layer thickness is then estimated in HYCOM using linear interpolation between the middle of that layer and the one above [Wallcraft et al., 2009].

$$Ri_b = \frac{(B_r - B)\,d}{(\overline{v}_r - \overline{v})^2 + V_t^2} \tag{2.16}$$

$$V_t{}^2(d) = \frac{c_v(-\beta_T)^{\frac{1}{2}}}{Ri_c\kappa^2}(c_s\epsilon)^{-\frac{1}{2}}dNw_s \tag{2.17}$$

In equation 2.16, V_t is the unresolved turbulent velocity shear, β is buoyancy, and r indicates reference values. The turbulent velocity shear (equation 2.17) is typically the most important when there is little or no mean shear, such as in pure convection [Large et al., 1994]. The term β_T is the ratio of entrainment flux to the surface buoyancy flux, and it is constant and negative in the convective limit, but depends on turbulent frictional velocity in forced convection. ϵ is the nondimensional extent of the surface layer and is set as 0.1, while $\kappa = 0.4$ is the Von Karman constant, c_v is the ratio of interior buoyancy to buoyancy at the Ekman depth (h_E; equation 2.18), and c_s is a coefficient of the flux profile for scalars (temperature or salinity) in its 1/3 power law regime. Finally, w_s is the turbulent velocity scale for scalars. Under stable forcing conditions, the boundary layer depth must be smaller than both the Ekman depth (equation 2.18) and the Monin-Obukhov Length (L; equation 2.19) [Large et al., 1994].

$$h_E = \frac{0.7u^*}{f} \tag{2.18}$$

$$L = \frac{u^{*3}}{\kappa B_f} \tag{2.19}$$

After calculating the surface boundary layer depth, surface boundary layer diffusivities are calculated at model interfaces and smoothly matched to the interior diffusivities and viscosity [Halliwell, 2004]. As in the interior ocean, there are three boundary layer diffusivities: T, S, and momentum (viscosity). The three boundary layer diffusivities are parameterized in equation 2.20 as functions of a velocity scale (w_θ), a shape function ($G(\sigma)$), and h_b. The shape function is a third-order polynomial function with four constants that are chosen so that each modeled variable satisfies the Monin-Obukhov similarity theory. Constants are also chosen to be certain that the resulting diffusivity profiles and their first derivatives in the surface boundary layer match those of the interior diffusivity profiles, which helps to maintain a smooth transition between diffusivity and viscosity fields of the interior and boundary layer regions.

$$K_\theta(\sigma) = h_b w_\theta(\sigma) G_\theta(\sigma) \tag{2.20}$$

The vertical turbulent fluxes of the scalars and momentum in the surface layer are calculated using equation 2.21. Salinity and temperature vertical fluxes have nonlocal transport terms (γ) that include the effects of surface fluxes and penetrating shortwave radiation, while the momentum flux does not [Large et al., 1994; Large and Gent, 1999].

$$\overline{w\theta}(d) = -K_\theta(\frac{\partial_z \theta}{\partial z} - \gamma_\theta) \tag{2.21}$$

The velocity scales (w_θ; equation 2.22) are different for T, S, and viscosity, but all depend on the ratio $\sigma = d/h_b$. Again, θ refers either to temperature, salinity, or vector momentum ($\vec{v}$), while a_θ and c_θ are constants that vary for each θ. The variables w^* and u^* represent the convective (equation 2.23) and turbulent friction (equation 2.24) velocity scales, respectively.

$$w_\theta = \begin{cases} \kappa\left(a_\theta u^{*3} + c_\theta \kappa \sigma w^{*3}\right)^{1/3} \rightarrow \kappa(c_\theta \kappa \sigma)^{1/3} w^*, & \sigma < \epsilon \\ \kappa\left(a_\theta u^{*3} + c_\theta \kappa \epsilon w^{*3}\right)^{1/3} \rightarrow \kappa(c_\theta \kappa \epsilon)^{1/3} w^*, & \epsilon \leq \sigma < 1 \end{cases} \tag{2.22}$$

$$w^* = (-B_f h_b)^{1/3} \tag{2.23}$$

$$u^* = ({u^*}_{min}, \sqrt{\alpha_{ref} c_d \rho_a} u) \tag{2.24}$$

In the equations above, B_f is the surface buoyancy flux, h_b is the boundary layer depth, $u^*_{min} = 1.0 \times 10^{-5} ms^{-1}$, $c_d = 0.0013$ for the experiments run in Chapter 3 and 0.0015 in Chapter 4, $\rho_a = 1.2 kgm^{-3}$, $\alpha_{ref} = 1.0 \times 10^{-3} m^3 kg^{-1}$, and u is the wind speed. HYCOM also contains the option to calculate u^* from wind stress data, but for this work, we have chosen to calculate u^* from wind speed.

The effect of increased wind speed on the surface mixed layer can be studied with equations 2.18 - 2.24. Higher wind speed results in an increased turbulent friction velocity scale (u^*; equation 2.24), which in turn leads to a larger velocity scale w_θ (equation 2.22). Then, the surface layer diffusivities (K_θ; equation 2.20) and vertical fluxes (equation 2.21) must amplify as well. The larger values of u^* and u^{*3} also mean that the Monin-Obukhov and Ekman layers (equations 2.18 and 2.19), and thus the surface boundary layer, are all deeper. Increased wind speed-induced entrainment, then, is reflected in the increased surface layer diffusivities and vertical fluxes, and in a thicker surface layer. Wind stress can affect the mixed layer by inducing vertical current shear, which reduces the local gradient and bulk Richardson numbers (equations 2.9 and 2.16), which can in turn trigger mixing and alter the surface boundary layer thickness.

After determining h_b, interior diffusivities and viscosity, and surface boundary layer diffusivities and viscosity for each model layer, a tri-diagonal matrix system is used to solve the vertical diffusion equation given in equation 2.25 [Wallcraft et al., 2009]. The procedure is repeated using the resulting vertically mixed profiles of model variables to get a new vertically mixed profile of

the same variables. This continues until the profiles resulting from two consecutive runs are essentially the same. This final set of viscosity and diffusivity vertical profiles is then used to mix the model scalars stored at p grid points.

$$\frac{\partial \overline{\theta}}{\partial t} = -\frac{\partial}{\partial z}\overline{w'\theta'} \tag{2.25}$$

Once the model scalars are vertically mixed, the KPP determines the mixed layer thickness, which is not necessarily equivalent to the surface boundary layer depth [Large and Gent, 1999]. The model travels down through its vertical layers until the density of a layer exceeds the surface layer density by an amount prescribed by the user (equivalent to 0.5°C for our experiments), at which point vertical interpolation is used to determine the actual depth [Wallcraft et al., 2009]. Finally, the diffusivity and viscosity profiles that were calculated in the final iteration of KPP on the p grid points are used to mix the momentum grid points [Wallcraft et al., 2009]. KPP horizontally interpolates the diffusivity and viscosity vertical profiles from the aforementioned iteration to the momentum grid points (u,v), where the interpolated values are then used to solve the vertical diffusion equation in the new coordinate space.

2.4 Model Grid Generator

Operating in the vertical, HYCOM's model grid generator is the last sequence to run at each time step. It checks each coordinate layer's density, and whenever possible, it restores isopycnic conditions to that layer [Bleck, 2002; Wallcraft et al., 2009]. The grid generator also maintains minimum layer thicknesses in both the upper and lower portions of the water column, each of which is specified by the user [Halliwell, 2004]. Here, 3m is chosen as the minimum layer thickness. First, the algorithm considers the properties of three adjoining model layers in determining if grid points need to be moved to maintain isopycnal and minimum thickness conditions. If the density of a coordinate layer does not equal its target isopycnic reference density, the grid generator moves either its upper or lower interface to exchange mass with an adjacent layer (and thus alter its density)

[Bleck, 2002; Halliwell, 2004].

The grid generator contains two user-specified minimum layer thickness parameters: δ_k and δ_{min}. The former represents the minimum thickness allowed for a layer in the surface boundary region, while the latter replaces it for layers below the boundary region. While attempting to restore isopycnal conditions, the grid generator compares all layer depths to the minimum layer thickness. At the surface layers, if density is larger than the target value, isopycnic conditions cannot be restored because upward movement of the top boundary is blocked by minimum layer thickness enforcement [Bleck, 2002]. Then, the layer transitions to a pressure-coordinate domain, with a cushion function to ensure that the transition is smooth [Halliwell, 2004]. The interior minimum layer thickness δ_{min} allows sharp pycnoclines to form by allowing a smaller layer thickness to be specified in the ocean interior [Halliwell, 2004].

2.5 Surface Fluxes

Air-sea surface flux parameterizations from Kara et al. [2000] are used to obtain sensible and latent heat fluxes (H and $L \times E$; equations 2.26 and 2.27) that include the effects of dynamical stability but are also computationally efficient. Both fluxes contribute to turbulent mixing in the ocean mixed layer and are necessary for accurate modeling of SST [Kara et al., 2000]. These parameterizations all consist of heat flux coefficients ($C_{L,S}$) and are dependent on wind speed and the air-sea temperature difference, and which are then used to calculate the heat fluxes. In equations 2.26 and 2.27, $\vec{V_a} = (u, v)$ is the wind velocity, ρ_a is the density of the air at the air-sea interface, and q_a and q_s are the vapor mixing ratios (specific humidity) for the air and sea. Equations for these variables and the flux coefficients can be found in Kara et al. [2000]. Note that an increase in wind speed ($\vec{V}$) results in increased latent and sensible heat fluxes, when air temperature does not equal SST and the air is not saturated.

$$H = C_S C_p \rho_a \vec{V_a} \left(T_a - T_S\right) \tag{2.26}$$

$$L \times E = C_L L \rho_a \vec{V}_a \left(q_a - q_s\right) \tag{2.27}$$

2.6 Rectification in HYCOM

Based on these core HYCOM model equations, wind can affect the SST though upwelling, horizontal advection, entrainment, and turbulent heat fluxes (THF). It is clear from equations 2.1-2.3 that changes to wind stress can cause upwelling and horizontal advection in the model (see more details in Section 2.2). Wind stress can also cause vertical current shear, which impacts vertical mixing and the surface boundary layer depth through equations 2.9 and 2.16, and thus affects SST. Equations 2.26 and 2.27 show how changes in wind speed can cause changes in sensible and latent heat fluxes. HYCOM output calls these fluxes 'turbulent heat fluxes,' and the same terminology will be used here. As discussed in Section 2.3, because we have chosen to calculate the turbulent frictional velocity (u^*) from wind speed rather than from wind stress, entrainment is forced by changes in wind speed, and it is parameterized in equations 2.18 - 2.24. Entrainment can also be altered by changes in stratification due to THF. That is, in this work, the term 'entrainment' is meant to describe the effects of the turbulent frictional velocity (u^*; calculated from wind speed) and changes in stratification due to THF on the temperature of the mixed layer.

Chapter 4 of this thesis focuses on the impact of atmospheric ISOs on the mean and seasonal-to-interannual variability of SST, mixed layer thickness (hm), and upper ocean heat content. Calculations of hm are completed in the last step of the KPP, and it is dependent on the final mixed profile of temperature. Heat content over a vertical layer is calculated using the standard formula $HC = \rho_z c_p T_z Z$, where ρ_z is the density of sea water in a layer, c_p is the specific heat of sea water ($4.0 \times 10^3 Jkg^{-1}C^{-1}$), T_z is the temperature of the same layer, and Z is the layer thickness. For upper ocean heat content, Z is 200m, and T_z and ρ_z are weighted averages over the layer. As with hm, upper ocean heat content depends on the mixed temperature and density profiles. Because hm and upper ocean heat calculations are determined from the final temperature profiles, we will focus only on isolating the wind-induced rectification onto low frequency SST.

The first step in determining how wind speed and stress can rectify onto the mean and seasonal-to-interannual SST is to decompose the model equations that encompass the wind processes into mean ($\bar{\cdot}$), intraseasonal (*), and low-frequency ($'$) components. However, the complexity of HYCOM's equations makes it difficult to exactly isolate the impacts of intraseasonally-forced wind on low frequency SST. For example, in evaluating the rectification due to entrainment, one can decompose equation 2.24 to yield the turbulent velocity due to intraseasonal wind speed only. However, the decomposed turbulent velocity then combines with a convective velocity scale (w^*), a series of constants, and a depth ratio to determine the velocity scale for temperature (equations 2.22 and 2.23). The velocity scale, in turn, is used to determine the vertical turbulent fluxes for temperature (equations 2.20 and 2.21), which are used to determine the mixed temperature profile. It is impossible to know the value of many of the constants and ratios used in the intermediate steps of KPP, and thus it would be exceedingly difficult, if not impossible, to exactly calculate the rectified impacts of intraseasonal wind speed-forced entrainment on seasonal-to-interannual SSTs. Similarly, it is very difficult to determine the impacts of wind stress-induced vertical current shear on SST.

Due to these complexities, it is difficult to use specific terms of the HYCOM equations to understand the rectification processes. Instead, the rectified effects of entrainment and THF due to wind speed, and of upwelling and horizontal advection due to wind stress, are diagnosed with the series of equations discussed below. Each equation is used to determine the full impacts (i.e. the ocean response across all timescales) of upwelling, horizontal advection, entrainment, and THF due to ISOs. Then, the seasonal and interannual rectification is isolated from the full impacts . The total rectification of ISOs onto low-frequency (seasonal + interannual) variability is estimated with monthly averages of the ISO-forced ocean response (i.e. average January 2002, February 2002, . . ., December 2008 from difference solution MR-EXP1). The rectification of ISOs onto the seasonal cycle is isolated by calculating the monthly climatology of the ISO-forced ocean response (i.e. average January 2002-2008; February 2002-2008, . . ., December 2002-2008). Then, the rectification of ISOs onto interannual variability is the difference between the total low-frequency response

(monthly average) and the seasonal response (monthly climatology), as given in equation 2.28.

$$T_{iann} = T_{monavg} - T_{monclim} \tag{2.28}$$

2.6.1 Estimating the Rectification due to Upwelling

Upwelling due to intraseasonal wind stress is estimated using the standard formulas:

$$dTup = w_E \left(\frac{dT}{dz}\right) dt \tag{2.29}$$

$$w_E = \frac{\partial}{\partial x}\left(\frac{\tau_y}{f}\right) - \frac{\partial}{\partial y}\left(\frac{\tau_x}{f}\right) \tag{2.30}$$

Tup is the change in temperature due to upwelling over a given time interval (3 days for our purposes), dz is the thickness of the surface layer, ∂x and ∂y are the zonal and meridional grid spacing in m; τ_x and τ_y are the zonal and meridional wind stress, f is the Coriolis parameter calculated at a given latitude, and dt is the time interval. Decomposing equation 2.29 into mean (-), intraseasonal (*), and seasonal-to-interannual components ($'$) yields $Tup_{mean+var} = (w_E^* + w_E') \times \frac{d}{dz}\left(\overline{T} + T^* + T'\right) dt$. Because only the Tup due to intraseasonal wind stress is desired, w_E^* is isolated by calculating w_E due only to intraseasonal wind stress. At the same time, we are only interested in the impact of intraseasonal wind stress on the seasonal-to-interannual variability of Tup. Because $T = \overline{T} + T^* + T'$, we can isolate T^* and T' with $T - \overline{T}$. Applying these changes yields the following equation for the impact of intraseasonal wind stress-forced upwelling on SST:

$$dTup_{ISO} = w_E^* \frac{d}{dz}\left(T - \overline{T}\right) dt \tag{2.31}$$

Put together, the 3-day change in SST due to ISO-forced upwelling depends on the intraseasonal Ekman pumping velocity (w_E), the thickness of the surface layer, and the model output temperature over the same layer. The intraseasonal wind stresses needed to calculate the intraseasonal Ekman pumping velocity (equation 2.30) are obtained by low-pass filtering the wind stress forcing

fields to 105 days. Then, the difference between the filtered and unfiltered wind stresses isolates only those wind stresses with periods from 10-105 days.

2.6.2 Estimating the Rectification due to Horizontal Advection

The temperature change due to horizontal advection is generally defined as $dT = -\vec{V} \cdot \nabla T dt = -\left[u\left(\frac{d}{dx}T\right) + v\left(\frac{d}{dy}T\right)\right] dt$, where $\vec{V} = (u, v)$ is the velocity of the current in the surface layer, T is the temperature of the surface layer, and dt is the time interval (3 days for all work in this dissertation). To isolate the full dT forced only by intraseasonal wind stress, we must calculate the surface current velocity due to wind stress, u^* and v^*. This is simply the difference between the model output current from MR and from EXP3 (Tables 2.1 and 2.2). In an equation, $\vec{V}_{stressonly} = \vec{V}_{MR} - \vec{V}_{EXP3}$. Put together, the 3-day temperature change due to intraseasonal wind stress-forced horizontal advection is:

$$dT_{advISO} = -\left[u^*\left(\frac{d}{dx}\left(T - \overline{T}\right)\right) + v^*\left(\frac{d}{dy}\left(T - \overline{T}\right)\right)\right] dt \tag{2.32}$$

2.6.3 Estimating the Rectified Impacts of Entrainment

As discussed above, the complexity of HYCOM's model equations makes it very difficult to exactly determine the change in SST due to entrainment forced by intraseasonal wind speed. Entrainment is generally calculated from the vertical temperature gradient over a layer and from an entrainment velocity (w_{Ent}), which is in turn dependent on the vertical velocity at a depth h (w_h) and on the total time derivative of h ($\frac{Dh}{Dt}$), which includes the effects of horizontal advection on h [Equation 2.33; see also Stevenson and Niiler, 1983].

$$dT_{Ent} = w_{Ent}\frac{dT}{dz} = w_h + \frac{Dh}{Dt} \tag{2.33}$$

In difference solution EXP3-EXP4, the model response to any forcing fields except for wind speed are removed. Because w_h is a function of wind stress, it is the same in both EXP3 and EXP4,

and the difference solution removes it from the entrainment equation. Then, entrainment is solely determined by $\frac{Dh}{Dt}$. Because of this, mixed layer thickness (hm) due only to wind speed is used to diagnose the presence of entrainment in the model output. During times of increased entrainment, cool subsurface water is mixed into the ocean's mixed layer, causing a thicker hm and reducing SST. Any changes to hm due to intraseasonal wind speed are indicative of changes in the entrainment rate. A thicker (thinner) hm due only to intraseasonal wind speed indicates that increased (decreased) ISO-forced wind speed is causing enhanced (reduced) entrainment and SST cooling (warming). Changes in hm due to intraseasonal wind speed are calculated using the model difference solution EXP3-EXP4 (Section 2.1). That is,

$$hm_{ISOwspeed} = hm_{EXP3} - hm_{EXP4} \tag{2.34}$$

2.6.4 Estimating the Rectified Impacts of Turbulent Heat Flux

It is also very difficult to determine the exact change in SST due to THF forced by intraseasonal wind speed. However, it is possible to determine the change in THF due to intraseasonal wind speed. HYCOM model output net heat flux (HF_{Net}) is actually the sum of net radiative heat flux (model forcing fields) and THF. Model experiments EXP3 and EXP4 have identical radiative heat fluxes. Because EXP3 is forced only by low-pass 105 day wind stress, while EXP4 is forced by low-pass 105 day wind speed and stress, any difference in model output net heat flux is due only to changes in THF forced by intraseasonal wind speed (equation 2.35)

$$THF_{ISOwspeed} = HF_{NetEXP3} - HF_{NetEXP4} \tag{2.35}$$

2.7 Summary

HYCOM's wide-ranging usage in the ocean modeling community makes it a reasonable choice for evaluating the impact of atmospheric ISOs on intraseasonal, seasonal, and interannual variability in the upper IO. Model output data from the experiments listed in Table 2.1 is used alone

and in the difference solutions detailed in Table 2.2 to estimate the impacts of wind speed (via entrainment and THF) and stress (via upwelling and horizontal advection) on the upper layers of the IO in Chapters 3 and 4. Rectified impacts of wind processes on SST are calculated in Chapter 4 using equations 2.28 and 2.31-2.35.

Chapter 3

Indian Ocean Intraseasonal Sea Surface Temperature Variability During Boreal Summer: Madden-Julian Oscillation Versus Submonthly Forcing and Processes

3.1 Abstract

Intraseasonal sea-surface temperature (SST) variability in the Indian Ocean during boreal summer is investigated with a series of experiments using the Hybrid Coordinate Ocean Model (HYCOM). QuickSCAT winds and satellite observed outgoing longwave radiation (OLR) are used to identify the wind and convection patterns associated with atmospheric intraseasonal oscillations (ISOs). Effects of the Madden-Julian Oscillation (MJO; 30-90 days) and submonthly ISOs are separately examined. Similar to winter, MJO forcing dominates summertime SST variability, even though submonthly forcing is stronger. Wind plays a much larger role in altering SSTs than either shortwave fluxes or precipitation. Different from winter cases, the maximum summertime SST variability shifts to the Arabian Sea (AS) and the Bay of Bengal (BOB), when ISOs also shift to the northern hemisphere. In the BOB, surface heat fluxes due to changes in wind speed have a stronger influence on SST than upwelling and advection induced by wind stress, whereas in winter the effects of surface heat fluxes and oceanic upwelling and advection are comparable. This difference arises from the barrier layer and thin surface mixed layer in the BOB, which reduce the effects of upwelling and amplify the effects of surface heat fluxes. In the AS, surface heat fluxes and entrainment cooling due to changes in wind speed have a larger effect on MJO-scale SST than upwelling induced by wind stress, while the two have comparable effects on submonthly SST. In the equatorial region wind speed and stress are equally important.

3.2 Introduction

3.2.1 Atmospheric Intraseasonal Oscillations

Indian Ocean (IO) intraseasonal oscillations (ISOs) range in scale from 10 to 90 days. On 30-90 day timescales, the Madden-Julian Oscillation (MJO) [Madden and Julian, 1971, 1972] dominates ISOs. On 10-30 day submonthly timescales, convectively coupled Kelvin and Rossby waves dominate the ISOs [Kiladis and Weickmann, 1997; Wheeler and Kiladis, 1999; Chatterjee and Goswami, 2004]. Their important component, the Quasi-Biweekly Mode (QBM), is thought to be a Rossby wave that is shifted northward (southward) by the mean flow during summer (winter) [Murakami and Frydrych, 1974; Chen and Chen, 1993; Numaguti, 1995; Chatterjee and Goswami, 2004]. Observations from the Bay of Bengal Monsoon Experiment (BOBMEX) show that submonthly convection and winds are much stronger than those of the MJO [Bhat et al., 2001; Vincent et al., 1998]. MJOs travel both eastward and northward during boreal summer with global zonal wave numbers 1-3 [Li and Wang, 1994; Hendon and Salby, 1996; Kiladis and Weickmann, 1997; Wang and Xie, 1997; Webster et al., 2002], whereas the QBM propagates westward with zonal wave numbers 5-6 [Kiladis and Weickmann, 1997].

It is suggested that submonthly ISOs together with the MJO can determine the amplitude and phase of the wet and dry spells of the Asian summer monsoon and the Australian monsoon [Sikka and Gadgil, 1980; Yasunari, 1981; Krishnamurti and Subrahmanyam, 1982; Webster, 1983; Lau and Chan, 1985; McBride, 1987; Krishnamurti et al., 1988; Wang and Xie, 1997; Webster and Hoyos, 2004; Lau and Waliser, 2005]. Recent studies have also shown that many ISOs generated in the IO can propagate to the Pacific and impact the El Nino Southern Oscillation (ENSO) [McPhaden, 1999; Moore and Kleeman, 1999; Takayabu et al., 1999; Kessler and Kleeman, 2000], and can affect the onset and termination of the IO dipole (IOD) [Saji et al., 1999; Webster et al., 1999; Murtugudde et al., 2000; Yu and Rienecker, 2000; Rao and Yamagata, 2004; Han et al., 2006b]. Importantly, air-sea interactions over the IO can have a significant influence on ISO propagation [Flatau et al., 1997; Wang and Xie, 1998; Waliser et al., 1999; Kemball-Cook and Wang, 2001;

Woolnough et al., 2001; Fu et al., 2003; Inness and Slingo, 2003; Sperber et al., 2005]. Realistic simulation of ISOs in climate models, however, is still a challenge [Slingo et al., 1996; Sperber et al., 2005; Lin et al., 2006], which underlines the need for further knowledge about coupled processes. To this end, investigating intraseasonal sea surface temperature (SST) variability is key to an increased understanding of coupled processes on intraseasonal timescales.

A large number of studies on IO intraseasonal SST variability exist [McPhaden, 1982; Krishnamurti et al., 1988; Hendon and Glick, 1997; Jones et al., 1998; Shinoda and Hendon, 1998; Shinoda et al., 1998; Woolnough et al., 2000; Harrison and Vecchi, 2001; Sengupta et al., 2001; Schiller and Godfrey, 2003; Waliser et al., 2003, 2004; Duvel et al., 2004; Kessler, 2005; Han et al., 2006a; Saji et al., 2006; Han et al., 2007]. These studies show divergent views of the processes that determine intraseasonal SST variability, and the relative importance of MJO and submonthly ISOs is not addressed for boreal summer. Han et al. [2007] summarized detailed aspects of the studies, and first investigated IO SST variability on both MJO and submonthly timescales for the winter monsoon. For comparison, here we provide a comprehensive study of SST variability during the summer monsoon.

3.2.2 Present Research

This paper will provide a detailed investigation of the impacts of the MJO and submonthly ISOs on SST during boreal summer. To ensure consistency for comparison with Han et al. [2007], we analyze the same set of experiments using the Hybrid Coordinate Ocean Model (HYCOM) to evaluate the importance of oceanic dynamical processes, mixed layer physics, and surface heat fluxes. Section 3.3 details our data, model, and experiment design. In Section 3.4, we discuss our results, while Section 3.5 provides a summary and discussion.

3.3 Data and Model

3.3.1 Data

Observed SST, outgoing longwave radiation (OLR), and winds are used to validate HYCOM solutions and to identify ISOs. Our period of interest is 1998-2004, when all the following datasets are available. Satellite observed daily OLR from the National Oceanic and Atmospheric Administration (NOAA) [Liebmann and Smith, 1996] and 3-day mean winds from QuickSCAT [Tang and Liu, 1996] are used to document ISOs. Prior to July 1999, when QuickSCAT winds do not exist, 3-day ECMWF reanalysis (ERA-40) winds are used. The 3-day mean Tropical Rainfall Measuring Mission (TRMM) SST with $0.25^\circ \times 0.25^\circ$ resolution is analyzed and compared with the model solution. To remove missing values, the TRMM SST is first averaged onto $2.5^\circ \times 2.5^\circ$ grids, and the few missing values left are then filled by linear spatial and temporal interpolation [Han et al., 2007].

Additionally, shortwave (SW) radiation and wind data during 21 October 2001 - 4 June 2004 from Triangle Trans-Ocean Buoy Network (TRITON) floats at 90°E, 1.5°S is analyzed. Two periods of continuous TRITON wind data are available for our range of years, from 23 October 2001 - 27 August 2002, and from 12 July 2003 - 8 June 2004. Vertical temperature and salinity profiles from Argo floats in the Bay of Bengal (BOB) are also studied. Monthly climatologies of temperature and salinity from the World Ocean Atlas 2005 (WOA05) are used to derive mixed layer thickness. Note that near Sumatra and the BOB coasts, WOA05 has very few data points and thus the estimated mixed layer depths may not be reliable in these regions.

3.3.2 Hybrid Coordinate Ocean Model Configuration and Validation of Forcing Fields

HYCOM utilizes terrain-following coordinates in coastal regions, isopycnal coordinates in the interior open ocean, and z coordinates in weakly stratified and surface layers, and in very shallow waters [Bleck, 2002; Halliwell, 2004]. In the present experiments, the K-Profile Parameterization [Large et al., 1994, 1997; Large and Gent, 1999] is chosen as the vertical mixing scheme.

HYCOM has been applied in studies of interannual and intraseasonal variability and the seasonal cycle in the Indian and Atlantic Oceans [Han et al., 2004; Han, 2005; Han et al., 2006a,b; Yuan and Han, 2006; Han et al., 2007]. Since the HYCOM configuration and experiment design are explained in detail in Han et al. [2007], we only provide a brief discussion here.

HYCOM is configured to the IO basin north of 30°S with 18 vertical layers and a horizontal resolution of 0.5°×0.5°. To better resolve the mixed layer, thermocline, and barrier layer, the vertical layers have a fine resolution in the upper ocean. For example, the mean interface depths of the upper 10 layers, averaged over the BOB from 1999-2003, are approximately 3, 48, 138, 151, 161, 169, 178, 191, 208, and 234m. SW radiation penetration is parameterized with Jerlov water type IA [Jerlov, 1976]. No-slip conditions are applied along continental boundaries. Near the southern boundary (25°S-30°S), a 5°-wide sponge layer is applied to relax model temperature and salinity fields to Levitus and Boyer [1994] and to Levitus et al. [1994] climatology. Lateral boundary forcing due to the Indonesian Throughflow and BOB rivers is included by relaxing model temperature and salinity to Levitus data in the corresponding regions.

Primary forcings used are 3-day QuickSCAT winds, International Satellite Cloud Climatology Project Flux Data (ISCCP-FD) SW and longwave radiative fluxes [Zhang et al., 2004], Climate Prediction Center Merged Analysis of Precipitation (CMAP) pentad data [Xie and Arkin, 1996], and ERA-40 and National Centers for Environmental Prediction (NCEP) air temperature and specific humidity for 1998-2004 (see Han et al. [2007] for details). Wind stress (τ) is calculated using QuickSCAT wind speed $\left(\left|\vec{V}\right|\right)$ in a standard bulk formula $\tau = \rho_a C_D \left|\vec{V}\right| \vec{V}$. Here, ρ_a is the density of air ($1.175 kg/m^3$), C_D is a drag coefficient (0.0015), and $\vec{V}$ is the QuickSCAT wind vector. Surface latent and sensible heat fluxes are then calculated using winds, air temperature, specific humidity, and HYCOM SST in the flux parameterizations of Kara et al. [2000].

Validity of these forcing fields was discussed by Han et al. [2007]. Here, we provide further validation. Figure 3.1 shows the variance spectra of zonal and meridional wind stresses from QuickSCAT and TRITON data at 90°E, 1.5°S. Both the TRITON and QuickSCAT wind stresses contain essentially the same spectral peaks at 10-30 day and 30-90 day periods, albeit with some

quantitative differences. Due to the short duration of the TRITON data records, some spectral peaks do not exceed the 90% confidence level. Quantitative comparison between ERA-40 and QuikSCAT wind stress demonstrates that ERA-40 winds are able to capture the observed intraseasonal variabilities rather well, but their amplitudes tend to be stronger than the QuikSCAT winds. After the ERA-40 wind speed is scaled down to 90%, the amplitudes of the ERA-40 winds agree very well with the QuikSCAT winds. Variance spectra of the scaled ERA-40 and QuickSCAT wind stress are shown in Figure 3.2 for a period of overlap (1 August 1999 - 31 December 2001) in the BOB (80-90°E, 4-15°N). Note that the wind stress data is averaged over the BOB before performing the spectral analysis. Both the zonal and meridional wind stresses contain similar peaks over the intraseasonal periods, but the magnitudes of the ERA-40 peaks are greater than those from QuickSCAT at 40-60 days (Figure 3.2a). The shape of the ERA-40 and QuickSCAT spectra are also very similar over the eastern equatorial IO for the same time period (not shown). Based on these comparisons, the scaled ERA-40 winds are used to force HYCOM before July 1999. This specific detail is also true in Han et al. [2006b, 2007], although it is not explicitly stated there.

Similarly, intraseasonal variability of net SW radiation from the TRITON observations is reasonably reproduced by the ISCCP data from 21 October 2001 - 4 June 2004 (Figure 3.3). Note that an albedo of 3% is applied to the TRITON data because it measures the total downward, rather than the net, SW radiation. The correlation coefficient between the two curves is 0.75. The standard deviations (STDs) for ISCCP and TRITON SW radiation are 41.7 Wm^{-2} and 48.6 Wm^{-2}, respectively, indicating that ISCCP may underestimate the SW flux variability by approximately 14%.

3.3.3 Experiments

Seven model experiments are performed for the period of 1998-2004. They are listed in Table 3.1 and summarized below. See Han et al. [2007] for details regarding the model spin-up and other aspects of the experiments.

The main run (MR) is forced by the complete 3-day mean fields discussed in Section 3.3.

Figure 3.1: (a) Variance spectra of zonal wind stress τ_x, from QuickSCAT (thick solid line) and TRITON (thick dashed line) observations for 24 October 2001 - 25 August 2002 at 90°E, 1.5°S. The thin solid/dashed lines show the 90% significance level for each. (b) Same as *a*, but for meridional wind stress τ_y. (c) Same as *a*, but for 11 July 2003 - 10 June 2004. (d) Same as *c*, but for meridional wind stress. The wind stress for TRITON is calculated using the same formula as that for QuickSCAT. Units are dyn^2cm^{-4}.

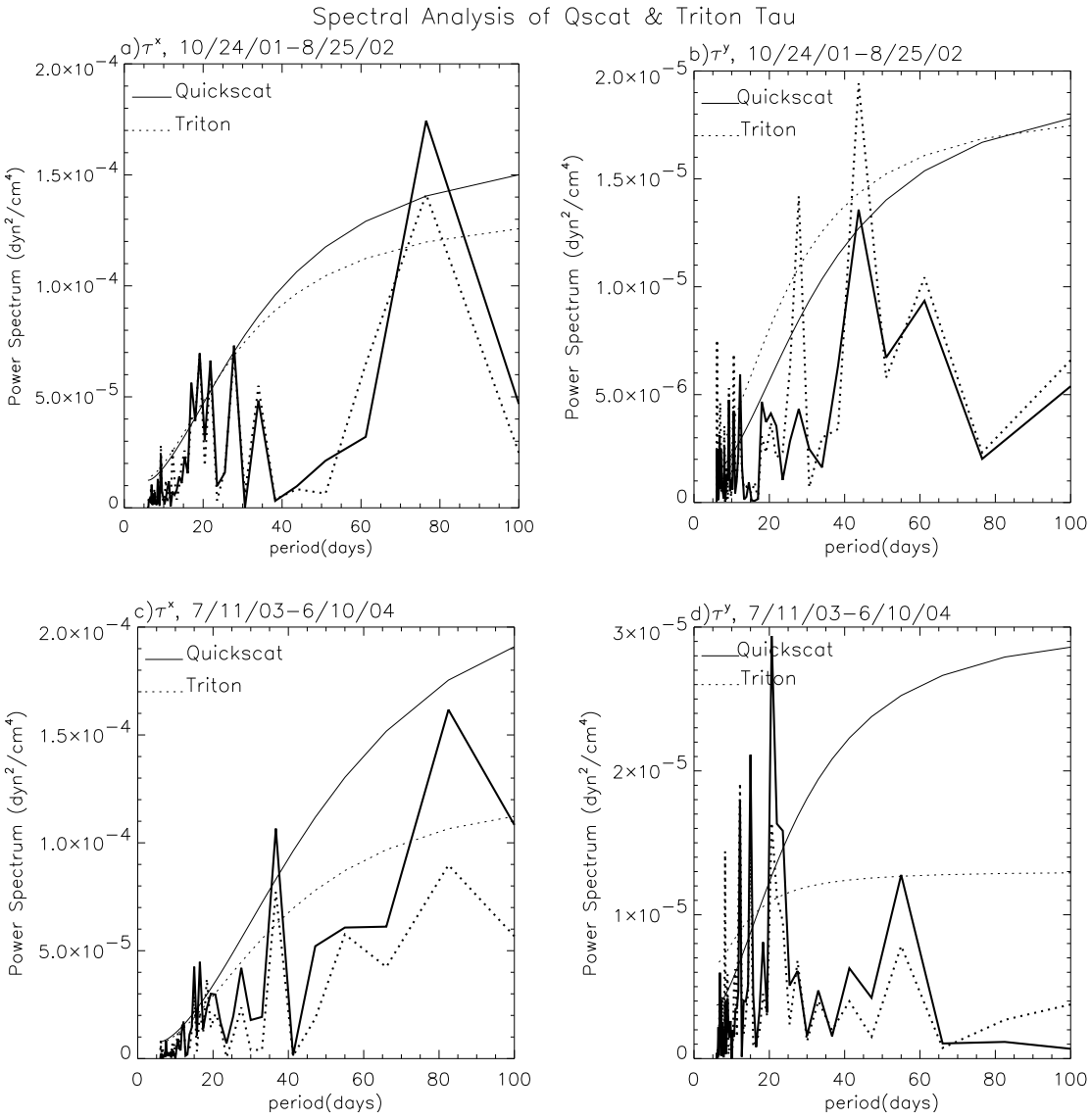

Figure 3.2: (a) Variance spectra of zonal wind stress τ_x, for QuickSCAT observations (thick solid line) and scaled ERA-40 reanalysis (thick dashed line) from 1 August 1999 - 31 December 2001, averaged over the western BOB (80-90°E, 4-15°N). The thin solid/dashed lines show the 90% significance level for each. (b) Same as *a*, but for meridional wind stress τ_y. Units are N m^{-2}.

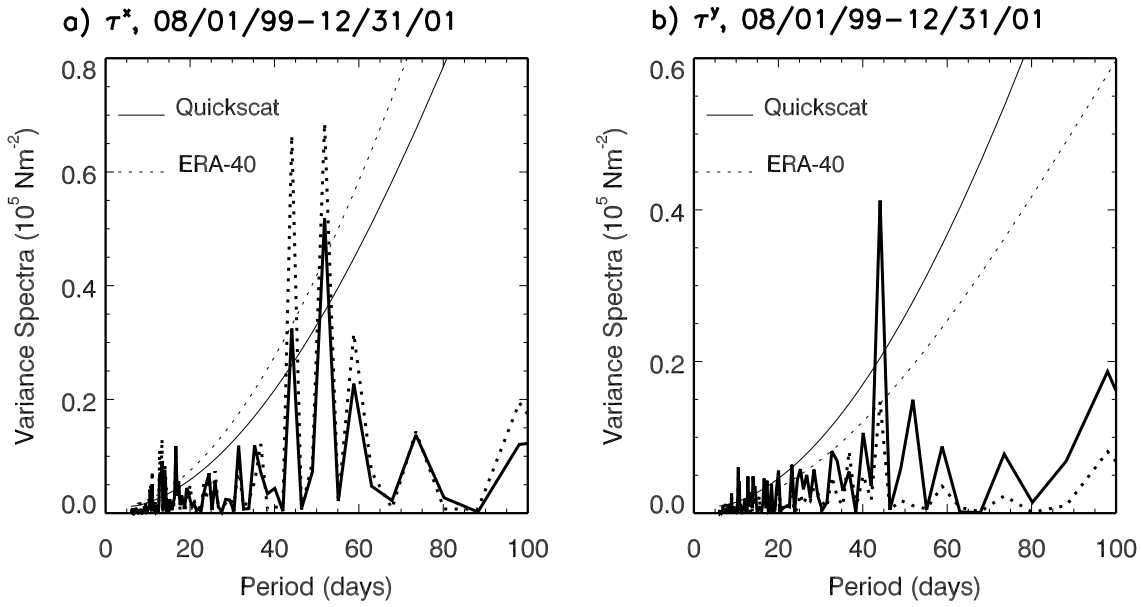

Table 3.1: Hybrid Coordinate Ocean Model experiments and forcings used[a]

Experiment Number	Forcings Used
MR	All 3-day mean forcing fields: winds, fluxes, precipitation
EXP1	Low-passed (removed less than) 105 days
EXP2	Low-passed (removed less than) 30 days
EXP3	Low-passed wind stress
EXP4	Low-passed wind stress and speed
EXP5	Low-passed shortwave flux
EXP6	Low-passed precipitation

[a]Low-pass frequency is 105 days, unless otherwise noted.

Figure 3.3: Time series of TRITON (dashed line) and ISCCP (solid line) net SW radiation from 21 October 2001 - 4 June 2004 at 90°E, 1.5°S. Earth's surface albedo of 3% is applied to the TRITON data. Standard deviations (STD) of both ISCCP and TRITON SW radiation are displayed, along with the correlation coefficient (r) between the two. Units are Wm^{-2}.

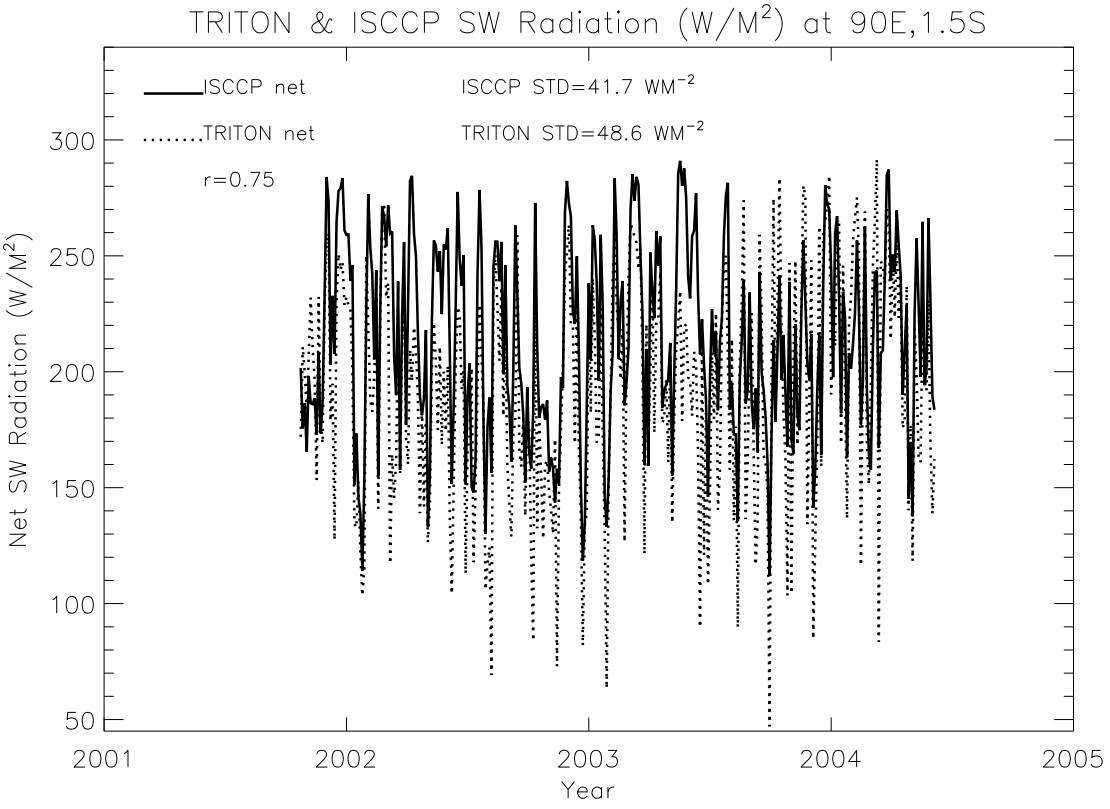

As such, it is the most complete solution, and it is used to evaluate the ocean response due to all forcings. Experiment 1 (EXP1) is forced by low-passed 105-day fields using a Lanczos filter [Duchon, 1979]. The low-passed fields remove any signals with periods shorter than 105 days. The difference solution MR - EXP1, then, isolates the ocean response to ISOs. Similarly, EXP2 employs a low-pass 30-day filter to remove any variability shorter than 30 days from the forcing fields. It follows that MR - EXP2 isolates the effects of submonthly variability, while EXP2 - EXP1 estimates the ocean response to 30-90 day ISOs, which are dominated by MJO events. EXP3 is forced by low-passed 105 day wind stress, so it excludes the effects of intraseasonal Ekman convergence and divergence (which can affect upwelling) as well as anomalous advection. EXP4 is forced by low-passed 105 day wind stress and wind speed. It excludes the same effects as EXP3, with the additional exclusion of intraseasonal wind speed, which can affect the SST via latent and sensible heat fluxes and entrainment cooling. This is because the entrainment rate depends on the frictional velocity u^*, which is directly associated with the wind speed $\left|\vec{V}\right|$ in our experiments because $u^* = \sqrt{(|\tau|\,\rho_a)} = \sqrt{\left(c_D \left|\vec{V}\right|\right)}$. Therefore, when $\left|\vec{V}\right|$ is filtered, the entrainment rate is affected. EXP5 is forced by low-passed 105 day SW flux, and EXP6 by low-passed 105 day precipitation, which can impact the SST by changing stratification and the mixed layer thickness (hm). Then, the difference solutions MR - EXP3, MR - EXP4, EXP3 - EXP4, MR - EXP5, and MR - EXP6 isolate the ocean response to intraseasonal wind stress, total winds, wind speed, SW radiation, and precipitation, respectively.

3.4 Results

3.4.1 Madden-Julian Oscillation (MJO) and Submonthly Intraseasonal Oscillations (ISOs)

Large values of STD in the OLR fields of Figures 3.4a-c indicate where strong variations in convection are located on each timescale. On 10-90 day timescales (Figure 3.4a), strong changes in convection ($\geq$28Wm^{-2}) occur in the central-eastern equatorial ocean, the BOB, and the eastern Arabian Sea (AS), where the mean SST exceeds 28°C (Figure 3.5). While the convective variability

associated with both submonthly ISOs and MJO events has similar spatial patterns, it appears that the former has a larger amplitude than the latter. Averaged over the whole IO, the STDs of 30-90 day and 10-30 day convection are 6.7 Wm^{-2} and 9.6 Wm^{-2}, respectively. Associated with the strong changes in convection, QuickSCAT wind speed (Figures 3.4d-f) and stress curl (Figures 3.4g-i) also show large-amplitude variations in the central-eastern equatorial basin, the BOB, the AS, and the southeast tropical IO. Again, submonthly events show larger amplitude variation than MJO events in most regions except the AS. The whole-IO averaged STDs of 30-90 day and 10-30 day wind speed are 0.69 ms^{-1} and 0.8 ms^{-1}, respectively. The increased strength of submonthly ISO forcings over MJO ISO forcings is consistent with Bhat et al. [2001].

3.4.2 Validation of the Simulated Intraseasonal SST

Over all seasons, the largest intraseasonal SST variability occurs in a region that stretches across the southern tropical IO, western AS, the BOB, and the eastern equatorial ocean (Figures 3.6a,b). The variability south of the equator is a major feature of the winter months that coincides with the location of the winter intertropical convergence zone (ITCZ), which has been investigated in several existing studies [Harrison and Vecchi, 2001; Duvel et al., 2004; Saji et al., 2006; Han et al., 2007].

During summer, the region of large amplitude SST change shifts to the northern IO (Figure 3.6), where maxima in convection and winds are located (Figures 3.4a,d,g). Averaged over summer months from 1999-2003, HYCOM simulates many of the major SST features at all timescales (Figures 3.6c-h), albeit with some quantitative differences. For example, strong SST variations in the AS, the BOB, and the eastern equatorial ocean are all reasonably simulated. An evident exception is the strong variability south of the equator in HYCOM, which does not occur in TRMM data during the summer season (Figures 3.6c-h). As shown by Han et al. [2007], this model/data discrepancy is likely because HYCOM has a much thinner mixed layer than is observed in the region, which makes it more sensitive to surface forcing.

To further quantify model/data comparisons, we choose three regions (labeled in Figure 3.6c)

Figure 3.4: (a) Standard deviation (STD) of 10-90 day band-pass filtered OLR over the tropical IO during boreal summer (May-October) from 1999-2003. (b) Same as *a* except filtered to 30-90 days. (c) Same as *a* except filtered to 10-30 days. (d) STD of 10-90 day band-pass filtered QuickSCAT wind speed during boreal summer from 1999-2003. ERA40 winds are used before July 1999. (e) Same as *d* but filtered to 30-90 days. (f) Same as *d* but filtered to 10-30 days. (g) STD of 10-90 day band-passed QuickSCAT wind stress curl during boreal summer from 1999-2003. (h) Same as *g* but filtered to 30-90 days. (i) Same as *g* but filtered to 10-30 days. Units are Wm^{-2} for OLR, ms^{-1} for wind speed, and $1\times10^{-7}Nm^{-3}$ for wind stress curl.

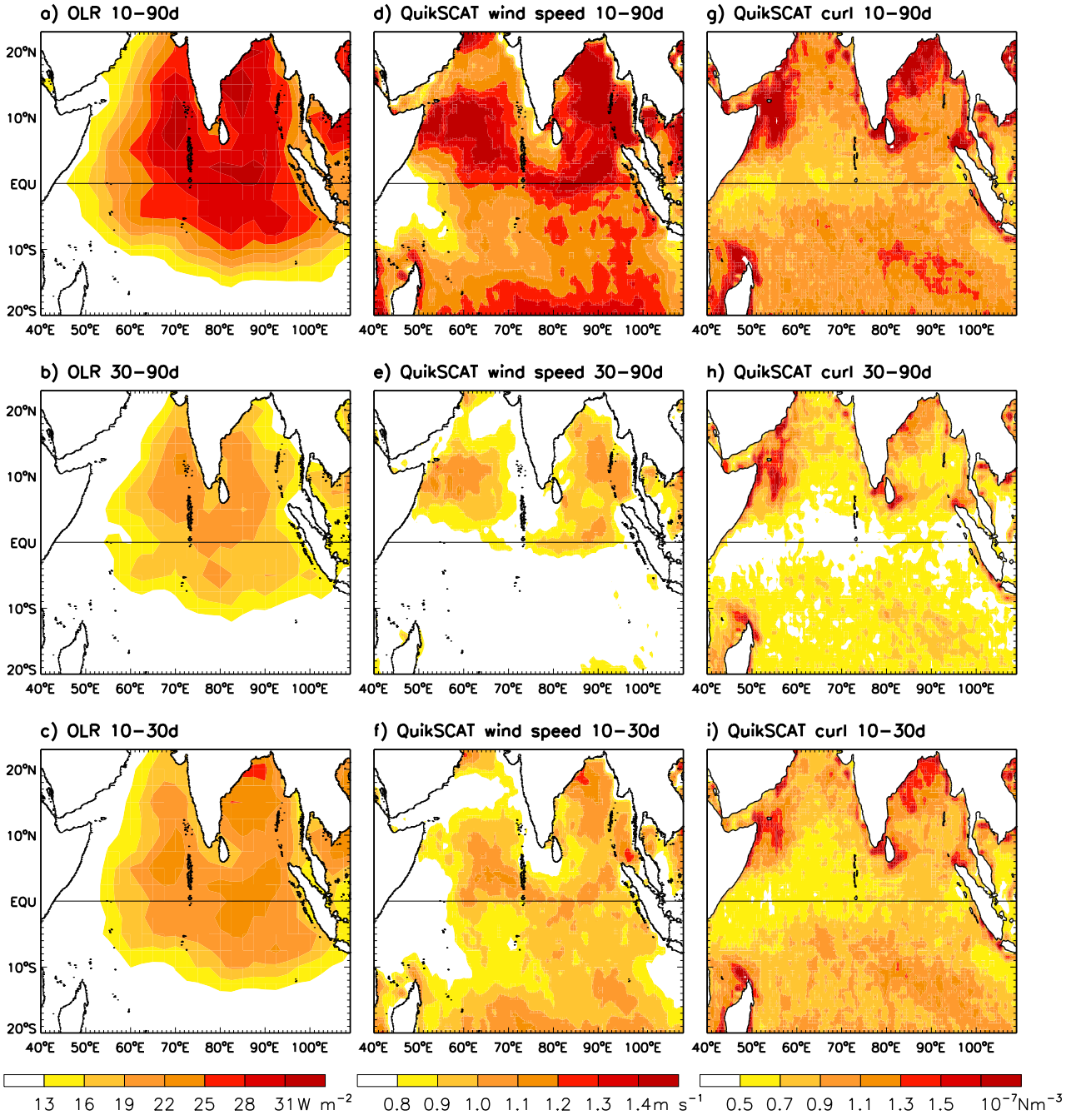

Figure 3.5: Summertime (May-October) mean SST from TRMM (shaded contours) for the period 1998-2004 and wind stress from QuickSCAT (arrows) for the period 1998-2003. ERA-40 wind stress was used before July 1999. Units are °C for SST and dyn cm^{-2} for wind stress.

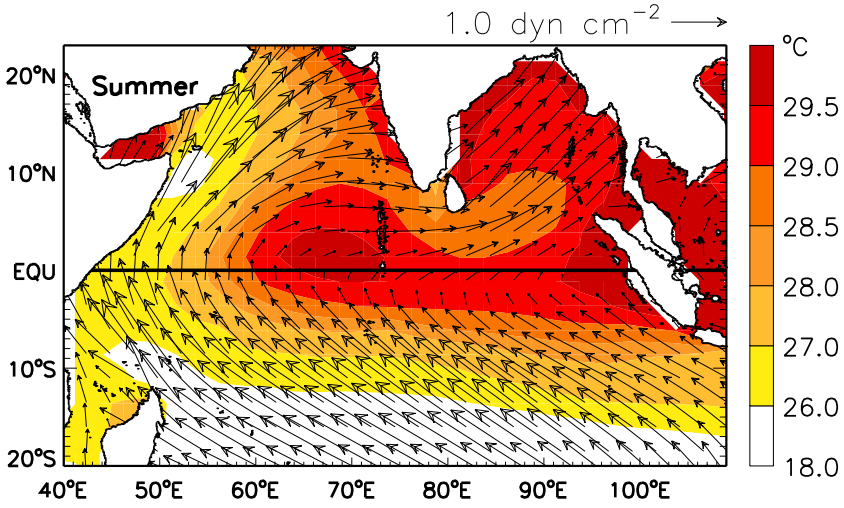

Figure 3.6: Observed (left) and modeled (right) SST standard deviation (STD), 1999-2003. (a) STDs of 10-90 day filtered TRMM SST based on all months from 1999-2003. (b) Same as *a* but for HYCOM MR. (c) Same as *a* but for boreal summer months (May-October) only. Boxed regions represent the AS (Region 1), the BOB (Region 2), and the eastern equatorial warm pool (Region 3), and are discussed in Section 3.4.2. (d) Same as *c* but for HYCOM MR. (e) Same as *c* but for 30-90 day filtered TRMM SST. (f) Same as *e* but for HYCOM MR. (g) Same as *c* but for 10-30 day filtered TRMM SST. (h) Same as *g* but for HYCOM MR. Units are °C.

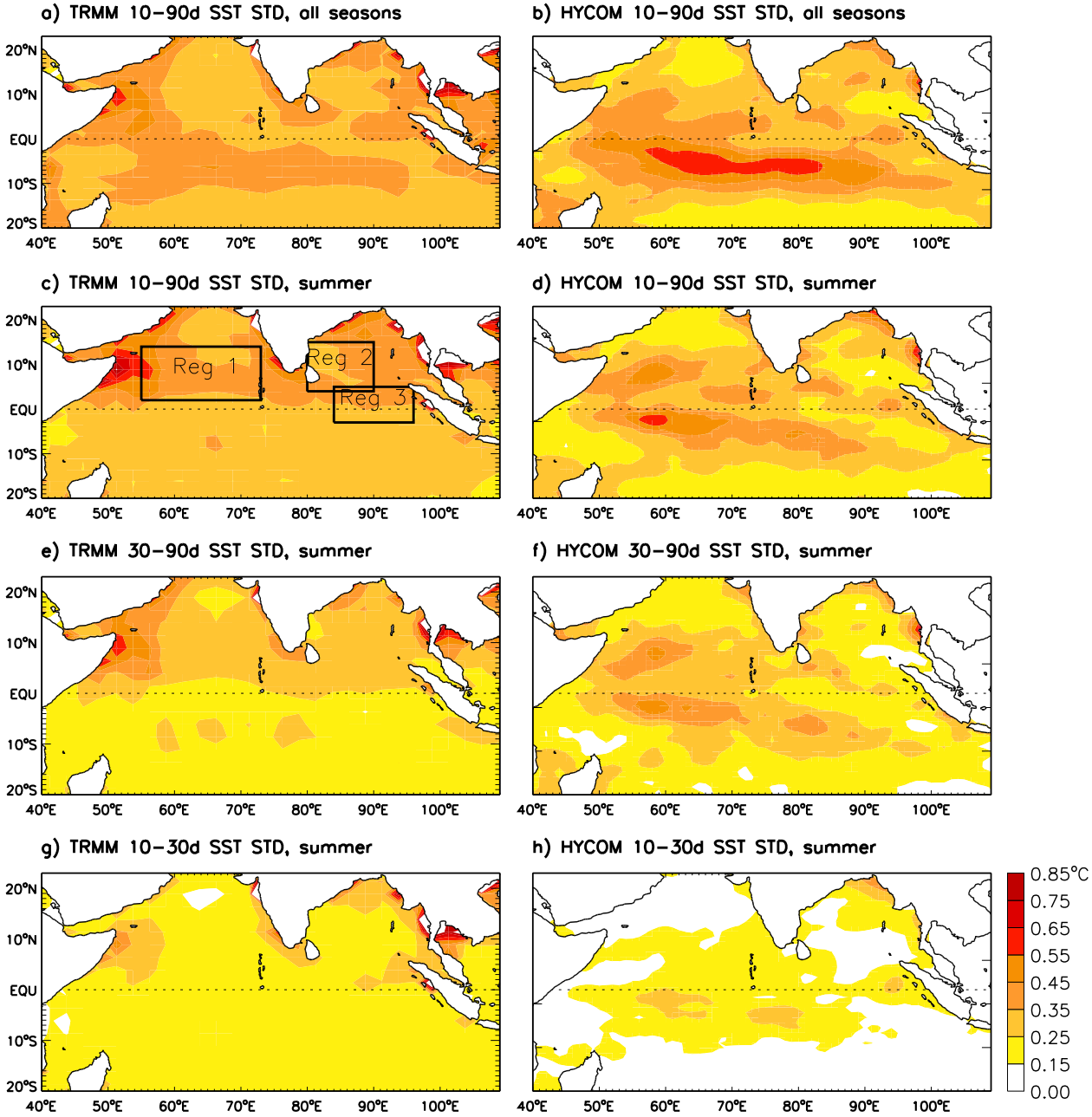

that are identified as having large variability in winds, OLR, and SST (Figures 3.4 and 3.6). Region 1 is located in the central AS (55-73°E, 2-14°N), Region 2 is in the western BOB (80-90°E, 4-15°N), and Region 3 is in the eastern equatorial IO warm pool (84-96°E, 3°S-5°N). Figure 3.7 provides a time series of intraseasonal SST in each region from 2000-2003, as observed by TRMM (thick solid line) and as simulated by HYCOM MR (dashed line) and by HYCOM MR - EXP1 (thin solid line), which represents the SST forced by ISOs only. Model-data correlations for regions 1, 2, and 3 are 0.66, 0.65, and 0.69 respectively, with significance above 95%. Note that the significance test takes into account the reduced degree of freedom due to the filter [Livezey and Chen, 1983]. These correlations are lower than those from the ITCZ region used in the wintertime study [Han et al., 2007], but they are similar in magnitude to those from the warm pool and the AS in the same study. Looking at events with magnitudes larger than 1 STD, HYCOM performs reasonably well, although it occasionally over- or under-estimates SST changes. MJO-scale events are simulated well by HYCOM, with model-data correlation coefficients of 0.71, 0.70, and 0.76 in regions 1, 2, and 3, respectively (Figure 3.8a for region 2), while submonthly events have somewhat lower model-data correlations (Figure 3.8b for region 2).

The variance spectra of summertime TRMM and HYCOM MR SST anomalies from 1999-2003 provide an additional look at HYCOM's performance in each of the three regions (Figure 3.9). To do this, we average the TRMM and HYCOM MR summertime SST time series over each region, and then perform a spectral analysis in which the annual and semiannual cycles are removed. The variance spectra of the two datasets generally agree well in all three regions, with some exceptions. The most notable model/data difference occurs in the BOB (Figure 3.9b), where a strong 90-day peak appears in the HYCOM solution but not in the TRMM data.

Overall, HYCOM reasonably simulates SST in the three chosen regions. Existing discrepancies may be due to model errors, data errors, uncertainties in the model forcing fields, and differences between TRMM skin temperature and the model bulk temperature. Model-data differences in coastal regions may be due to the artificial interpolation of QuickSCAT winds to land where their values are zero [Han et al., 2007]. Differences may also be due to the model's thick mixed layer

Figure 3.7: (a) Time series of 10-90 day SST averaged over Region 1 (AS) in Figure 3.6c, from 2000-2002. The thick solid and dashed lines represent the TRMM and HYCOM MR SSTs, respectively. The thin solid line represents the SST from HYCOM difference solution MR - EXP1, which isolates the effect of ISOs only. The horizontal dashed line represents the STD of TRMM SST. Correlation coefficients between SSTs from HYCOM MR and TRMM (r) and HYCOM MR - EXP1 (r_m) are calculated for the years 1999-2003 and displayed. (b) Same as *a* but for the BOB Region 2 in Figure 3.6c. (c) Same as *a* but for the warm pool Region 3 in Figure 3.6c. Units are °C.

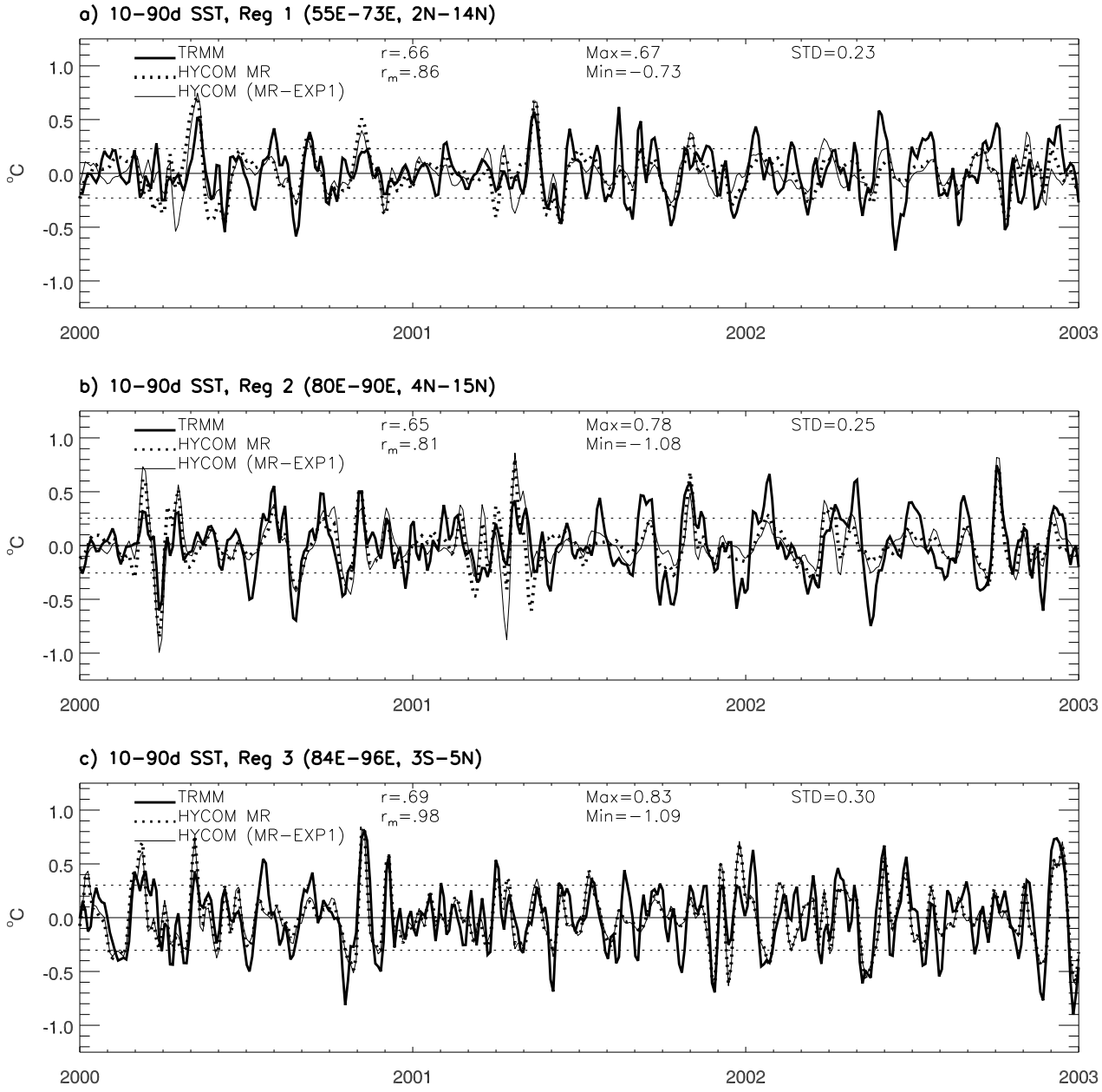

Figure 3.8: (a) Same as figure 3.7b, except band-pass filtered to 30-90 days. (b) Same as *a*, but band-pass filtered to 10-30 days. Units are °C.

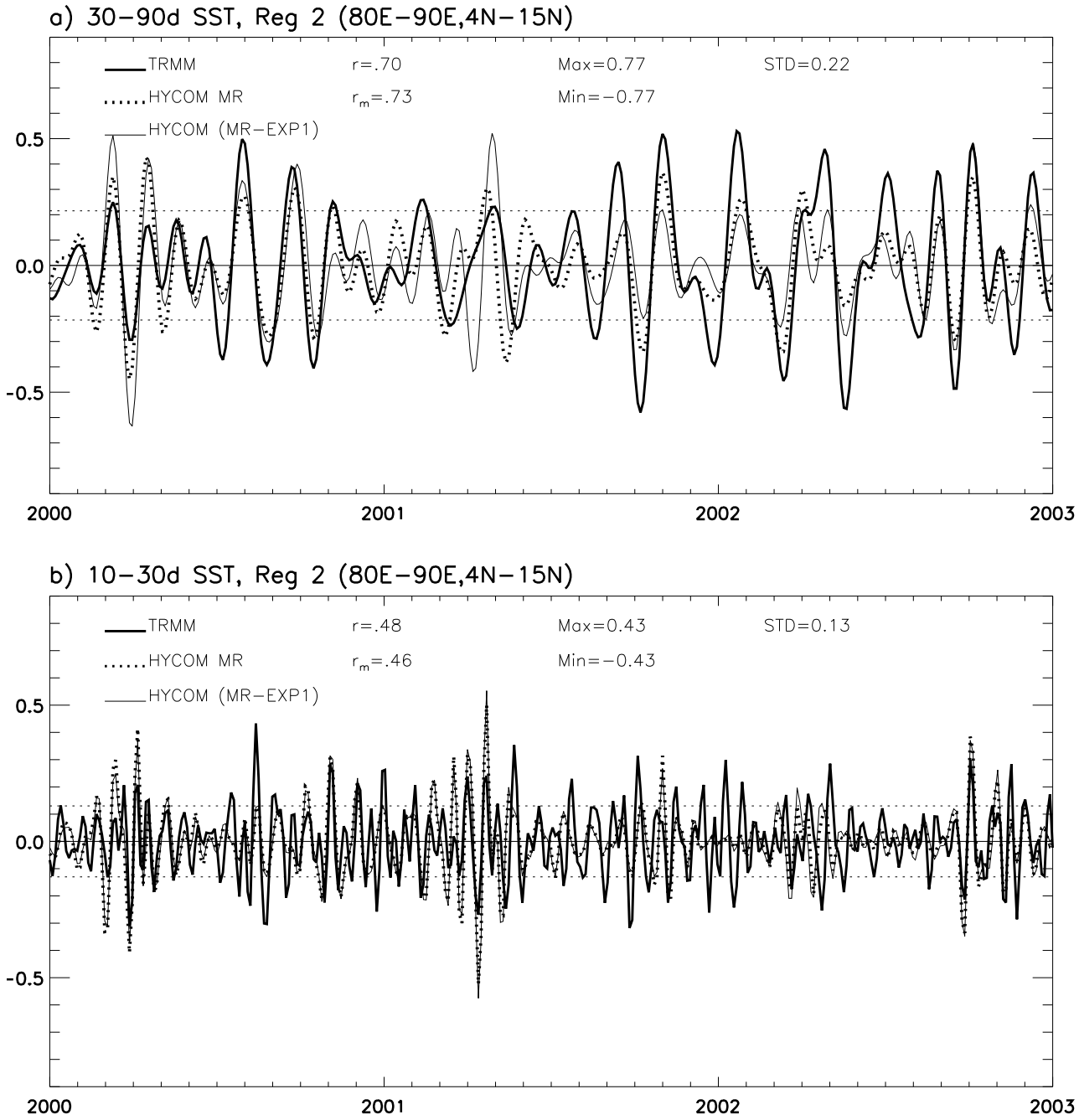

Figure 3.9: (a) Variance spectra of observed TRMM SST (thick solid line) and modeled HYCOM MR SST (thick dashed line) during summer days from 1999-2003, averaged over the AS (Region 1). The thin solid/dashed lines show the 90% significance level for each. (b) Same as *a*, but for the western BOB (Region 2). (c) Same as *a*, but for the eastern equatorial warm pool (Region 3). Units are °C.

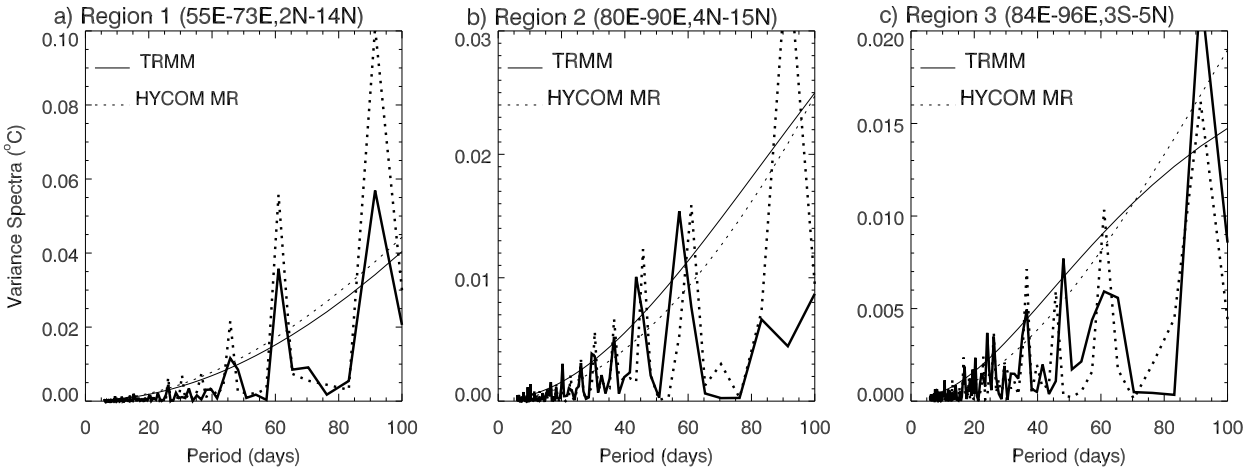

and deep thermocline, a topic which is investigated in more detail in Section 3.4.5.1.

Amplitudes of the SST variability shown in Figure 3.7 are large, with maximum warming (cooling) of 0.83°C (1.09°C) in the eastern equatorial IO warm pool, 0.78°C (1.08°C) in the BOB and 0.67°C (0.73°C) in the AS. Even small SST changes in these regions can have a very important effect on convection because mean summer SSTs there exceed 28-29°C (Figure 3.5). At such a high SST, small temperature changes can have large impacts on convection [Fu et al., 1994; Bajuk and Levoy, 1998; Del Genio and Kovari, 2002].

3.4.3 Impact of Atmospheric ISOs

Of particular interest is that while winds and OLR variations are larger during submonthly events (Figure 3.4), amplitudes of summer SST variability are larger during MJO events (Figure 3.6). This is true even in the BOB, where submonthly ISOs are much stronger than the MJO-scale ISOs. The BOB-averaged STDs of observed TRMM 30-90 day and 10-30 day SSTs are 0.29°C and 0.20°C, respectively. The same is true during winter, as discussed in Han et al. [2007]. Following the discussion in Han [2005], this skew of frequency between the peak forcing and response is likely because it is the time derivative of SST, rather than the SST itself, that is proportional to the strength of the forcing. Total changes in SST during an event are found by integrating the forcings over the event duration. That is, even though the amplitude of submonthly forcing is larger than that for the MJO, it does not act on the ocean long enough to cause as large an SST change as is induced by the MJO forcing.

Intraseasonal SST changes can also result from oceanic internal variability [Jochum and Murtugudde, 2005; Han et al., 2007]. In this study, we focus on understanding air-sea interactions related to ISOs. The high correlation coefficients (0.81-0.98) between 10-90 day SSTs from the MR (due to both ISO forcing and internal variability) and the difference solution, MR - EXP1 (mainly due to ISO forcing), demonstrate the dominance of ISO forcing (Figure 3.7). HYCOM MR and the difference solution can occasionally differ significantly, likely because of internal variability. This is in agreement with Waliser et al. [2004], who found that ISO forcing dominates instabilities

over the IO.

3.4.4 Processes: General Analysis

A time series of intraseasonal SST changes caused by SW radiation, precipitation, and wind (via entrainment, turbulent heat fluxes, advection, and upwelling) is calculated for each region over both MJO and submonthly timescales. Due to the high degree of similarity for all regions, only region 2 (the BOB) is shown in Figure 3.10. In all regions, SST variability on both MJO and submonthly timescales is dominated by wind (red line of Figures 3.10a,c), while the effects of SW radiation and precipitation (blue and yellow curves) are weak. On 30-90 day timescales, correlation coefficients between the total SST change due to all ISO forcings (black curve in Figure 3.10a) and due to the total wind (red curve) is 0.95 in the AS, 0.93 in the BOB, and 0.96 in the eastern equatorial IO. On 10-30 day timescales, the correlations are the same as shown above (Figure 3.10c). The high correlation coefficients demonstrate the deterministic role played by winds in causing summertime intraseasonal SST variability, as during wintertime [Han et al., 2007].

Different from the winter, when the largest SST change occurs in the ITCZ and equatorial regions due almost equally to both oceanic upwelling and advection associated with changes in wind stress (see section 3.3.3) and turbulent heat fluxes and entrainment cooling associated with changes in wind speed [Han et al., 2007], the strongest summertime variability in the BOB is mostly due to wind speed, with wind stress playing a lesser role (Figures 3.10b,d). Entrainment and turbulent heat fluxes due to changes in wind speed have an apparently larger effect than upwelling and advection on SST variability for almost every MJO and submonthly-scale event, albeit to a lesser extent for submonthly ISOs (Figure 3.10d). The MJO-scale (submonthly) SST correlation coefficient between total wind and wind speed forcing is 0.93 (0.90), while that for wind stress is 0.77 (0.84). The reasons for the importance of wind speed in the BOB will be discussed in Section 3.4.5.1.

In the AS, wind speed also has a larger effect than wind stress on MJO-scale SST variability (Figure 3.11a), with a correlation coefficient of 0.95 between the SSTs induced by total wind

Figure 3.10: (a) Time series of 30-90 day SST averaged over Region 2 (the BOB), forced by total ISOs (MR - EXP1, black curve), total wind (MR - EXP4, red curve), SW radiation (MR - EXP5, blue curve), and precipitation (MR - EXP6, green curve) from 1999-2003. (b) Same as *a* but for SST caused by wind stress (MR - EXP3, solid black curve), wind speed (EXP3 - EXP4, dashed curve), and total wind (MR - EXP4, red curve). (c) Same as *a* but for 10-30 day SST. (d) Same as *b* but for 10-30 day SST. Standard deviations (STD) of SST changes due to all forcings, wind speed and stress forcings, SW radiation, and precipitation are displayed in the figures, along with the correlation coefficients (r) between total SST changes and those due to each process. Units are °C.

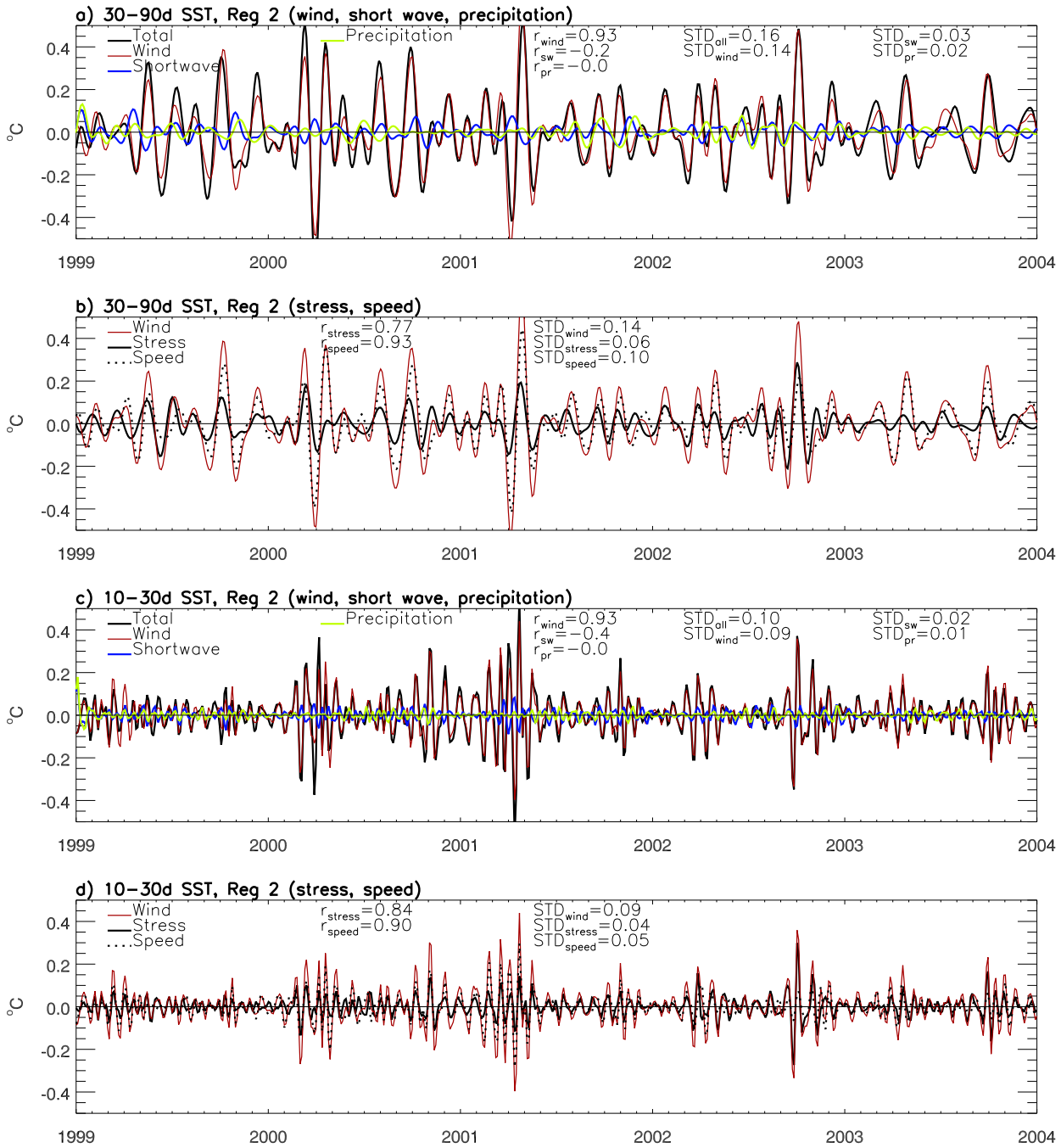

and wind speed, and 0.84 between total wind and stress forcing. On submonthly timescales, SST variability in the AS results almost equally from wind stress and wind speed (Figure 3.11b). In the warm pool (region 3), wind speed and stress (Figures 3.11c,d) seem to contribute almost equally on both submonthly and MJO timescales. This is also true in the equatorial region surrounding the Maldives (not shown), where wind forcing is strong on submonthly timescales (Figures 3.4f,i).

In studying specific MJO and submonthly events (see below), it is clear that SW radiation and precipitation can make non-negligible contributions to overall SST variability in some regions. The ratios STD_{SW}/STD_{all} and STD_{pr}/STD_{all}, which measure the ratio of SST STD forced by total ISOs and by SW radiation and precipitation only, are calculated using STD values for each region and for each timescale. SW forcing has the largest relative amplitude in the warm pool on both MJO (ratio=0.22) and submonthly (ratio=0.23) scales. Precipitation has the largest relative amplitude in the BOB for MJO timescales (ratio=0.125) and in the warm pool for submonthly scales (ratio=0.154).

The overarching dominance of winds on ISO-induced SST variability is in agreement with winter events [Han et al., 2007] and with Waliser et al. [2004]'s study of boreal summer canonical ISOs. The latter study, however, found that SW effects can be more important in the IO than is found here. Perhaps this discrepancy is partly due to the use of canonical ISOs, rather than the observed events studied here, or partly due to the $\sim$14% underestimation of SW fluxes by the ISCCP data (Figure 3.3). The apparent importance of wind speed processes over wind stress processes in the BOB, and to a lesser degree in the AS, appears to be different from Schiller and Godfrey [2003], who suggested the importance of precipitation due to the barrier layer effect [Lukas and Lindstrom, 1991; Sprintall and Tomczak, 1992]. These aspects will be further discussed for specific ISO events below.

3.4.5 Specific Events and Composite MJO

To reveal the spatial patterns of SST induced by ISOs in the IO, strong MJO and submonthly cooling events are identified using Figure 3.8. The term "strong" refers to events during which the

Figure 3.11: (a) Same as Figure 3.10b, but for Region 1 (AS). (b) Same as Figure 3.10d, but for Region 1. (c) Same as *a* but for Region 3 (eastern equatorial IO warm pool). (d) Same as *b* but for Region 3. Units are °C.

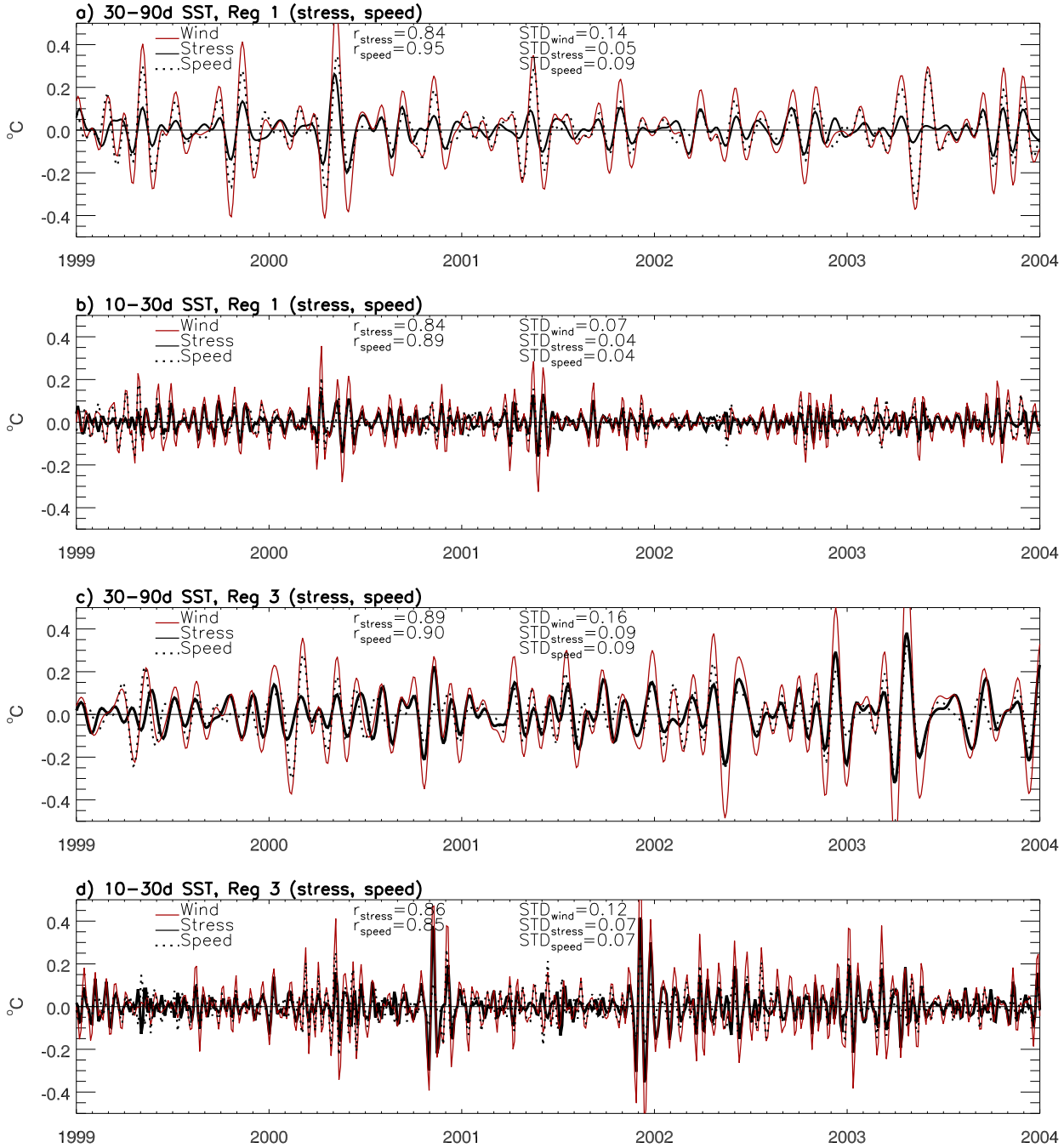

maximum SST cooling is larger than 1 STD. Although cooling is used to choose the events, we examine the full life cycle of each. Thus, the warming phase of each chosen intraseasonal SST event is also investigated. While many cases are evaluated, we choose two representative cases for 30-90 day and submonthly SST variability and discuss the common features below.

3.4.5.1 A Strong MJO Event

A strong MJO-scale event is identified based on the BOB time series (Figure 3.8a), but can also be seen in the warm pool and in the AS. The peak BOB cooling occurs on 25 August 2000, with subsequent warming on 21 September 2000 (Figure 3.12). HYCOM simulates the SST variations well, with warm and cold anomalies shown in similar locations and with similar magnitudes as those observed by TRMM (middle and right columns of Figure 3.12). For example, cool SSTs in the northern BOB and AS appear in both the TRMM data and the HYCOM solution on 3 and 12 September, with warm SSTs off the west coast of India and across the equatorial IO. TRMM SST anomalies in the BOB are typically larger than those modeled by HYCOM, an artifact that could be due to the modeled mixed layer being thicker than observed in the BOB, as investigated below.

Interestingly, temporal evolution of the event shows that strong convection (negative OLR anomaly, left column of Figure 3.12) and its associated winds, together with cool SSTs, appear to move northward from the equator to the Indian and Asian subcontinents during 7-25 August. Before cooling arrives in the BOB (7 August), wind anomalies are northeasterlies in the BOB and AS, westerlies in the equatorial region, and northwesterlies in the south AS. As the event develops (16 August), anomalous winds become southwesterlies in both the BOB and AS. On 25 August, the peak cooling day, winds are strong southwesterlies in the northern hemisphere and easterlies along the equator. After the cooling event has completely passed through the IO basin (21 September), winds are generally as they were on 7 August. The anomalous SST apparently lags the convection and winds. While increased convection arrives at the northern AS and BOB on 16 August, cool SST anomalies remain near the equator in the south AS and BOB. By 25 August and 3 September when strong convection moves to the northern Bay and then to the Indian subcontinent, strong

Figure 3.12: (left) The 30-90 day filtered QuickSCAT wind stress (arrows) and OLR (shading) for an MJO event from 7 August - 21 September 2000 at a 9 day interval. (middle) TRMM 30-90 day SST for the same period of time. (right) HYCOM MR 30-90 day SST for the same period of time. SST contour intervals are 0.2°C, while OLR contour intervals are 5 Wm^{-2}. Units are dyn cm^{-2} for wind stress.

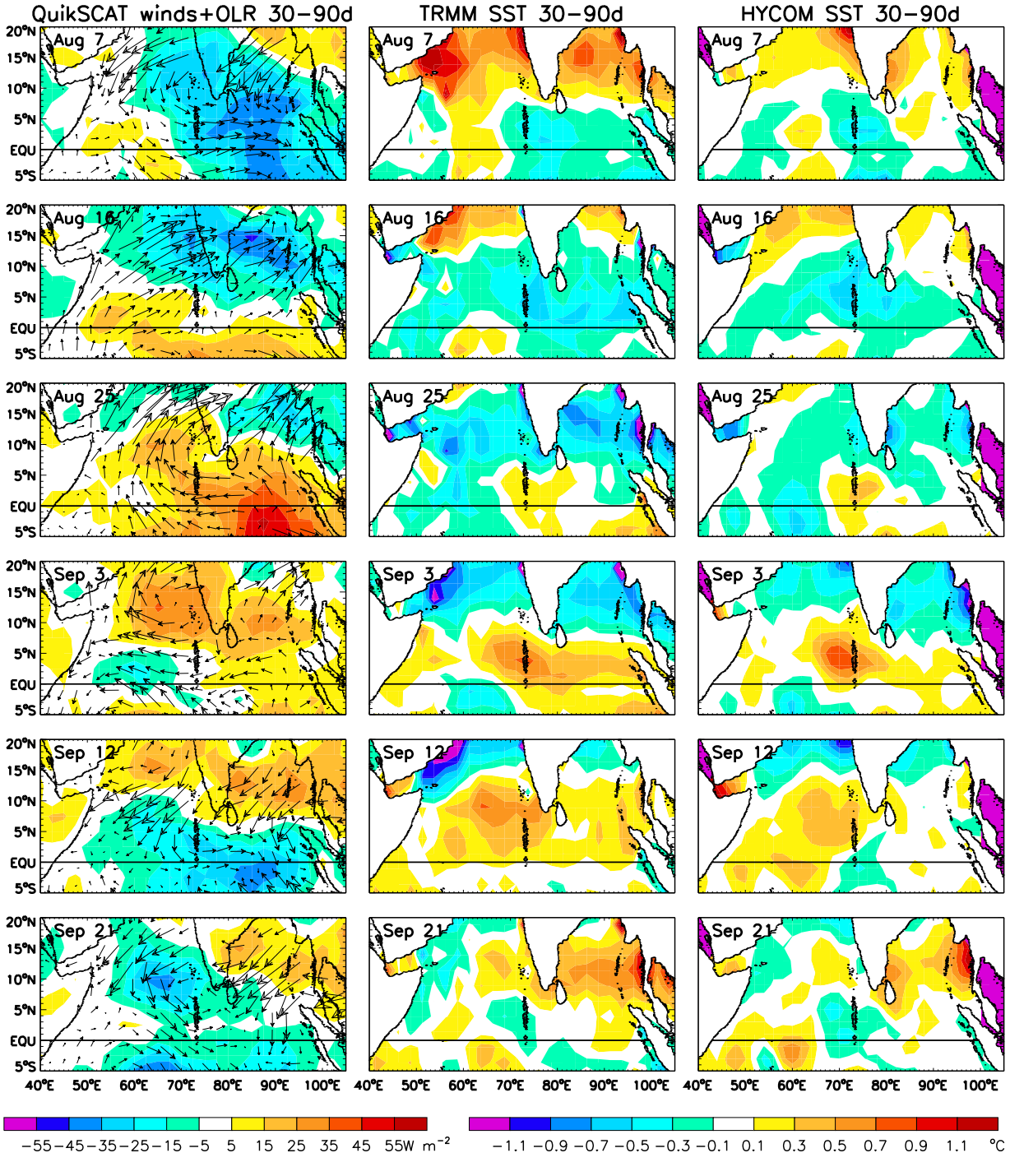

negative SST anomalies first appear in the south-central and then northern parts of the two basins. This delay is in agreement with Bhat et al. [2001] and Webster et al. [2002].

Consistent with the general analysis in Section 3.4.4, wind effects dominate over SW radiation and precipitation during this MJO event (Figures 3.13a-b versus c-d, i-j, and k-l), and wind speed plays a larger role than wind stress in the BOB (Figures 3.13c-d versus e-f, g-h). On both 25 August and 21 September 2000, (the event peak cooling and warming days), wind speed is the strongest forcing in the BOB. While wind stress also plays a role in causing SST anomalies there, its effect is smaller in both geographic extent and magnitude. SW radiation can be important for specific cases in specific regions, especially in the BOB, as suggested by Han et al. [2006b].

During the peak cooling phase of this event (25 August), the anomalous southwesterly winds in the BOB and AS (Figure 3.12, left column) enhance the mean southwest monsoon winds (Figure 3.5) and produce positive wind speed anomalies (Figure 3.13e, solid black contours). The strengthened winds enhance turbulent heat fluxes and result in negative heat flux anomalies (Figure 3.14c), producing the surface cooling. In contrast, during the warming phase the reduced wind speed (Figures 3.5, 3.12, and dashed contours of 3.13f) produces a positive heat flux anomaly (Figure 3.14d) and thus warms the sea surface. In the AS, the stronger (weaker) wind speed increases (decreases) entrainment cooling (see Section 3.3.3), and thickens (thins) the mixed layer (Figures 3.14a,b), contributing to the surface cooling. In the BOB, however, entrainment cooling appears to be negligible because the hm stays almost unchanged. As a result, intraseasonal SST variability in the BOB predominately results from surface heat flux due to intraseasonal winds. This is likely because the warm, fresh river runoff and strong precipitation in the BOB increase the stratification and reduce the entrainment rate there [Han et al., 2001; Howden and Murtugudde, 2001]. The increased stratification is due mostly to salinity, because the warm, fresh river runoff causes a sharp halocline gradient, while the thermocline gradient is not sharp. The halocline gradient causes a shallow pycnocline, and thus a thinner surface mixed layer than elsewhere in the IO (Figures 3.15a,b). Because the thermocline gradient is not as sharp, the thermocline is deeper than the pycnocline and the mixed layer. This layer of still warm water below the mixed layer is the barrier

Figure 3.13: The 30-90 day filtered SST for (left) 25 August and (right) 21 September 2000 from a suite of HYCOM difference solutions designed to isolate processes. (a and b) SST forced by the MJO (30-90 day filtered MR - EXP1). (c and d) SST forced by the MJO wind (speed plus stress; MR - EXP4). (e and f) SST forced by the MJO wind speed only (EXP3 - EXP4). Overlying the SST is the 30-90 day wind speed (line contours) 6 days before the SST. Dashed lines show negative values (weak wind speed), and solid lines are positive values (strong wind speed). (g and h) SST forced by the MJO wind stress (MR - EXP3). Overlying the SST is the 30-90 day Ekman pumping velocity (w_E). See text for equation and definition. Positive values (upwelling) are solid, and negative values (downwelling) are dashed. (i and j) SST forced by the MJO SW radiation (MR - EXP5). (k and l) SST forced by the MJO precipitation (MR - EXP6). Units are °C for SST, ms^{-1} for wind speed, and 10^{-6} ms^{-1} for w_E.

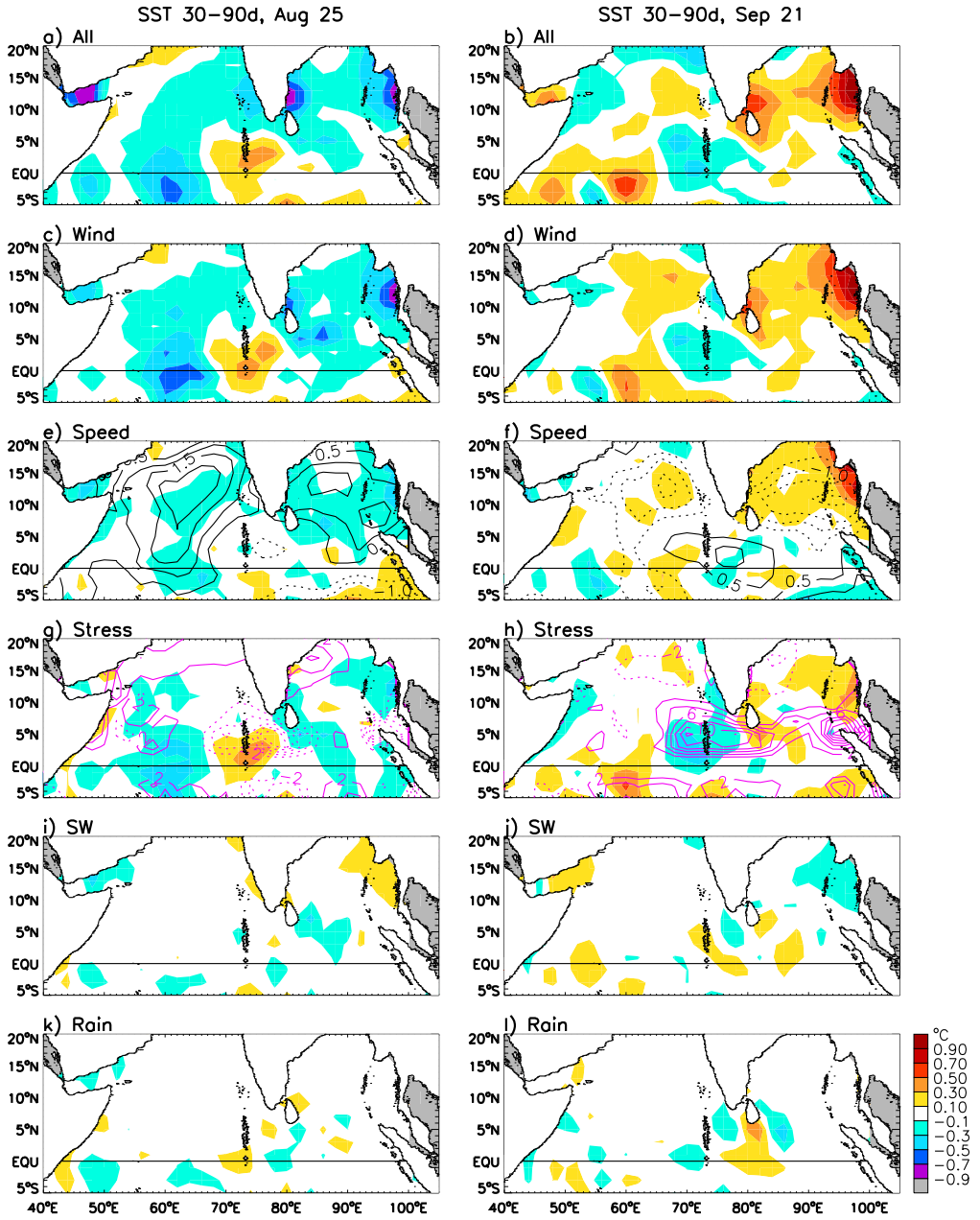

layer [Sprintall and Tomczak, 1992], and it is present both in HYCOM MR results and in Levitus and Argo observations (Figures 3.15c-f). The Argo float data used here is taken only from floats in the BOB (Region 2; See Figure 3.7c) with delayed-mode, scientific quality data. The longest continuous time series of data available during the study period is used, extending from August 2002 - November 2004. As few as 5 floats are available in August 2002, while as many as 15 floats meet the criteria during October 2004. The temperature and salinity data from all chosen Argo floats is averaged over each month of the time series to create monthly mean observations for the BOB. As a result of the barrier layer, even if entrainment is occurring, it will not affect SST appreciably because the warm barrier layer water is entrained to the surface. The modeled barrier layer thickness is similar to that observed in Argo float data (Figures 3.15e,f). HYCOM's mixed layer, however, is thicker than the Levitus and Argo data in the BOB and in the AS (Figures 3.15 a,b, and e,f). Atmospheric forcings acting on this thicker mixed layer result in modeled SST variability in the BOB and AS that is generally smaller than in the TRMM data (Figures 3.7, 3.8, and 3.12). Conversely, HYCOM's mixed layer is thinner than observed from 70°E-80°E and EQ-5°S (Figures 3.15 a,b). As a result, the modeled SST response in this region is often stronger than observed (Figure 3.12).

Wind stress affects the SST (Figures 13g,h) by anomalous upwelling due to changes in Ekman pumping velocity (w_E) and by anomalous advection. The w_E (line contours in Figures 13g,h) is calculated with the following equation:

$$w_E = \frac{\partial}{\partial x}\left(\frac{\tau^y}{f}\right) - \frac{\partial}{\partial y}\left(\frac{\tau^x}{f}\right) \tag{3.1}$$

where τ_x and τ_y are the zonal and meridional wind stress, and f is the Coriolis parameter. In addition to wind speed, wind stress also plays an important role in the south-central AS (Figures 3.11a and 3.13g,h). In the southeast AS near the Maldives Islands, the effects of wind stress dominate wind speed. The anomalously warm (cold) SSTs agree well with the negative (positive) w_E anomalies there (Figures 3.13g,h). Anomalous horizontal advection due to wind stress is estimated using:

Figure 3.14: (a) Mixed layer thickness (hm) from HYCOM difference solution EXP3 - EXP4 (wind speed only), filtered to 30-90 days for an MJO event peak BOB cooling day (25 August 2000). Units are m. (b) Same as *a*, but for an MJO event warming day (21 September 2000). (c) Surface turbulent heat flux during an MJO event peak cooling day, from HYCOM 30-90 day difference solution EXP3 - EXP4 (wind speed only). Units are Wm^{-2}. (d) Same as *c*, but for an MJO event end day.

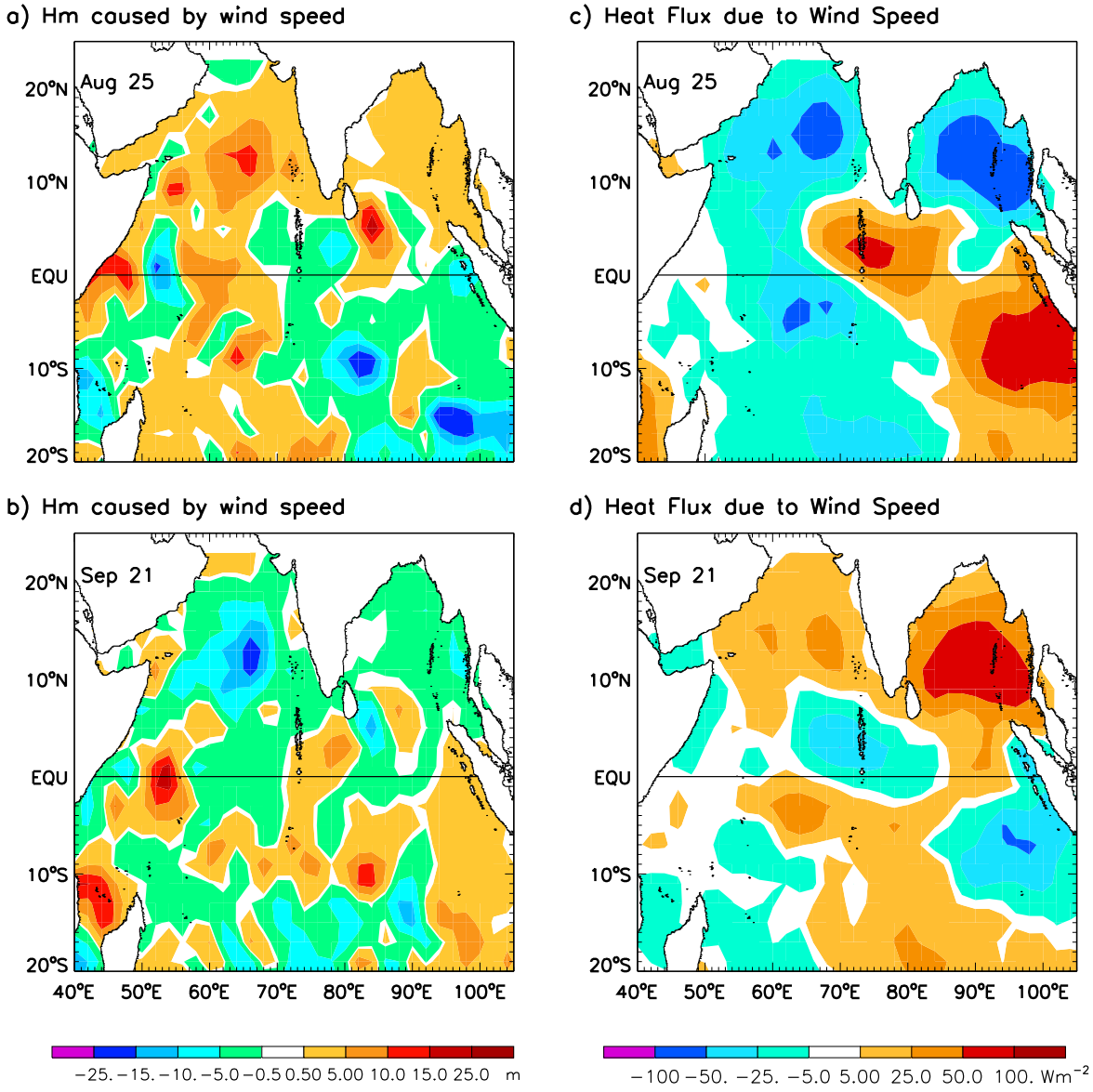

Figure 3.15: (a) HYCOM MR hm averaged over the summer months (May-October) from 1999-2003. (b) Same as *a*, but for Levitus data. (c) HYCOM average summertime barrier layer thickness from 1999-2003. Calculated using HYCOM MR mixed layer depth and the depth at which temperature decreases by 0.5°C ($T_{0.5}$). (d) Time series of Argo monthly averaged barrier layer thickness, August 2002 - November 2004, in Region 2 (BOB). The difference between the hm (solid line) and $T_{0.5}$ (dotted line) is the barrier layer thickness. The hm is calculated as the depth at which the density decreases by the equivalent of 0.5°C. (e) HYCOM mean vertical temperature (solid line) and salinity (thick dotted line) profiles for an MJO event in Region 2 (BOB) from 7 August - 21 September 2000. Horizontal lines indicate the calculated hm (dashed line) and $T_{0.5}$ (dot-dash line). The distance between hm and $T_{0.5}$ is the barrier layer. (f) Same as *e*, except using Argo float data. Units for all figures are m, except *d* and *f*, which are in dbar.

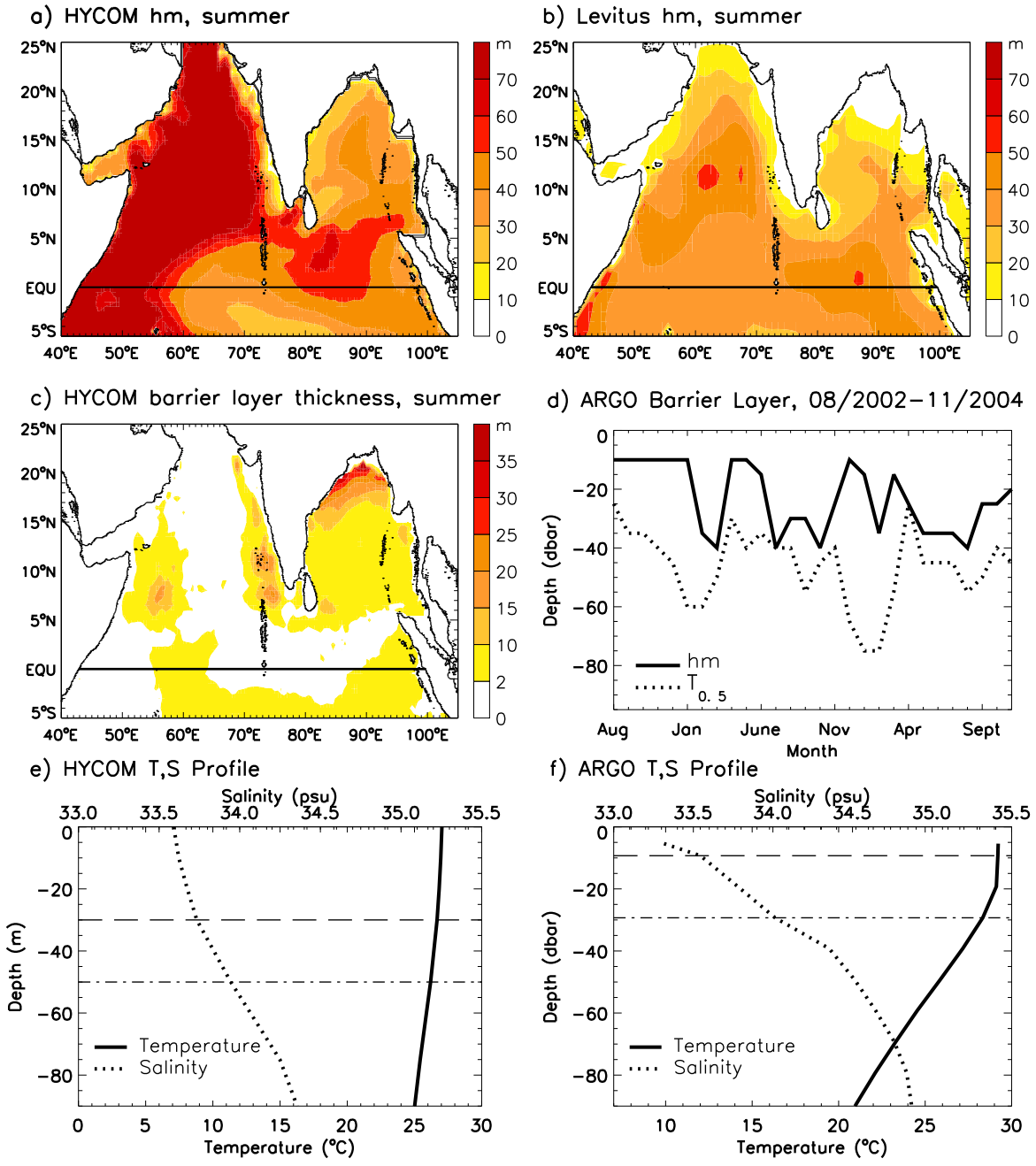

$$\Delta T = -\left[u\frac{\partial T}{\partial x} + v\frac{\partial T}{\partial y} + \overline{u}\frac{\partial \overline{T}}{\partial x} + \overline{v}\frac{\partial \overline{T}}{\partial y}\right]\Delta t \tag{3.2}$$

where u, v, and T are zonal and meridional currents and SST, respectively, from HYCOM solution MR. Terms with overbars are the same, but taken from HYCOM solution EXP3 that is forced by low-passed wind stress, and Δt is 3 days. Our results show that horizontal advection contributes little to the SST variability during this event (not shown).

SST variations reach their maxima in the eastern equatorial IO warm pool on 16 August and 3 September, which leads the maximum SST variability in the BOB (Figure 3.12). In this region, SST variability is also controlled by winds, with wind stress and speed playing equally important roles (not shown).

3.4.5.2 MJO Composite

A composite MJO event is constructed (Figure 3.16), consisting of 5 separate strong summer MJO cooling events that can be seen in both TRMM and HYCOM MR SST records (Figure 3.8a). Each event is also associated with subsequent strong warming in both records. The peak cooling dates for the 5 events are 8 June 1999, 25 August 2000, 14 October 2000, 6 October 2001 and 15 September 2002. Both the OLR (left column of Figure 3.16) and the associated SST from TRMM and HYCOM MR (middle and right columns of Figure 3.16) bear a remarkable resemblance to Figure 3.12, except that the amplitudes are weaker in the composite. This is likely because, at least partly, each MJO event has a somewhat different structure than the others, and the composite averages out some strong peaks. While the composite provides a general picture of the MJO and its impact, these results suggest that analysis of specific events is also necessary to obtain a more complete understanding of the impact of MJO events. The MJO composite TRMM and HYCOM MR SSTs in Figure 3.16 also show the northeastward motion associated with individual MJO events (Figure 3.12). Process studies for the individual MJO events that contribute to the composite show that the relative importance of SW radiation, precipitation, and winds are consistent between the

events. The conclusions from our detailed study of an MJO event, then, hold for the MJO composite.

3.4.5.3 A Strong Submonthly Event

HYCOM does not model submonthly events as well as it models MJO events, a point highlighted by the lower 10-30 day model-data correlation coefficients in Section 3.4.2 and further discussed below. It is important to note that the model forcings are 3-day mean fields, which prevents HYCOM from resolving sub-weekly variability. A strong submonthly ISO cooling event overlaps with the previously discussed MJO event, occurring from 19 August - 3 September 2000, with peak cooling in the BOB on 25 August (Figure 3.17). HYCOM is able to capture major areas of cooling and warming in the BOB, the warm pool and the AS, albeit with apparent underestimations in amplitudes, particularly in the AS (middle and right columns of Figure 3.17). On 22 and 25 August, regions of cooling observed by TRMM in the BOB, near the warm pool, and in the eastern AS are all modeled reasonably well, with some discrepancies in magnitude and geographic extent. Subsequent warming in the BOB and eastern AS is well simulated by HYCOM. As is expected from our general results, cooling is not as pronounced during this submonthly event as it is during the MJO event, even though the submonthly convection and winds are stronger. Cooler (warmer) SSTs are observed and modeled in the southeastern AS mini warm pool region [Rao and Sivakumar, 1999] on 25 August (3 September). This SST variability in the mini-warm pool area (Figures 3.5 and 3.17) may have important implications for monsoon onset prediction [Rao and Sivakumar, 1999].

Prior to the submonthly event's peak cooling in the BOB (19 and 22 August), winds in the northern AS and in the northern BOB are northeasterlies, which act to weaken the mean summer monsoon winds (Figure 3.5) and thus increase SST (top middle and right panels of Figure 3.17). Meanwhile, westerly winds prevail in the south AS, along the equator, and in the southern BOB, which enhances the mean monsoon winds and coincides with cooler SST anomalies (Figures 3.5 and 3.17). Strong convection first appears in the eastern equatorial warm pool and south of India

Figure 3.16: (left) The 30-90 day filtered QuickSCAT wind stress (arrows) and OLR (shading) for an MJO composite event at a 6-day interval with respect to the date of peak BOB cooling (d0). (middle) TRMM 30-90 day SST for the same period of time. (right) HYCOM MR 30-90 day SST for the same period of time. SST contour intervals are 0.1°C, while OLR contour intervals are 5 Wm^{-2}. Units are dyn cm^{-2} for wind stress.

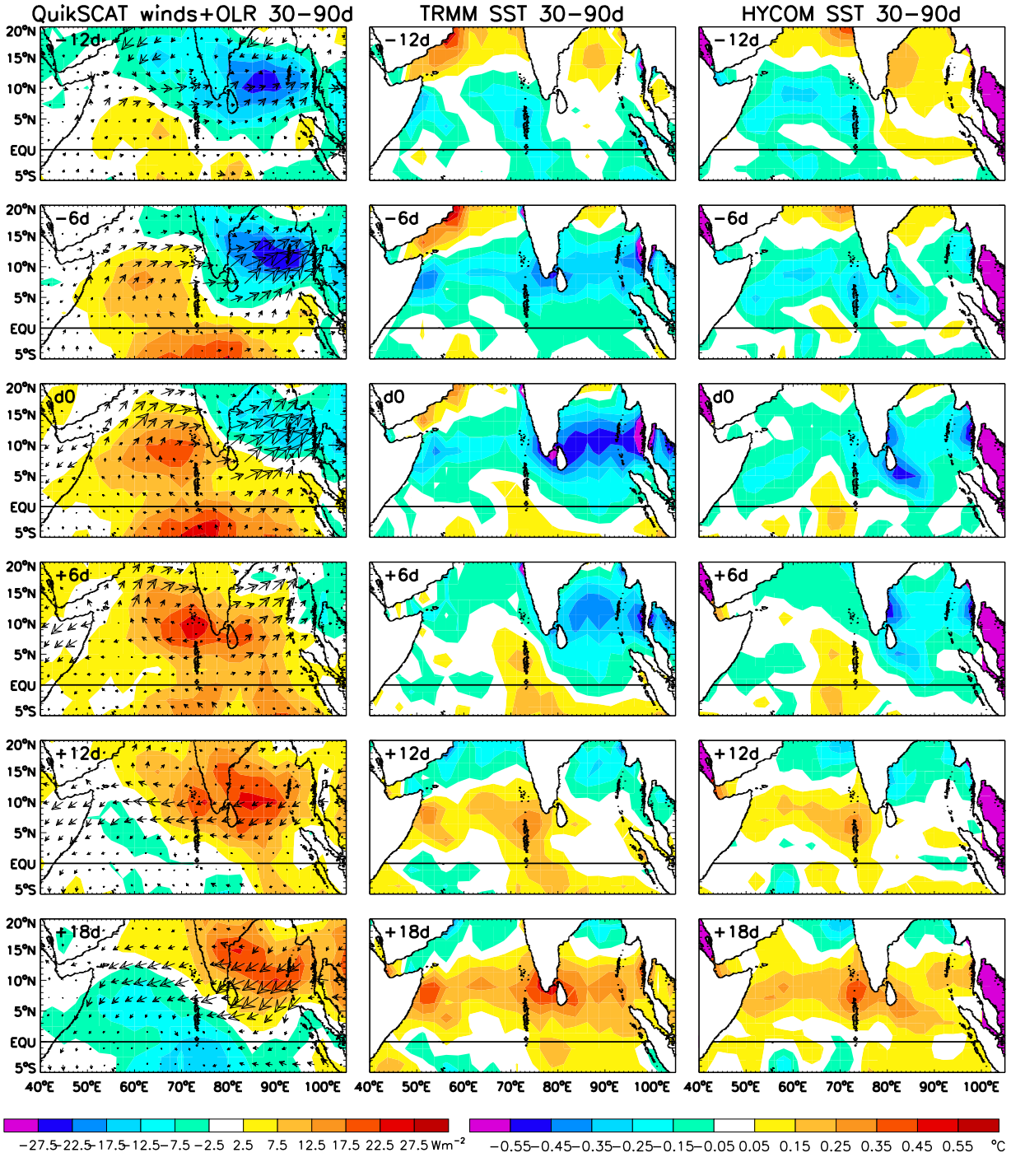

Figure 3.17: Same as Figure 3.12, but for a submonthly event from 19 August - 3 September 2000, filtered to 10-30 days, and displayed at a 3 day interval with SST contour intervals of 0.1°C.

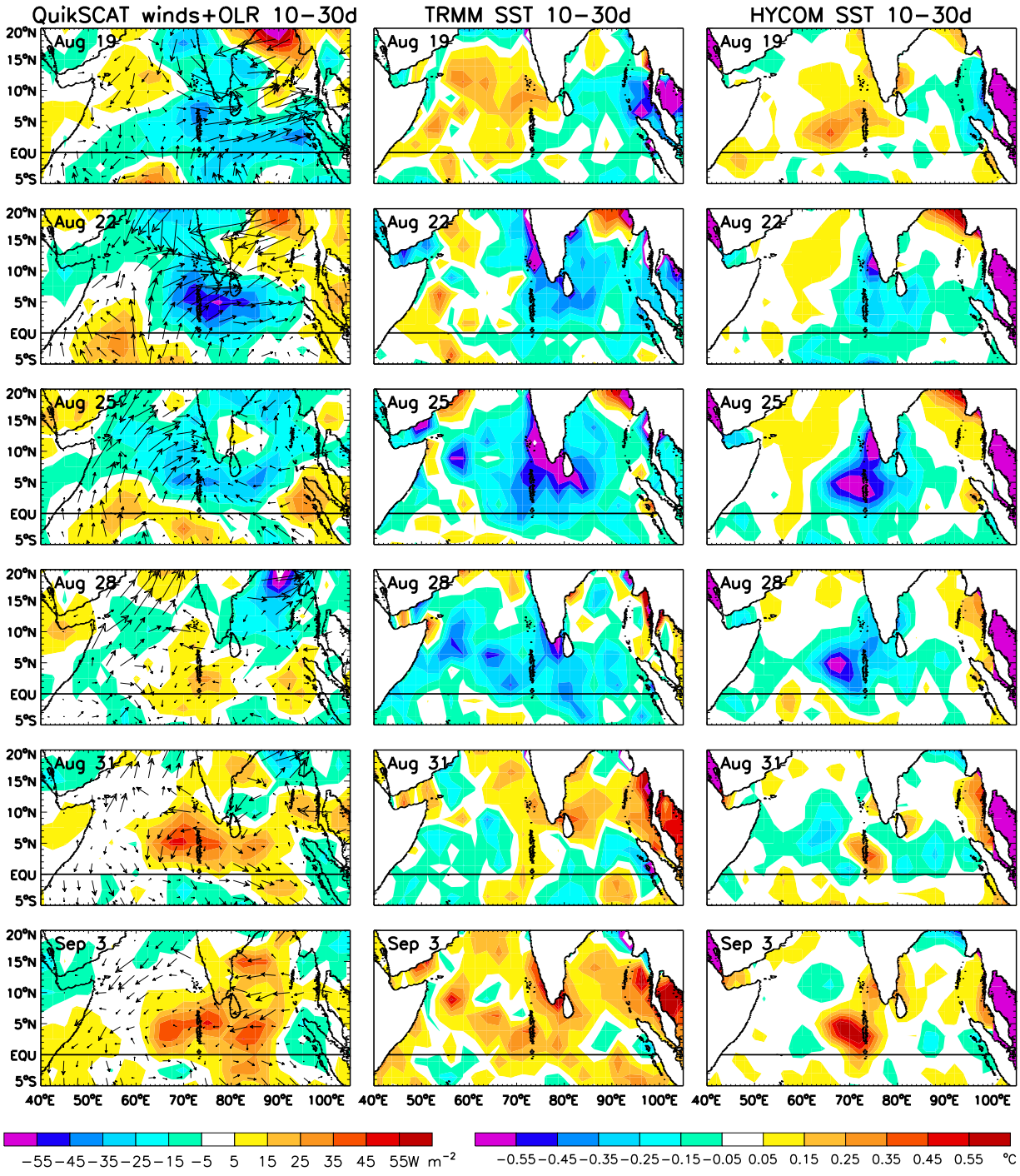

on the 19th, and then obtains its maximum strength in the mini-warm pool region on the 22nd. On the peak cooling day of 25 August, winds in the south AS become southwesterlies, which enhances the mean monsoon and extends the cooler SST anomaly westward into the central AS. At the same time, winds in the BOB are weak with complex spatial structure. Later in the month, the anomalous southwesterlies in the AS weaken (28 August) and then reverse on the 31st, which corresponds with warmer SSTs there. Again, SST changes appear to lag the wind and convection variability (Figure 3.17). The spatial structures of the submonthly ISO and its associated SST show evident differences from those of the MJO. The strongest cooling produced by the submonthly ISO occurs in the mini-warm pool of the eastern AS, south of India and in the western BOB (Figure 3.17), whereas the strongest cooling associated with the MJO is present across the AS and BOB (Figure 3.12). Wind effects again dominate SW flux and precipitation in generating the submonthly SST variability; effects of surface heat flux and entrainment cooling due to changes of wind speed are comparable to the upwelling and advection induced by variations of wind stress (figure not shown).

3.5 Summary and Conclusions

In the present study, we use satellite observed OLR and QuickSCAT winds to document the MJO and submonthly ISOs during boreal summer. A hierarchy of experiments is performed using HYCOM (Table 3.1) to better understand the processes that contribute to intraseasonal SST variability. As shown in Section 3.4, SST changes can be due to SW radiation, precipitation, surface turbulent heat fluxes and entrainment cooling associated with wind speed, and oceanic upwelling and advection associated with wind stress.

While peak summer ISO forcing is the strongest on submonthly timescales (Figure 3.4), the peak ocean SST response occurs on MJO timescales (Figures 3.6e-h). As discussed in Section 3.4.3, this is likely because the time rate of change of SST is proportional to the forcing strength. Then, the total SST change due to an event is the integral of the forcing over time. The longer forcing period of MJO events causes a larger ocean response than the shorter, but stronger, submonthly forcing.

To evaluate the relative importance of the different processes on SSTs, we choose three representative regions with strong convection, wind, and SST variability (Figures 3.4 and 3.6). Regions 1, 2, and 3 are located in the AS, the BOB, and the eastern IO warm pool, respectively (Figure 3.6). Of the three, maximum summer ISO-induced SST variability is found in the warm pool (Figure 3.7), where maximum warming (cooling) is 0.83°C (1.09°C). The BOB also experiences strong ISO-induced SST changes, with maximum warming (cooling) of 0.78°C (1.08°C) and an STD of 0.25°C. ISO-induced SST variability is the smallest in the AS, where the mixed layer is thicker than in the BOB and equatorial warm pool (Figures 3.15a,b). Maximum warming (cooling) there is 0.67°C (0.73°C). These SST changes may have important implications in convection because the mean summer SSTs in all three regions exceed 28-29°C (Figure 3.5).

In general, winds have much larger effects than either SW radiation or precipitation on SST variability in the three regions of interest (Figures 3.10a,c for region 2). Surface turbulent heat fluxes and entrainment cooling associated with changes in wind speed appear to have a larger effect on MJO-scale SSTs in the BOB than oceanic upwelling and advection induced by changes in wind stress (Figures 3.10b,d). In the AS, the former are just slightly stronger than the latter (Figures 3.11a,b). The same relationships hold for submonthly ISOs, albeit to a lesser extent. The effects of wind stress and wind speed appear to be comparable in the warm pool region (Figures 3.11c,d).

For a more detailed analysis, many strong events (SST changes larger than 1 STD) are identified and analyzed using a time series of MJO and submonthly-scale SST changes from January 2000 - January 2004 (Figure 3.8). Of these, one MJO-scale event, an MJO composite, and one submonthly-scale event are discussed in Section 3.4.5. While the composite event is valuable for demonstrating the general MJO-scale variability, it can average out the larger amplitude changes that are visible when looking at specific MJO events (Figures 3.12 and 3.16). HYCOM appears to model SST variability in the three regions well, although it consistently underestimates the magnitude of SST changes in the BOB and AS. This is likely because the model's mixed layer is thicker than both the Levitus and the Argo observations (Figures 3.15a,b,e,f).

Consistent with our general results, surface turbulent heat fluxes and entrainment cooling

induced by changes in wind speed and oceanic upwelling and advection induced by changes in wind stress are the most important in determining SST variability during both events (Figure 3.13 for the MJO event). Again, on the MJO timescale, turbulent heat fluxes and entrainment cooling tend to dominate in the BOB, with some contributions from upwelling and advection (Figures 3.13a-b versus e-f and g-h). Turbulent heat flux effects appear to be larger than the effects of entrainment there, as indicated by very strong heat fluxes that coincide with comparatively small changes in hm (Figure 3.14 for the MJO-scale event). This apparent importance of turbulent heat flux in the BOB can be attributed to a modeled and observed thin mixed layer and a barrier layer there (Figure 3.15). The thin mixed layer is a result of strong stratification that in turn reduces entrainment cooling. In addition, the barrier layer inhibits surface cooling due to entrainment, leaving turbulent heat fluxes as the dominant process controlling summertime SST variability in the region. Also consistent with the general results, entrainment and turbulent heat fluxes, together with upwelling, are important in causing SST variability in the AS during the two events. SW radiation appears to play a non-negligible role in SST variability, particularly in the BOB during the MJO-scale event (Figures 3.13i,j).

The SST structure and temporal evolution varies between the MJO and submonthly events. As in the general results, SST changes are stronger during the MJO event than they are during the submonthly event. The strongest submonthly SST variability is in the mini-warm pool of the eastern AS, south of India, and in the western BOB (Figure 3.17), while it stretches across the AS and BOB during the MJO event (Figure 3.12). Winds consistently enhance the prevailing summer monsoon southwesterlies in the AS and BOB during peak cooling, while they oppose it during the warming phase of the events.

Overall, the effects of winds dominate IO SST variability during boreal summer ISOs, with some minor contributions from SW radiation and precipitation near the equator and in the BOB (Figures 3.10 and 3.11). Our work suggests that, in addition to surface heat fluxes, oceanic processes (upwelling and entrainment) are important in determining intraseasonal SST variability in the IO during boreal summer, particularly in the AS and warm pool region. The deterministic role

of winds on SST anomalies (Figures 3.10, 3.11, and 3.13), and the lag between OLR and SST variability (Figure 3.12), may indicate that SST variations in the north IO during summer are important in modifying MJO convection, and that the MJO causes SST anomalies with its strong winds. It is hoped that this study will contribute to the understanding of coupled air-sea processes.

Chapter 4

Influence of Atmospheric Intraseasonal Oscillations on Seasonal and Interannual Variability in the Upper Indian Ocean

4.1 Abstract

An ocean general circulation model (the Hybrid Coordinate Ocean Model, HYCOM) is used to examine the rectification of atmospheric intraseasonal oscillations (ISOs) on lower-frequency seasonal to interannual sea surface temperature (SST), mixed layer thickness (hm) and upper ocean heat content in the Indian Ocean (IO). Existing studies have shown that ISOs rectify on low-frequency equatorial surface currents and on cross-equatorial transport, suggesting that they may also have important impacts on low-frequency upper ocean variability. To evaluate these impacts, a hierarchy of experiments is run with HYCOM that isolates the ocean response to atmospheric forcing by 10-90 day (atmospheric ISO) events. Other experiments isolate the ocean response to a range of intraseasonal forcing fields including shortwave radiation, precipitation, and winds.

Results indicate that rectification of ISOs onto seasonal and interannual upper ocean variability does occur, and that it is important in some regions. The regions displaying maximum rectification vary between SST, hm, and upper ocean heat content, and between seasonal and interannual timescales. Strong seasonal SST rectification occurs in the Arabian Sea and in the Bay of Bengal. Because SSTs in the Arabian Sea are already warm ($>28°C$), the ISO-forced seasonal cycle peak of 0.6°C in May can affect convection there. Intraseasonal wind speed and wind stress have a much larger impact on seasonal and interannual SST, hm, and upper ocean heat content than either intraseasonal shortwave radiation or precipitation. The relative importance of entrainment

and turbulent heat flux due to intraseasonal wind speed, and of upwelling and horizontal advection due to intraseasonal wind stress, varies with region. Atmospheric ISOs appear to have a larger impact on the Indian Ocean Dipole Mode Index during non-dipole years than during strong dipole years.

4.2 Introduction

4.2.1 Atmospheric Intraseasonal Oscillations in the Indian Ocean and their Impacts on Coupled Climate Modes

Extensive research over the past few decades has shown that atmospheric intraseasonal oscillations (ISOs) play an important role in causing oceanic variability on both intraseasonal and seasonal-to-interannual timescales in the Indian and Pacific Oceans. ISOs range in period from 10-90 days, with peaks from 10-30 days mostly due to the Quasi-Biweekly Mode (QBM) [Kiladis and Weickmann, 1997; Chatterjee and Goswami, 2004], and peaks from 30-90 days due to the Madden Julian Oscillation (MJO) [Madden and Julian, 1971, 1972, 1994]. Relationships between ISOs, the Indian summer monsoon, the Indian Ocean Dipole (IOD; Saji et al., 1999; Webster et al., 1999; Murtugudde et al., 2000; Yu and Rienecker, 2000), and the El Nino Southern Oscillation (ENSO) demonstrate that ISOs can have regional and global impacts on climate. Effective modeling of ISOs is difficult, particularly because their initiation and propagation mechanisms are not well understood, and improvements are needed to allow for more accurate weather and climate predictions [Slingo et al., 1996; Sperber et al., 2005]. It is important, then, to better understand the interactions between ISOs and the upper layers of the Indian Ocean (IO) so that improved parameterizations can be developed.

A number of studies have shown that the phases of the QBM and the MJO together determine the amplitude and phase of the wet and dry spells of the Indian summer monsoon, the Asian monsoon, and the Australian monsoon [Sikka and Gadgil, 1980; Yasunari, 1981; Krishnamurti and Subrahmanyam, 1982; Webster, 1983; Krishnamurti et al., 1988; Chen and Chen, 1993; Chatterjee

and Goswami, 2004]. The time scale of the QBM corresponds well with the timing of Indian summer monsoon active and break periods [Murakami and Frydrych, 1974], and strong relationships have been noted between intraseasonal atmospheric and SST variability [Krishnamurti et al., 1988; Harrison and Vecchi, 2001; Sengupta et al., 2001; Schiller and Godfrey, 2003; Duvel et al., 2004; Shaji et al., 2005; Han et al., 2007; Vialard et al., 2008; Duncan and Han, 2009].

Atmospheric ISOs, particularly the MJO, have been shown to have a strong impact on the IOD, which is an internal mode of interannual variability in the Indian Ocean that has widespread impacts on the climate of regions surrounding the IO. During a positive (negative) IOD event, SSTs are anomalously warm (cool) in the west (east), which leads to increased (decreased) precipitation in the west (east) IO. The zonal wind, convection, and wave structure associated with MJOs is the likely source of their impacts on IOD events [Saji et al., 1999; Webster et al., 1999; Murtugudde et al., 2000; Yu and Rienecker, 2000; Rao and Yamagata, 2004; Han et al., 2006b]. MJO events co-occur with the termination of IOD events dating from the 1960s which do not co-occur with El Nino events, and they can impact the formation and strength of IOD events as well [Rao and Yamagata, 2004; Han et al., 2006b; Rao et al., 2009].

Connections have also been observed between MJO-scale atmospheric variability and the onset, development, and termination of El Nino events [Luther et al., 1983; Lau and Chan, 1985, 1988; Kessler et al., 1995; Moore and Kleeman, 1999; Takayabu et al., 1999; Kessler and Kleeman, 2000; Zavala-Garay et al., 2005]. Studies of 40-50 day variability in observed OLR revealed that the 1982-1983 El Nino event was preceded by MJO events that may have triggered and then amplified the development of the El Nino event [Lau and Chan, 1985, 1988]. A coupled ocean-atmosphere model of ENSO indicated that MJO triggering and development of El Nino events may be due to MJO-induced westerly and easterly wind bursts in the tropical west Pacific Ocean [Moore and Kleeman, 1999]. The modeled strength of the 1997-1998 El Nino event was improved by including MJO-forced rectified low-frequency SST in the forcing fields of an ocean general circulation model (OGCM). Without the rectified SST pattern, the modeled El Nino was much weaker than the actual event, indicating that MJOs can also impact the relative amplitude of the ENSO [Kessler

and Kleeman, 2000].

This extensive and ongoing effort to evaluate the interactions between atmospheric ISOs and the Indian, Asian, and Australian monsoons, the IOD, and ENSO has demonstrated that cross-timescale rectification occurs between atmospheric intraseasonal forcings and the ocean response, and that the impacts of this rectification can be important. It is likely that atmospheric ISOs can rectify onto the seasonal to interannual variability of the ocean outside of these well-studied modes of variability during years without strong IOD and ENSO events.

4.2.2 Rectification of ISOs on the Mean, Seasonal Cycle, and Interannual Variability in the IO

Some work has been done to investigate the rectification of atmospheric ISOs onto the seasonal-to-interannual variability of the upper ocean, but this work is very limited in the IO. Observational and OGCM studies have shown that atmospheric ISOs can rectify onto low-frequency SST, mixed layer thickness (hm), zonal surface currents and transport in the equatorial IO and tropical Pacific Ocean, and onto meridional heat transport in the tropical IO [Kessler and Kleeman, 2000; Waliser et al., 2003, 2004; Han et al., 2004; Halkides et al., 2007]. In a modeling study forced by atmospheric ISOs from 1988-2001, Han et al. [2004] found that ISO rectification onto low-frequency zonal equatorial transport and equatorial surface currents is mostly due to nonlinear processes that include entrainment and momentum upwelling, and the mixed layer depth's asymmetric response to easterly and westerly winds. In addition, the authors found that ISOs reduce the strength of seasonal eastward Wyrtki Jets (westward surface currents) by $\sim$15-25cm/s in boreal spring and autumn (January - March). Wyrtki Jets are an important source of zonal heat transport in the IO, and changes in their strength can be important in the region. A similar modeling study found that ISO rectified seasonal and interannual meridional heat transport can be significant (up to 30% of interannual heat transport is due to ISOs), and that it is mostly forced by wind processes which include turbulent heat fluxes, entrainment, and momentum upwelling [Halkides et al., 2007].

The impacts of atmospheric ISOs on seasonal-to-interannual SST, hm, and upper ocean heat

content in the IO have not been extensively evaluated. In a series of papers, Waliser et al. [2003, 2004] separately investigated the ocean's response to boreal summer and winter MJOs using composite MJO events to force an OGCM. Attention was paid to MJO rectification onto SSTs, hm, and zonal currents and transport for the intraseasonal event mean. Results indicated that MJOs do rectify onto the mean ocean hm, SST, zonal current, and zonal heat transport in the Indian and Pacific Oceans. During boreal winter, MJOs cause cooling of $\sim$0.15°C and hm shoaling of $\sim$4m in the IO, which was largely attributed to shortwave (SW) radiation and wind anomalies. The authors noted that strong SW radiation forcing co-occurs with weak wind anomalies, so the two forcings act together to shoal (thicken) the hm and increase warming (cooling) during suppressed (active) phases of the MJO. In addition, MJO-forced upwelling and vertical temperature gradients contributed to the modeled low-frequency SST and hm rectification. The authors found that boreal winter MJOs also contributed to a zonal SST gradient in the IO that occurs during the same time as typical IOD growth and is mostly due to surface heat fluxes. As a result, they hypothesized that surface heat fluxes associated with boreal winter MJOs may contribute to the formation and growth of IOD events [Waliser et al., 2003]. Different from boreal winter, the authors found that boreal summer MJOs can cause warming of $\sim$0.2°C and hm shoaling of $\sim$7m in the north IO, and an eastward rectified zonal equatorial current. The rectified SSTs forced by boreal summer MJOs were due mostly to SW radiation, while the rectified hm was due to nonlinear mixed layer processes, and the rectified current was most strongly due to wind stress forcing. In agreement with Han et al. [2004], the rectified current was related to the mixed layer's asymmetric response to easterly and westerly winds [Waliser et al., 2004].

4.2.3 Present Research

To date, there have not yet been studies using realistic (non-composite) atmospheric ISO forcing to systematically evaluate the rectification of atmospheric ISOs onto the mean, seasonal cycle, and interannual variability of SST, hm, and upper ocean heat content in the IO. The present work will tackle this problem by performing a series of OGCM experiments forced by observed

atmospheric fields from 2000-2008. We will evaluate the presence and strength of these impacts, and the processes by which they occur. Because both the MJO and QBM are important ISOs in the IO, we will examine the ISOs as a whole without separately assessing them.

4.3 Model and Experiments

4.3.1 The Hybrid Coordinate Ocean Model (HYCOM)

HYCOM is an oceanic general circulation model that uses pressure, density, and sigma vertical coordinates to optimize the model's representation of oceanic processes in a variety of conditions [Bleck, 2002; Halliwell, 2004]. It has been used in modeling studies of a wide range of regions and ocean basins including the Black Sea, the tropical Pacific Ocean, the Gulf of Mexico, the tropical Atlantic Ocean, and the Indian Ocean [Han, 2005; Kara et al., 2005a,b; Shaji et al., 2005; Han et al., 2006a; Prasad and Hogan, 2007; Han et al., 2008].

Here, HYCOM is configured to the IO basin from 30°S-25°N and 30°E-119°E with horizontal grid spacing of 0.5°$\times$ 0.5° and 18 vertical layers. The K-Profile Parameterization [Large et al., 1994, 1997; Large and Gent, 1999] is chosen as the vertical mixing scheme and no slip conditions are applied along continental boundaries. Because this research is focused on the upper ocean response to atmospheric variability, the vertical layers are more closely spaced in the upper ocean than they are in the deep ocean. The Persian Gulf and Red Sea are masked out of the model domain. The effects of the Indonesian Throughflow (ITF) and Bay of Bengal (BOB) rivers are considered by relaxing the temperature and salinity fields in the corresponding regions to Levitus and Boyer [1994] and to Levitus et al. [1994] climatology. A sponge layer from 25°S-30°S is applied to relax the model solutions to Levitus climatology near the model's southern boundary.

4.3.2 Forcing Fields

The 3-day mean QuickSCAT 10m winds [Tang and Liu, 1996], National Center for Environmental Prediction (NCEP) surface air temperature and specific humidity, shortwave and longwave

fluxes from International Satellite Cloud Climatology Project Flux Data (ISCCP-FD; [Zhang et al., 2004]), and Climate Prediction Center (CPC) Merged Analysis of Precipitation (CMAP) pentad precipitation [Xie and Arkin, 1996] are used to force HYCOM from 2000-2008. The CMAP pentad precipitation is interpolated to a 3 day interval to match other forcing fields. Note that ISCCP fluxes are available from 2000-2006. They are extended to 2008 by regressing NOAA OLR data onto ISCCP fluxes, as in Duncan and Han [2009]. In addition, the flux data is tuned by -25Wm^{-2} to improve the HYCOM SST simulation (see Section 4.4.1). This tuning is based on the fact that the mean of the ISCCP fluxes is approximately 25Wm^{-2} higher than that of in situ Triangle Trans-Ocean Buoy Network (TRITON) observations (Figure 4.1a red dashed line and blue dotted line; see also Duncan and Han [2009]). QuickSCAT wind stress is calculated from the 10m QuickSCAT wind speed and direction data using the standard bulk formula $\vec{\tau} = \rho_a C_D \left|\vec{V}\right| \vec{V}$, where ρ_a is the density of air (1.175 kgm^{-3}), C_D is a drag coefficient (0.0013), and $\left|\vec{V}\right|$ is the wind vector. Surface latent and sensible heat fluxes are calculated using the forcing wind, air temperature, and specific humidity data described above, together with HYCOM SST output, in the flux parameterizations of Kara et al. [2000].

4.3.3 Experiments

First, HYCOM is spun up for 30 years using monthly mean climatologies calculated from the forcing fields described above. Then, a series of model experiments is performed from 1 January 2000 - 31 December 2008 (Table 4.1). The first experiment, a 'main' run (MR) contains the complete 3-day model forcing fields. In experiment 1 (EXP1), all of the forcing fields are low-pass filtered to 105 days using a Lanczos filter [Duchon, 1979]. Low-pass filtering removes variability shorter than a chosen period, so EXP1 is forced by seasonal and longer timescale atmospheric variability that excludes the ISOs. Because the forcing fields are at a 3-day interval, synoptic-scale variability with periods of few days cannot be properly resolved. Therefore, the difference solution MR-EXP1 (Table 4.2) primarily isolates the ocean's response to atmospheric ISOs.

All of the atmospheric forcing fields are left unfiltered for Experiment 2 (EXP3) with the

Figure 4.1: a) Time series of TRITON (blue dotted line) and ISCCP tuned (black solid line) and untuned (red dashed line) net SW radiation from 21 October 2001 - 4 June 2004 at 90°E, 1.5°S. Horizontal lines show the mean SW radiation from each time series. Because albedo effects are not originally included in the TRITON data, Earth's surface albedo of 3% is applied to it. The tuned ISCCP data is reduced by 25 Wm^{-2}. Standard deviations (STD) and mean values of both ISCCP and TRITON SW radiation are displayed, along with the correlation coefficient (r) between the two. Units are Wm^{-2}. b) Time series of sea surface temperature (SST) from HYCOM Tuned MR (black solid curve), HYCOM untuned MR (blue dashed curve), and TRMMv4 0.25°×0.25° (red dotted curve) data, averaged over the whole IO, from 2000 - 2008. Horizontal lines show the mean SST from each time series. The correlation coefficient (r) between HYCOM MR and TRMM SSTs is displayed. Units are °C.

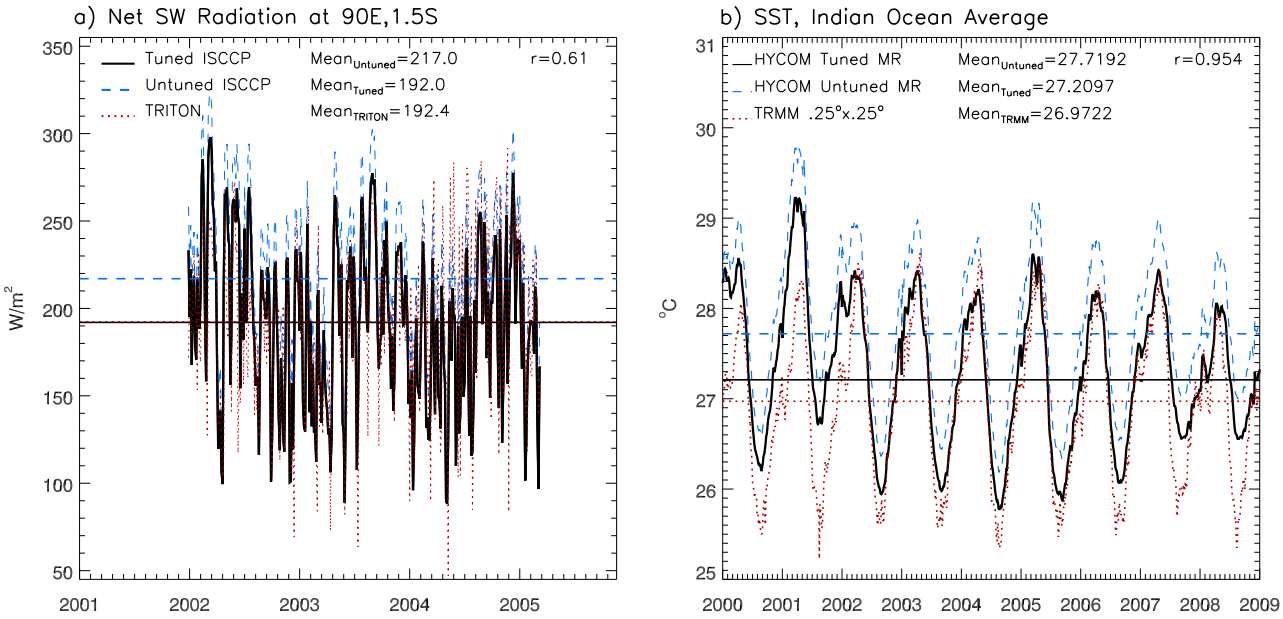

Table 4.1: Hybrid Coordinate Ocean Model experiments and forcings used[a]

Experiment Number	Forcings Used
MR	All 3-day mean forcing fields: winds, fluxes, precipitation
EXP1	Low-passed (removed less than) 105 days
EXP3	Low-passed wind stress
EXP4	Low-passed wind stress and speed
EXP5	Low-passed shortwave flux
EXP6	Low-passed precipitation

[a]Low-pass frequency is 105 days, unless otherwise noted.

Table 4.2: Hybrid Coordinate Ocean Model difference solutions and processes isolated

Difference Solution	Isolates Ocean Response To
MR-EXP1	All intraseasonal forcing fields: winds, fluxes, precipitation
MR-EXP3	Intraseasonal wind stress
MR-EXP4	Intraseasonal wind stress and speed
EXP3-EXP4	Intraseasonal wind speed
MR-EXP5	Intraseasonal shortwave flux
MR-EXP6	Intraseasonal precipitation

exception of QuickSCAT wind stress, which is low-pass filtered to 105 days. Similarly, only QuickSCAT wind speed and stress are low-pass filtered to 105 days in Experiment 3 (EXP4). The difference solution MR-EXP3 isolates the ocean's response to intraseasonal wind stress forcing. In HYCOM, wind stress can impact the ocean via Ekman convergence and divergence and horizontal advection. It can also impact mixing because it causes vertical shear in the modeled ocean currents and thus may affect the gradient and bulk Richardson numbers and cause shear instabilities. Difference solutions MR-EXP4 and EXP3-EXP4 isolate the ocean's response to intraseasonal wind in general (wind speed and stress) and wind speed only, respectively. HYCOM offers the choice to allow entrainment to be calculated through either wind speed or wind stress. We choose the 'wind speed' option, and thus wind speed can impact the upper ocean SST via turbulent heat fluxes (THF) and entrainment cooling. Experiments 4 and 5 (EXP5 and EXP6) are forced with low-pass 105 day filtered SW radiation and precipitation, respectively. The difference solutions MR-EXP5 and MR-EXP6 isolate the ocean's response to intraseasonal SW radiation and precipitation.

Note that this approach assumes that the ocean's responses to different forcing fields do not interact. In reality, they may interact due to nonlinearities in the system, thus the sum of oceanic responses to individual forcing fields may not exactly match the response to the total forcing fields. These nonlinear effects are generally small except in some specific regions of the IO, where their effects can be significant [e.g. Han et al., 2007; Duncan and Han, 2009, see also Section 4.4]. That is, this approach of separating the forcing fields (and thus the associated processes) is generally valid. Note also that the low-pass filtered wind stress and wind speed include the seasonal-to-interannual components directly rectified by the intraseasonal variability of winds associated with ISOs [Shinoda and Hendon, 2002]. Consequently, this paper focuses on assessing the rectified effects due to the nonlinear response of the upper IO to ISO forcing. Turbulent heat fluxes may contain a rectified component, because the bulk formulae used in their calculation are associated with the products of wind speed, air temperature, SST, specific humidity, and the wind-speed dependent coefficient of Kara et al. [2000].

4.4 Results

4.4.1 Model-Data SST Comparison

Averaged over the entire IO, SST variability from HYCOM MR agrees with that from the Tropical Rainfall Measuring Mission v4 (TRMM) data from 2002-2008 (Figure 4.1b), with a correlation coefficient of 0.95 between the two datasets. The discrepancy between HYCOM MR SST and TRMM SST in 2000 and 2001 is primarily due to the model's adjustment from the monthly spin-up forcing to the 3-day mean forcing fields used in the experiments. Consequently, only the years 2002-2008 are analyzed. Without flux tuning, the entire-IO mean of HYCOM SST is $\sim$0.75°C warmer than that of TRMM SST (Figure 4.1b, blue dashed and red dotted horizontal lines). Reducing ISCCP flux by 25Wm^{-2} (Section 4.3.2; Figure 4.1a) improves the simulated HYCOM SST (Figure 4.1b, black solid and red dotted curves), and the basin mean warm bias decreases to 0.24°C (Figure 4.1b, black solid horizontal line). As a result, all HYCOM experiments listed in Table 4.1 use ISCCP-FD data that has been corrected by -25Wm^{-2}.

Monthly climatologies of HYCOM MR and TRMM SSTs, averaged over boreal summer (JJA) and winter (DJF) monsoon months from 2002-2008, show that the spatial pattern of the modeled mean SST seasonal cycle is also consistent with observations (Figure 4.2). However, the modeled SSTs are warmer than the observed SSTs in most regions of the IO, except in the Thermocline Ridge region where the modeled SST is colder than observed. These high modeled SSTs produce the warm basin-mean bias in Figure 4.1b. One possible reason for the model/data discrepancy is that HYCOM's climatological mixed layer is thicker than the mixed layer estimated from World Ocean Atlas data [Boyer et al., 2009] in most regions, but thinner in the Thermocline Ridge region [Figure 4.3; see also Han et al., 2007; Duncan and Han, 2009]. When the modeled hm is thicker, the monsoon winds cannot cool the upper ocean as quickly as observed (Figures 4.1b and 4.2). When hm is thinner, as in the Thermocline Ridge region, the upper ocean is cooled more quickly, and thus the modeled SST is lower than observed (Figure 4.2). In addition, TRMM SST represents skin temperature, whereas HYCOM SST represents the temperature of the near-surface

layer with a minimum depth of 3m. This difference may also contribute to the stronger cooling in TRMM data forced by monsoon winds.

To further quantify the model-data SST comparison, Figure 4.4 shows time series of the SST seasonal cycle and interannual variability from TRMM, HYCOM MR and EXP1, averaged over regions where ISO impacts are large. See Sections 4.4.3 and 4.4.4 for a detailed discussion of the calculation of the seasonal cycle and the selection of these regions. The amplitude of the observed seasonal cycles (Figure 4.4a,b, red dotted line) is somewhat larger than the modeled seasonal cycles (Figure 4.4a,b, solid black line), but the timing of the two seasonal cycles is consistent. Correlation coefficients between HYCOM MR and TRMM seasonal SSTs are 0.89 and 0.99 in the Arabian Sea and the southwest IO, respectively. Removing ISO forcing fields increases (decreases) the difference between the observed and modeled SST seasonal cycle in the Arabian Sea (southwest IO) during April and May (February and March) (Figure 4.4a,b blue dashed and red dotted curves). That is, ISOs appear to improve the modeled SSTs in the Arabian Sea, and they appear to worsen the modeled SSTs in the southwest IO. In reality, the modeled thermocline and hm are thin in the southwest IO, so the impact of ISOs on the region-averaged SST is exaggerated there (4.3). Similar time series of region-averaged HYCOM MR and TRMM SST interannual variability are shown in Figure 4.4c,d. Details about the calculation of interannual variability can be found in Section 4.4.5. The modeled (solid black line) and observed (dotted red line) SST interannual variability are fairly consistent in the west equatorial IO and the central IO (Figure 4.4c,d), although the amplitude of the observed interannual variability is often larger than, and sometimes out of phase with, the modeled variability. Correlation coefficients between HYCOM MR and TRMM SSTs are 0.53 and 0.49 in the west equatorial IO and the central IO, respectively.

4.4.2 ISO Impact on Time-Mean Upper Ocean Variables

Maps of the ISO-forced change in the mean SST, hm, upper ocean heat content, and mixed layer heat content, averaged from 2002-2008 (Figure 4.5) show that ISO impacts on the mean are regionally dependent. Heat content over a vertical layer is calculated using the standard formula

Figure 4.2: a) Summertime (June - August) mean SST from HYCOM MR, calculated from monthly mean climatologies. (b) Wintertime (December - February) mean SST from HYCOM MR, calculated from monthly mean climatologies. (c) Same as *a*, but from TRMMv4 2.5°×2.5° SST. (d) Same as *b*, but from TRMMv4 2.5°×2.5° SST. Units are °C.

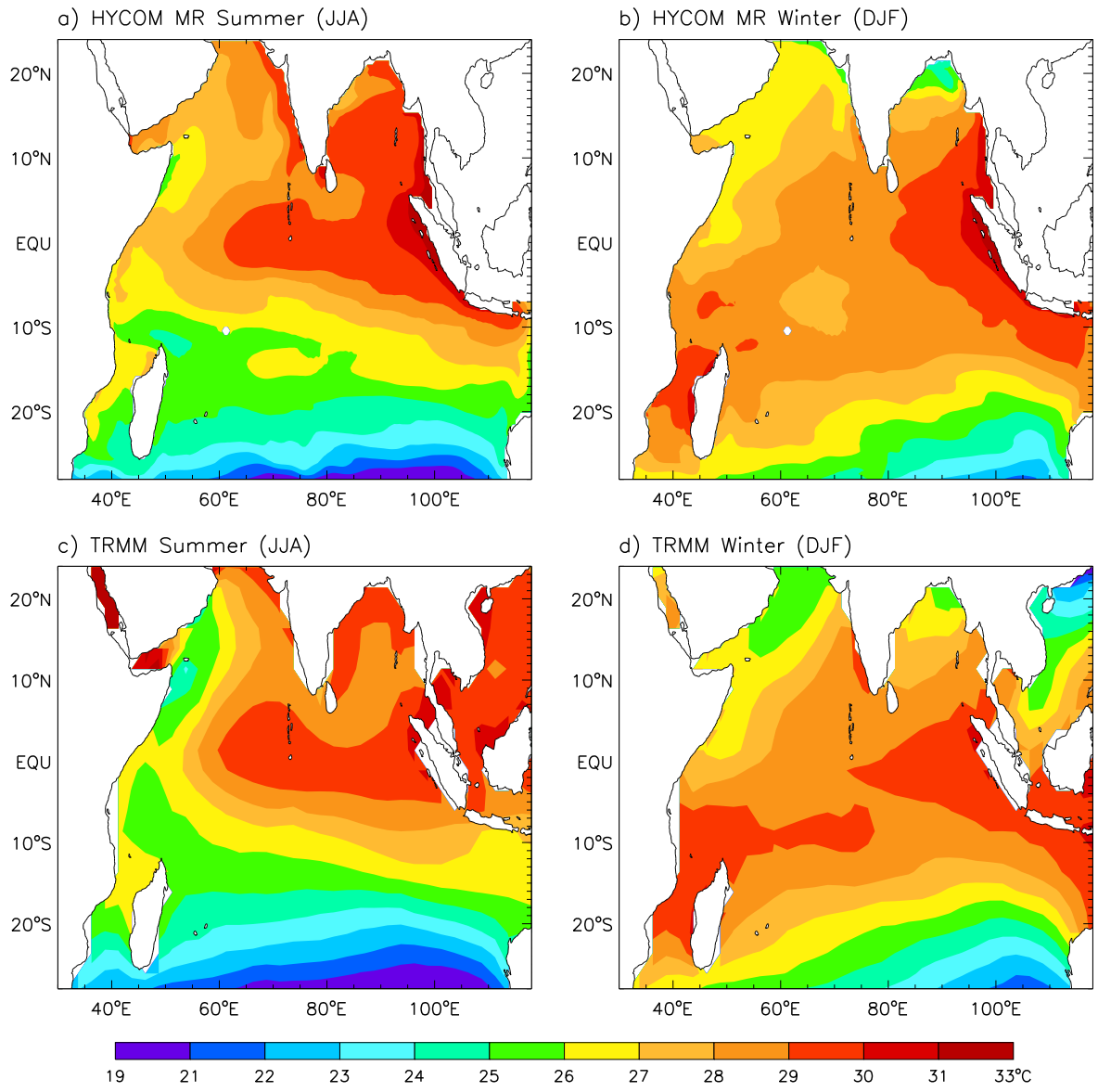

Figure 4.3: a) Mean hm from HYCOM MR, calculated from 3-day model output. (b) Mean hm, calculated from monthly mean Levitus WOA09 data.Units are m.

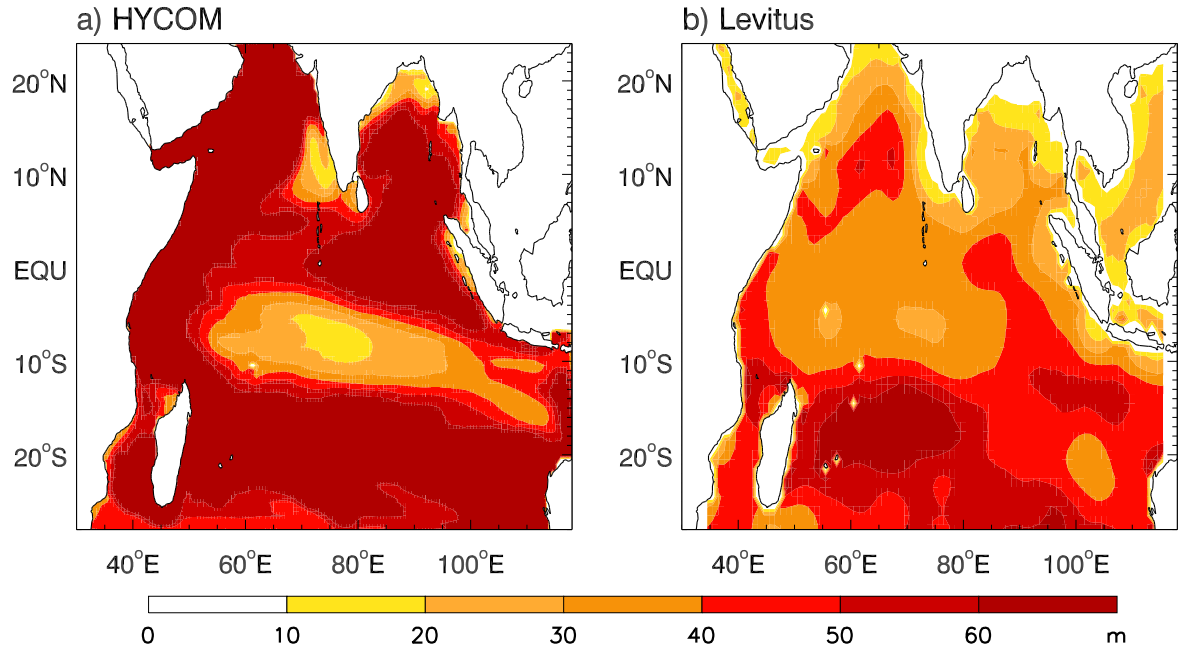

Figure 4.4: (a) Time series of seasonal SST from 2002-2008, averaged over the Arabian Sea (Region 1 in Figure 4.7c). The black solid, blue dashed, and red dotted curves represent the SST from HYCOM MR, HYCOM EXP1, and TRMMv4 2.5°×2.5° data. Horizontal lines represent the mean SSTs, which are also calculated and displayed. Differences between HYCOM MR and EXP1 represent the contributions of atmospheric intraseasonal oscillations (ISOs) to the seasonal SST. (b) Same as *a*, except averaged over the southwest IO (Region 3 in Figure 4.7c). (c) Same as *a*, except interannual SSTs averaged over the west equatorial IO (Region 1 in Figure 4.14). Because mean interannual SSTs are always zero, the horizontal black line represents zero. STDs of SSTs and correlation coefficients (ri) between HYCOM MR and TRMM SSTs are calculated and displayed. (d) Same as *c*, except averaged over the central IO (Region 2 in Figure 4.14). Units are °C.

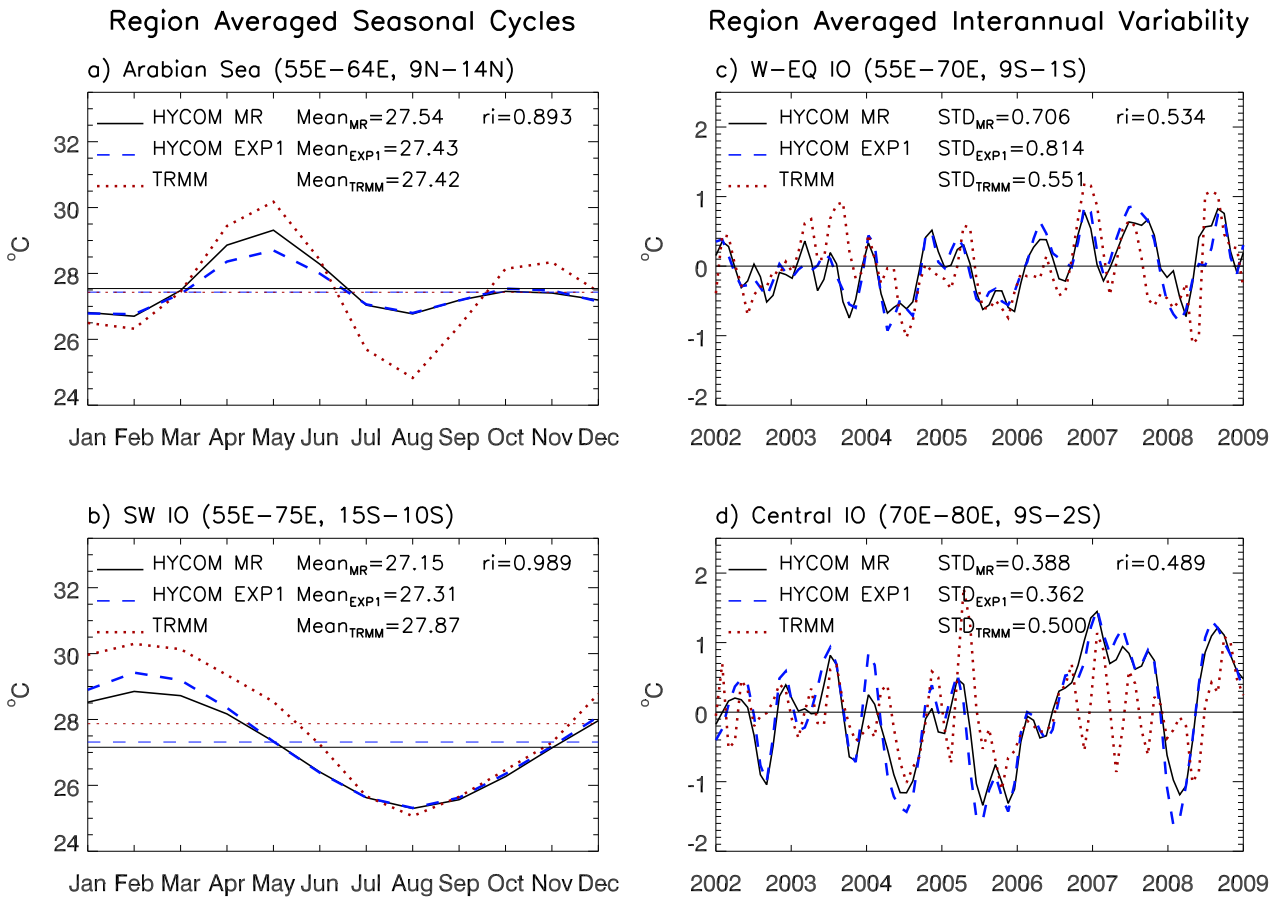

$H = \rho_z c_p T_z Z$, where ρ_z is the density of sea water in the layer, c_p is the specific heat of sea water ($4.0 \times 10^3 Jkg^{-1}C^{-1}$), T_z is the temperature of the layer, and Z is the layer thickness. For upper ocean heat content, Z is 200m, and T_z and ρ_z are weighted averages over the layer. For mixed layer heat content, Z is the mixed layer thickness, and T_z and ρ_z are the mixed layer temperature and density, respectively.

ISOs tend to reduce the mean SST in the equatorial and south IO, but they warm the mean SST in the Arabian Sea and the BOB by 0.1-0.2°C (Figure 4.5a). The strongest ISO impact on the mean SST occurs along the Sumatra coastline, where SSTs are reduced by 0.1-0.9°C, and along the western coastline of Madagascar, where SSTs are reduced by 0.1-0.5°C. In comparison with the seasonal cycle, which can have an amplitude of over 1°C (Figures 4.1b and 4.4), these values can be non-negligible in some specific areas. A wide stretch of weaker cooling (0.1-0.3°C) extends between the two regions.

The pattern of ISO impact on mean hm (Figure 4.5b) differs from that on mean SST (Figure 4.5a) in the interior IO. Along the coast of Sumatra and west of Java, however, the maximum ISO-forced mean hm is 3-12m, consistent with the cool SST there. This thicker hm, together with the cool SST, suggests that anomalous entrainment and upwelling cooling due to ISOs contributes to the pattern of mean cooling there. Different from SST, there is a region of ISO-forced shallow mean hm anomaly just to the west of the maximum, with hm shoaling by 3-13m. In the Arabian Sea, mean hm shoals by 3-10m (deepens by 3-12m) in the northwest (southeast). Patchy regions of thickened mean hm also stretch across the basin from approximately 15°S -25°S. In these regions, rectification of ISOs onto the mean surface heat fluxes and instabilities may play an important role in causing the mean SST change (see Section 4.4.4.1 for additional discussion of processes).

The most apparent impacts of atmospheric ISOs on the mean upper ocean (above 200m) heat content are that they increase the heat content in most regions in the north IO, including the BOB, by up to $3\times10^6 Jm^{-2}$ (Figure 4.5c). This is an intriguing result, which indicates that ISOs may pump heat into the upper IO through mixing north of the equator. This heat may be transported to the south IO by the shallow cross-equatorial meridional overturning circulation, where it is released to

Figure 4.5: Change in mean HYCOM (a) SST, (b) mixed layer thickness (hm), (c) upper ocean (200m) heat content, and (d) mixed layer heat content due to ISOs, calculated from mean values of HYCOM MR and EXP1. Calculations of heat content are detailed in Section 4.4.2. Units are °C for SST, m for hm, and $10^6 Jm^{-2}$ for heat content.

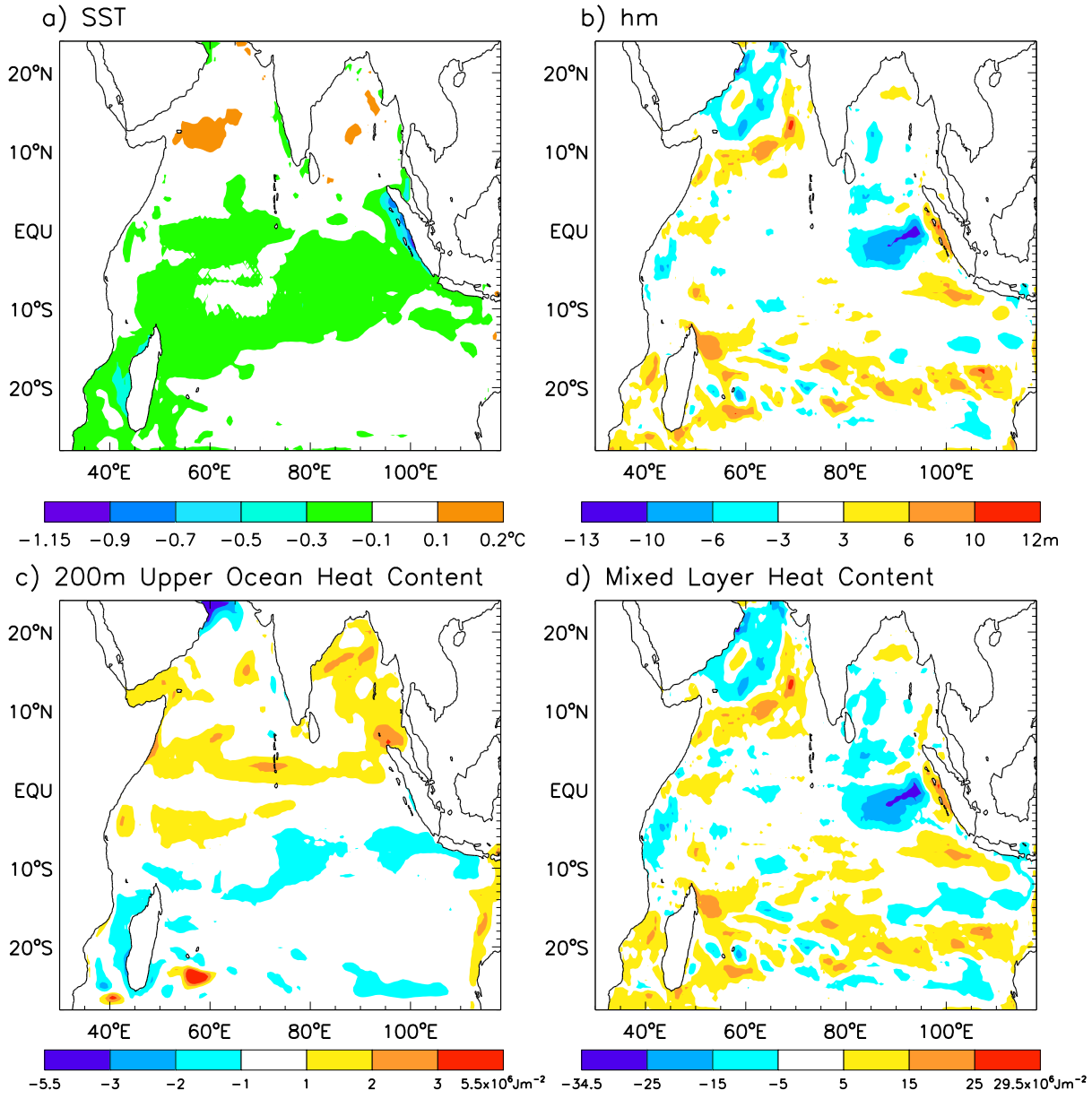

the atmosphere. These results are reminiscent of existing studies on the effects of tropical cyclones, which suggest that tropical cyclones can pump heat into the tropical ocean and affect meridional heat transport [Emanuel, 2001; Sriver and Huber, 2007].

The pattern of ISO-altered mean mixed layer heat content closely resembles that of hm (Figure 4.5b,d). In some regions like the Sumatra coast, the mean mixed layer heat content increases with the thickening mean hm, even though the mean SST cools there. This suggests that hm has a much larger impact in determining the mixed layer heat content than SST does. In general, when the ISO-forced SST is warming, the mixed layer is shoaling, indicating reduced entrainment. A thinner mixed layer tends to override the impact of warming SST, resulting in decreased mixed layer heat content.

4.4.3 ISO Rectification on Seasonal to Interannual Variability

Atmospheric ISOs can impact both the mean state and the variability of the upper IO. In order to evaluate the effects of atmospheric ISOs on seasonal-to-interannual ocean variability, we first calculate the monthly averages of low-passed 105 day filtered SST and hm from the 3-day HYCOM difference solution MR-EXP1. Monthly averaging removes the intraseasonal ocean response while preserving the longer timescale seasonal-to-interannual response, and low-pass filtering the data to 105 days before the averaging ensures that the intraseasonal response is fully removed.

The standard deviation (STD) of this monthly averaged ISO-forced SST, hm, upper ocean heat content, and mixed layer heat content provide a basin-wide view of the seasonal-to-interannual IO response to atmospheric ISOs (Figure 4.6). Similar to the impacts of ISOs on the mean state, the strongest ISO rectification onto SST variability occurs in the south tropical IO, along the west coasts of Sumatra and Madagascar (0.2-0.6°C), and, to a lesser degree, in the Arabian Sea and the BOB (0.2-0.4°C; Figure 4.6a). ISO-forced upper ocean heat content variability occurs in most regions of the IO north of 15°S, and in a band near 23°S that stretches from the western boundary to 95°E with values ranging from 1-11$\times 10^6 \mathrm{Jm}^{-2}$ (Figure 4.6c). Rectified hm and mixed layer heat content variability have maxima extending south from the Arabian Sea to Madagascar (12-31m;

20-80$\times 10^6$Jm^{-2}), in the eastern equatorial basin (12-31m; 20-80$\times 10^6$Jm^{-2}) and in the subtropical south IO (15°S-25°S; 8-31m; 10-80$\times 10^6$Jm^{-2}) (Figure 4.6b,d).

As with the rectification onto the mean, rectification of ISOs onto the variability of hm dominates the mixed layer heat content (Figure 4.6b,d). Consequently, the remainder of this work will focus on the rectification of ISOs onto SST, hm, and upper ocean heat content. As shown above and shall be discussed below, atmospheric ISOs rectify onto the mean, seasonal and interannual variability of SST, hm, and upper ocean heat content in a number of climatically relevant regions in the IO. In order to further understand the impact of ISO rectification on the IO, the seasonal cycle and the interannual variability of the ISO-forced upper ocean response are evaluated separately. Here, the seasonal cycle is defined as the monthly mean climatology for the period of 2002-2008, and the interannual variability is the deviation from the seasonal cycle.

4.4.4 ISO Rectification on the Seasonal Cycle of the Upper Ocean

The seasonal cycle of HYCOM difference solution MR-EXP1 provides a measure of the presence and magnitude of atmospheric ISO rectification on seasonal timescales. Before calculating the monthly mean climatologies, all model output variables are low-pass filtered to 105 days to ensure that the intraseasonal ocean response is removed from the rectified signal. For example, the impact of atmospheric ISOs on the seasonal cycle of SST is calculated by low-pass filtering the SST from difference solution MR-EXP1 to 105 days, and then calculating the monthly mean climatology from 2002-2008. The same procedure is followed using the other model difference solutions detailed in Table 4.2 to determine the rectification of intraseasonal wind, SW radiation, and precipitation onto the seasonal cycle of the upper ocean. The STDs of ISO-forced seasonal variations in SST, hm, and upper ocean heat content all indicate that rectification is present across the IO (Figure 4.7). The magnitude of rectification onto seasonal variability is relatively large in some areas of the IO. Regions with strong rectification and relatively high model-data correlations are noted by boxes in Figure 4.7. Further analysis of ISO rectification onto seasonal variability focuses on these regions of maximum impact.

Figure 4.6: STD of ISO-forced seasonal + interannual HYCOM (a) SST, (b) hm, (c) upper ocean heat content, and (d) mixed layer heat content, calculated from monthly averaged difference solution (MR-EXP1). Units are °C for SST, m for hm, and $10^6 Jm^{-2}$ for heat content.

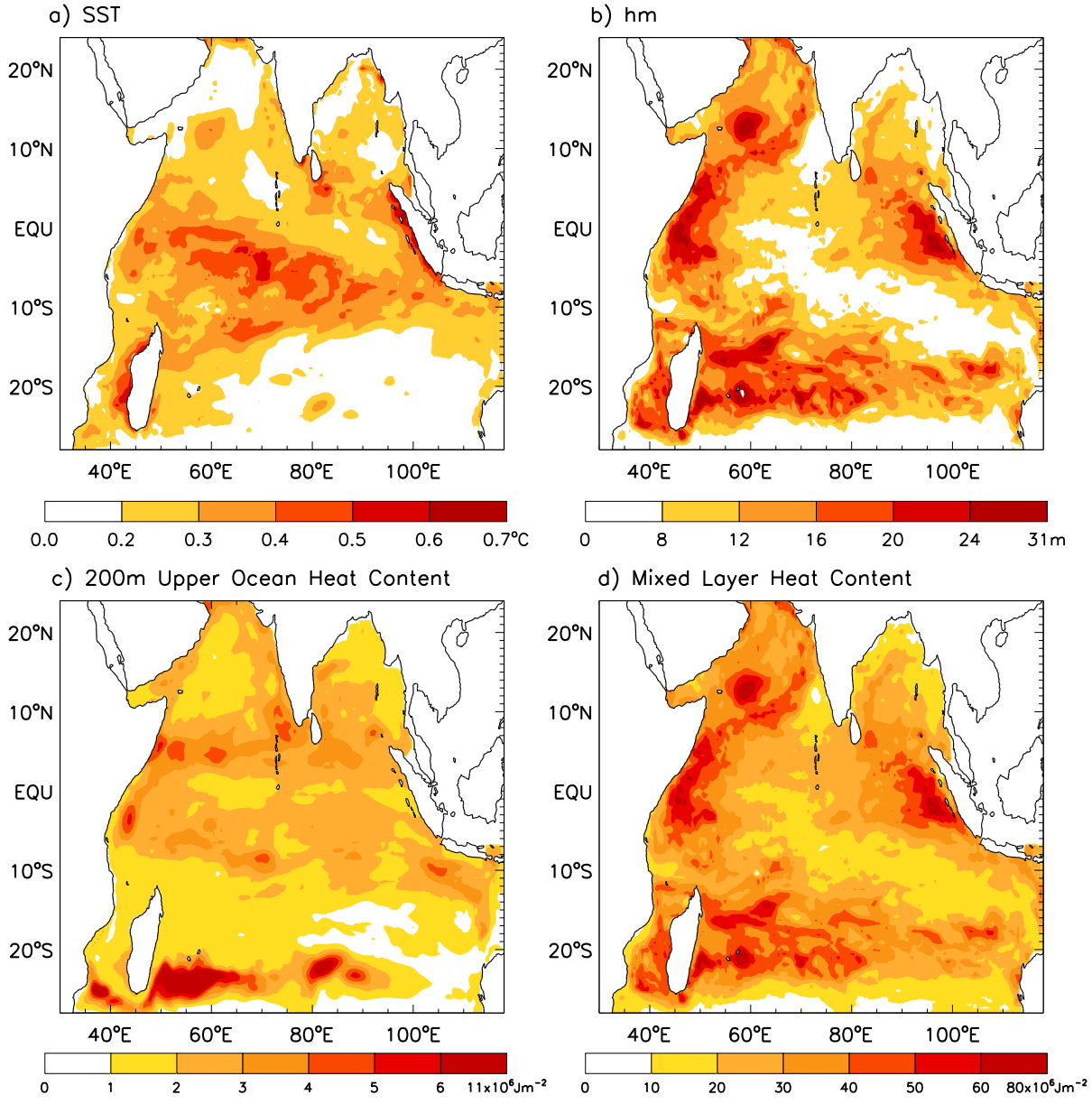

Figure 4.7: STD of ISO-forced seasonal HYCOM (a) hm, (b) upper ocean heat content, and (c) SST, calculated from difference solution (MR-EXP1). Representative regions with strong ISO-forced seasonal variability are boxed and numbered, and they are discussed in Section 4.4.4. Units are °C for SST, m for hm, and $10^6 Jm^{-2}$ for heat content.

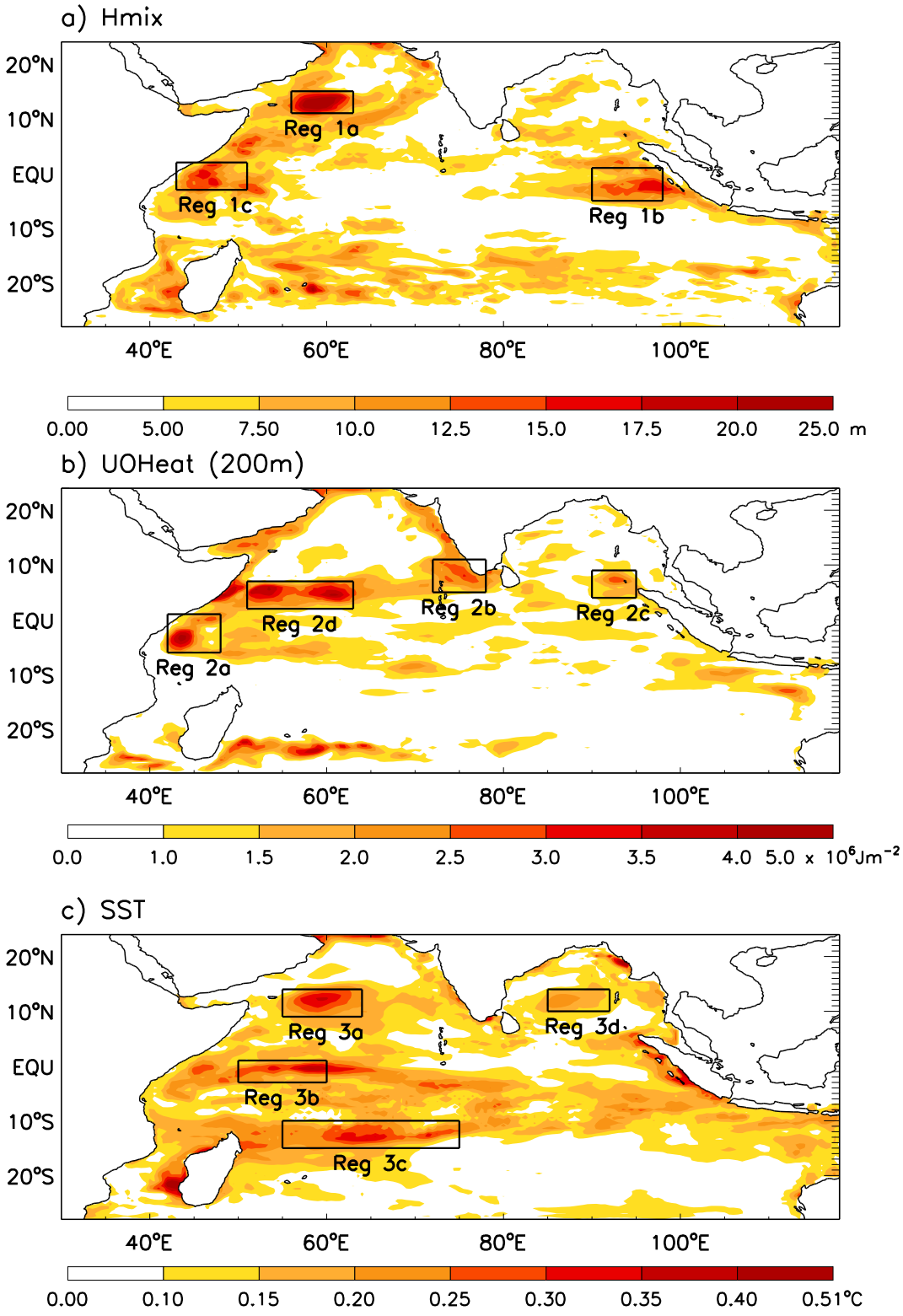

Time series of the ISO-induced seasonal variations of SST, hm, and upper ocean heat content are averaged over the corresponding regions of interest and shown and discussed in Sections 4.4.4.1-4.4.4.3. These time series provide an in-depth look at the timing and magnitude of the rectified seasonal cycle in each region. When the ISO-forced rectified signal exceeds one standard deviation, it indicates that there is consistently large rectification during the corresponding month for every year of the study. Region-averaged seasonal variations forced by intraseasonal wind (both stress and speed), SW radiation, and precipitation, and those forced separately by intraseasonal wind speed and wind stress, are shown and discussed in Sections 4.4.4.1-4.4.4.3 as well. These time series allow for a clear determination of the degree to which each intraseasonal forcing and its associated processes contribute to the rectified seasonal cycle in each region of interest.

4.4.4.1 ISO Rectification on Seasonal Hm

Three regions with maximum ISO-forced seasonal hm variability are located in the Arabian Sea (56°E-63°E, 11°N-15°N), the eastern equatorial IO (90°E-98°E, 5°S-1°N), and the western equatorial IO (43°E-51°E, 3°S-2°N) (Figure 4.7a). In general, intraseasonal wind has a much larger impact than intraseasonal SW radiation and precipitation on the seasonal cycle of hm in all three regions of interest (Figure 4.8a-c). Intraseasonal wind speed and wind stress contribute to the seasonal hm cycle in amounts that vary by region and timing (Figure 4.8d-f).

The Arabian Sea is a climatologically important region that is strongly impacted by the seasonally changing Indian summer monsoon winds. In the Arabian Sea, the ISO-forced hm seasonal cycle has minima in April and May (-30.44m and -28.36m respectively) and a maximum in October (16.69m), indicating that strong rectification occurs there during each of these months from 2002-2008 (Figure 4.8a). Intraseasonal wind speed, which affects hm by changing the entrainment rate, dominates the springtime minimum and contributes largely to the fall maximum (Figure 4.8d). This is because ISO winds tend to weaken the seasonal monsoon winds during spring when the southwest monsoon begins (Figure 4.9a-c), and thus reduce entrainment and shoal the mixed layer. During the monsoon transition period in October, however, mean climatological winds in

Figure 4.8: (a) Time series of seasonal hm averaged over the Arabian Sea (Region 1a in Figure 4.7a), forced by total ISOs (MR-EXP1, black curve), total wind (MR-EXP4, red curve), SW radiation (MR-EXP5, blue curve), and precipitation (MR-EXP6, green curve). (b) Same as *a*, but averaged over the east equatorial IO (Region 1b in Figure 4.7a). (c) Same as *a*, but averaged over the west equatorial IO (Region 1c in Figure 4.7a). (d) Same as *a*, but for seasonal SST forced by total wind (MR-EXP4, black curve), wind speed (EXP3-EXP4, red dotted curve), and wind stress (MR-EXP3, blue dashed curve). (e) Same as *d*, but averaged over the east equatorial IO. (f) Same as *d*, but averaged over the west equatorial IO. Horizontal lines represent the mean seasonal SSTs from each difference solution. STDs of hm changes due to each intraseasonal forcing are calculated and displayed in the figures, along with the correlation coefficients (r) between total wind hm changes and those due to wind speed and wind stress. Units are m.

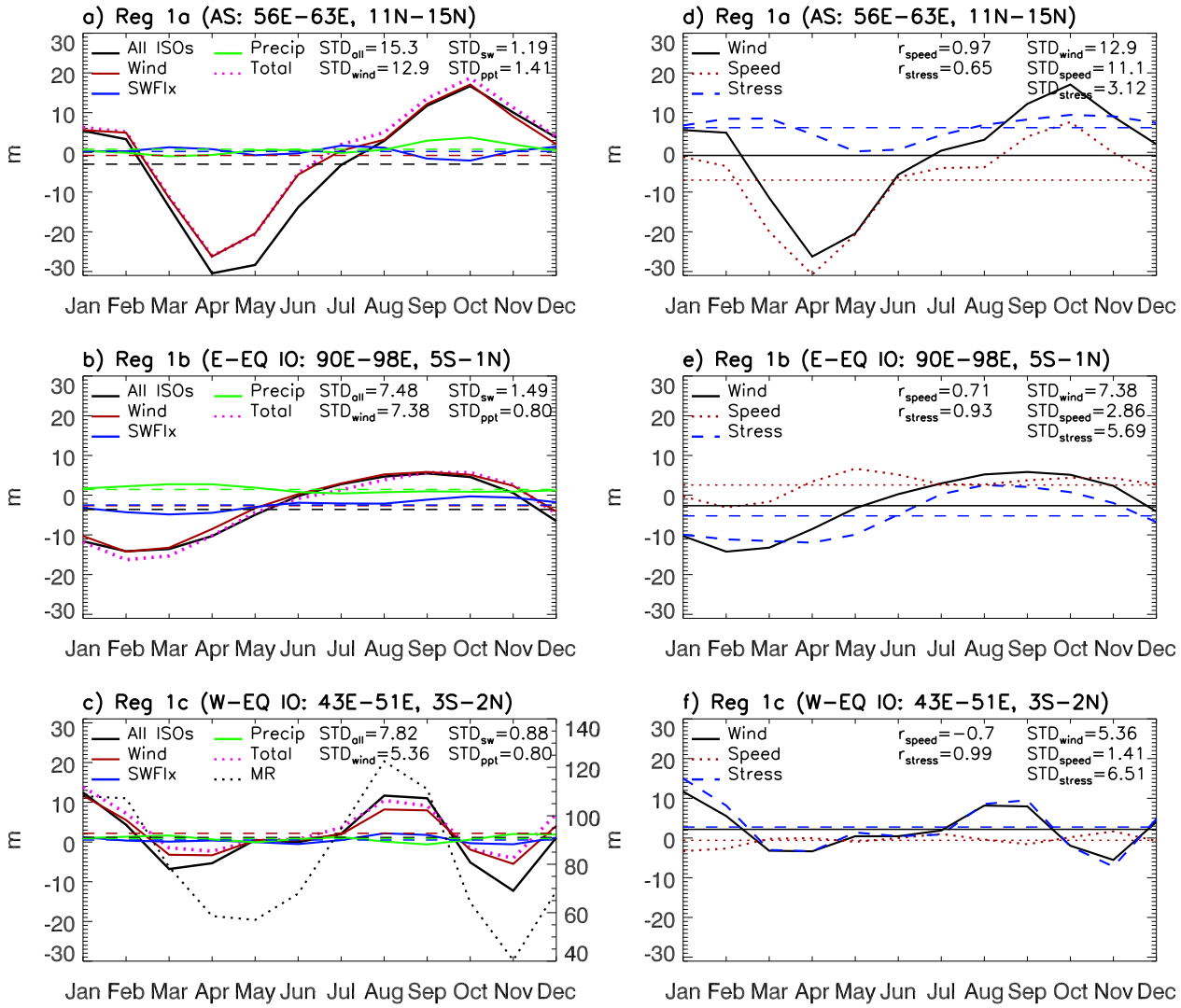

the Arabian Sea are weak (Figure 4.9d), and ISO winds strengthen the mean winds (Figure 4.9e,f), causing enhanced entrainment and a thickened mixed layer (Figure 4.8a). Intraseasonal wind stress, which can rectify onto seasonal hm through anomalous advection and entrainment, also has significant contributions to the deepened hm in October (Figure 4.8d). The effects of SW radiation and precipitation further shallow hm by 5-10m during spring (Figure 4.8a). It is important to note that the sum of the change in hm due to wind, SW radiation, and precipitation does not exactly equal the total rectified hm (Figure 4.8a-c, purple dotted and black solid lines), suggesting that the nonlinear response of the ocean to these forcing fields allows different effects to interact. For example, the ISO-associated precipitation can enhance stratification in the region. This enhanced stratification can interact with the weakened winds due to ISOs, thus substantially reducing the entrainment rate and further thinning the hm.

The ISO-induced hm seasonal variations in the east equatorial IO attain minima in February and March (-14.12m and -13.55m respectively) and a maximum in September (5.48m) (Figure 4.8b). Different from the Arabian Sea, intraseasonal wind stress plays a somewhat larger role in January and February, while intraseasonal wind speed and stress both contribute to the maximum rectified seasonal variations in late summer and fall (Figure 4.8e).

In the west equatorial IO, ISO rectification onto the hm seasonal cycle has a strong semi-annual component that is also seen in the full MR seasonal cycle of hm, which has two maxima and two minima (Figures 4.8c, solid and dotted black lines). The first maximum occurs in January (12.45m) during the winter monsoon, and the second occurs in August and September (11.67m and 11m, respectively) during the summer monsoon. The first minimum occurs in March (-6.8m), and the second occurs in November (-12.28m) during the monsoon transition seasons. Intraseasonal wind stress has a much larger impact on the seasonal hm variations than wind speed during all months with strong ISO rectification in the west equatorial IO (Figure 4.8f), likely because of changes in mixing associated with shear instabilities (see Section 4.3.3).

Figure 4.9: (a) QuickSCAT mean wind speed (shading) and stress (arrows) excluding ISOs, calculated for May (2002-2008) from data that has been low-pass filtered to 105 days. Details about the filter are in Section 4.3.3. (b) Same as *a* except data is unfiltered and includes ISOs. (c) Same as *a* except only ISO winds are shown. ISO winds are calculated as the difference between full (*b*) and low-passed (*a*) winds. (d) Same as *a* except averaged over October. (e) Same as *b* except averaged over October. (f) Same as *c* except averaged over October. Units are ms^{-1} for wind speed and dyn cm^{-2} for wind stress.

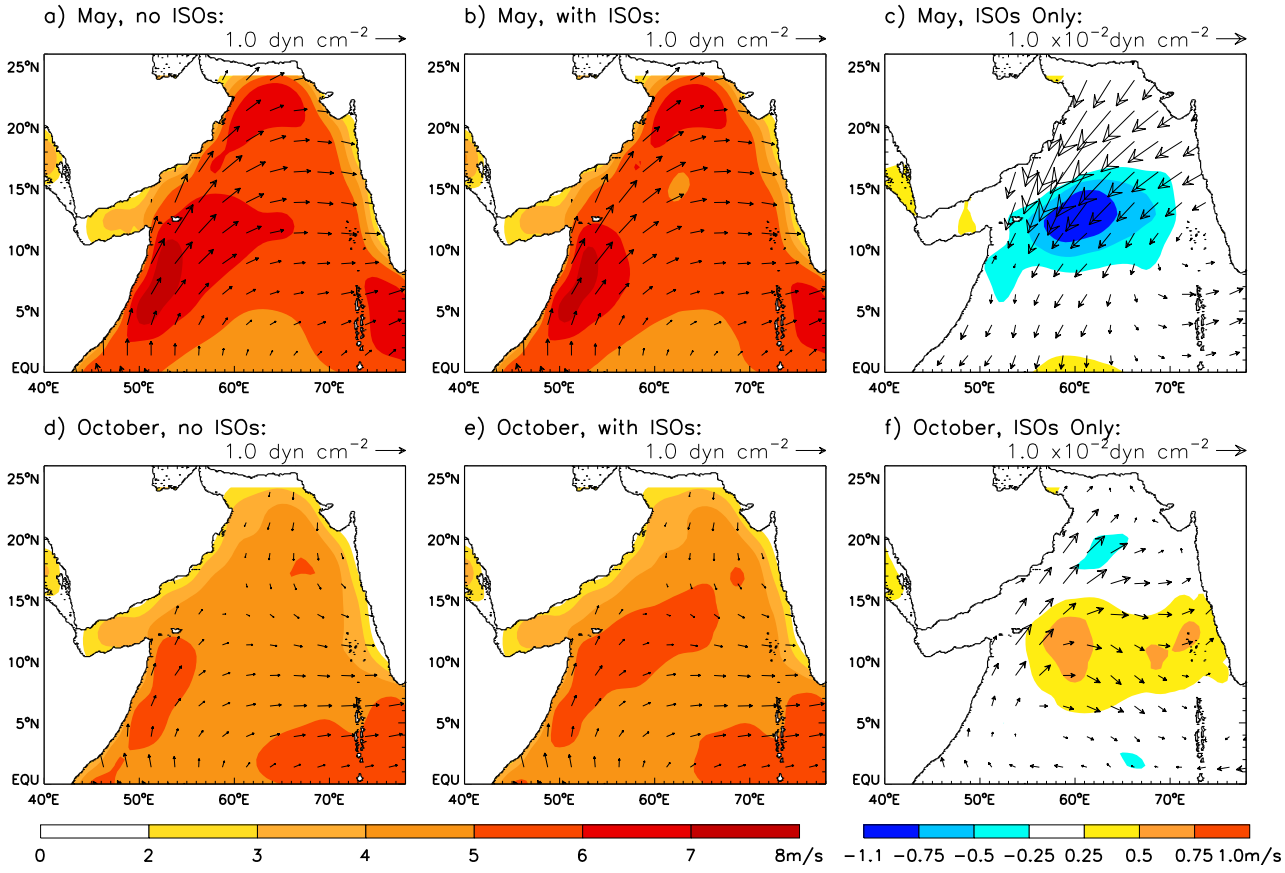

4.4.4.2 ISO Rectification on Seasonal Upper Ocean Heat Content

ISO rectification onto the seasonal cycle of upper ocean heat content occurs in various regions of the Indian Ocean. Here, we choose four representative regions where the impacts are large: the southwest equatorial IO (42°E-48°E, 6°S-1°N), the southeast Arabian Sea (72°E-78°E, 5°N-11°N), the southern BOB (90°E-95°E, 4°N-9°N), and the southwest Arabian Sea (51°E-63°E, 2°N-7°N) (Figure 4.7b). In all four regions, ISOs pump heat into the upper ocean, producing positive mean heat content in the upper 200m (Figure 4.10a-c, horizontal black dashed lines; see also Figure 4.5). There are, however, significant regionally-dependent seasonal variations. As with the impact of hurricanes on the basin [e.g. Emanuel, 2001; Sriver and Huber, 2007], atmospheric ISOs appear to act as a heat pump for the IO. This heat pump effect is dominated by winds associated with ISOs (Figure 4.10). Intraseasonal wind has a much larger impact on the seasonal cycle of upper ocean heat content than intraseasonal SW radiation and precipitation in all regions, especially in the BOB (Figure 4.10c). Intraseasonal SW radiation does contribute to the seasonal maximum in the southeast Arabian Sea during September (Figure 4.10b). In some regions during some seasons, such as in the western equatorial IO during January-March and in the southeastern Arabial Sea during July-October, the effects of SW radiation and precipitation are non-negligible. Intraseasonal wind stress consistently plays a more important role than wind speed on the seasonal cycle of upper ocean heat content in all regions (Figure 4.10 d-f; southwest Arabian Sea not shown). This might be because intraseasonal wind stress increases current shear in the upper ocean and thus enhances shear instabilities and increases mixing. A detailed investigation of the processes that cause the heat pump effects is beyond the scope of this study, though it is an essential component of our future research.

Where does the heat that ISOs pump into the north IO eventually go? ISOs cause negative mean upper ocean heat content in the southern IO (Figure 4.5), indicating that this north IO heat could be transported to the south by the cross-equatorial cell [e.g. Schott et al., 2009], where it is lost by the ocean to the atmosphere. Detailed examination of these processes, however, is beyond

Figure 4.10: (a) Same as Figure 4.8a, except for upper ocean heat content averaged over the southwest equatorial IO (Region 2a in Figure 4.7b). (b) Same as *a* except averaged over the southeast Arabian Sea (AS) (Region 2b in Figure 4.7b). (c) Same as *a* except averaged over the south Bay of Bengal (BOB) (Region 2c in Figure 4.7b). (d) Same as Figure 4.8d, except for upper ocean heat content averaged over the southwest equatorial IO. (e) Same as *d* except averaged over the southeast AS. (f) Same as *d* except averaged over the southern BOB. Units are $10^6 Jm^{-2}$

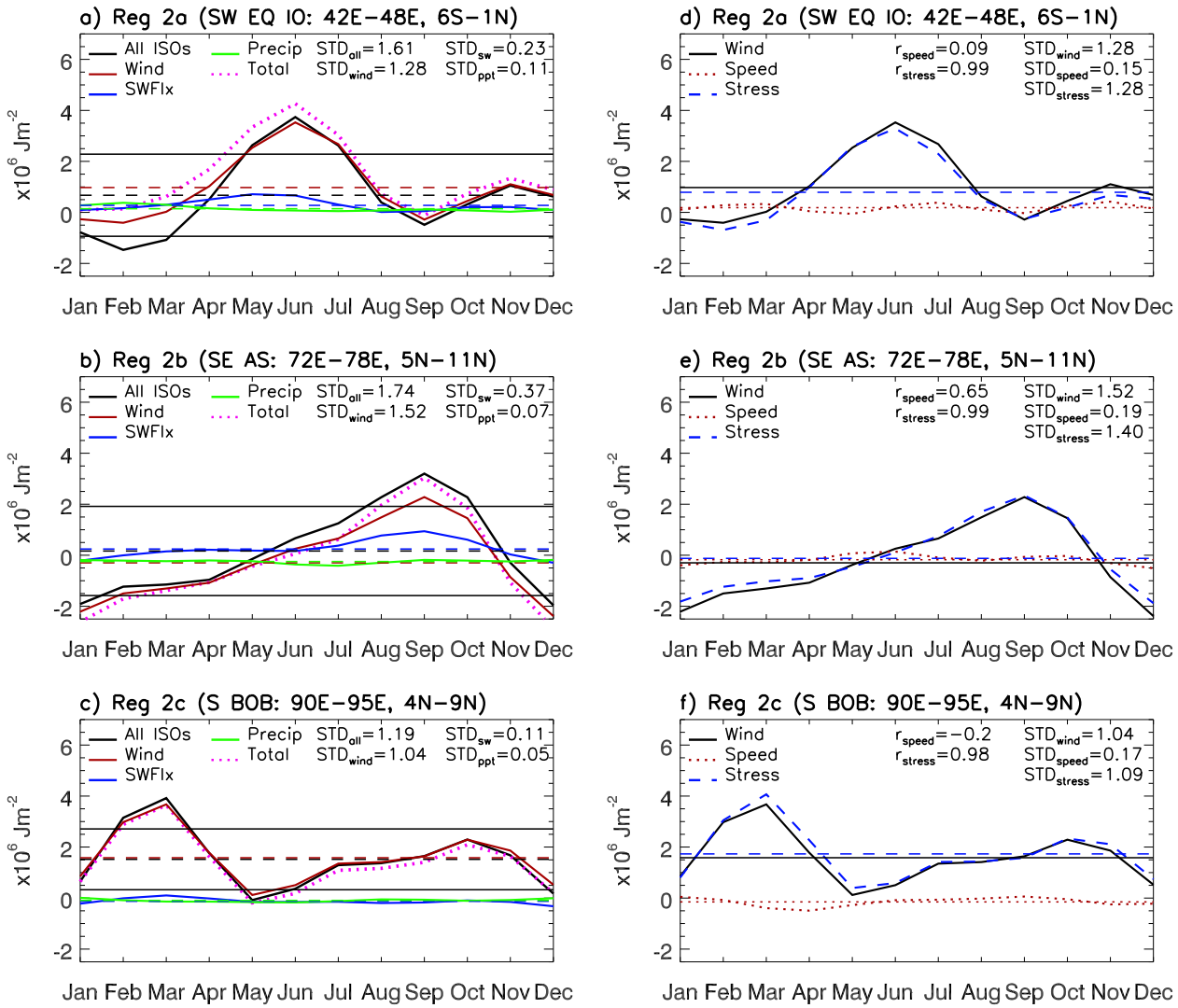

the scope of this research.

4.4.4.3 ISO Rectification on Seasonal SST

Atmospheric ISOs have a strong impact on the seasonal variability of SST in a range of climatically important regions of the IO (Fig. 4.7c), including the Arabian Sea (55°E-64°E, 9°N-14°N), the western equatorial IO (50°E-60°E, 3°S-1°N), the southwest IO (55°E-75°E, 15°S-10°S), and the BOB (85°E-92°E, 10°N-14°N). Intraseasonal wind consistently has a much larger impact on the total SST seasonal cycle than either intraseasonal SW radiation or precipitation in all four regions (Figure 4.11a-c; BOB not shown), though the relative importance of intraseasonal wind speed and wind stress varies between the regions (Figure 4.11d-f). The consistent dominance of intraseasonal wind speed and stress in causing ISO rectification onto the seasonal cycle of SST suggests that further study is needed to determine how this rectification occurs.

Recall from Section 4.3.3 that in HYCOM, wind can affect the SST via wind stress processes (upwelling, horizontal advection, and mixing due to shear instabilities) and wind speed processes (turbulent heat fluxes and entrainment). In HYCOM, all of these processes are represented by nonlinear terms. Because rectification occurs via nonlinear terms in the model equations, all of these 'wind processes' can contribute to the cross-timescale SST rectification observed in Figures 4.7 and 4.11. Each of the wind processes is estimated as directly as possible to further evaluate its relative importance in the rectification of atmospheric ISOs onto long-timescale SST variability. The complexity of HYCOM's model equations makes it difficult to exactly isolate the impact of an individual process on SST, and impossible to isolate the impacts on hm and upper ocean heat content. It is also difficult to exactly quantify the impacts of intraseasonal wind stress on entrainment, so an estimate is not provided for these impacts. Despite their limitations, the diagnostics described below provide a more in-depth understanding of the processes by which intraseasonal wind can impact seasonal-to-interannual SST variability.

Entrainment and THF are the two processes by which intraseasonal wind speed can affect the seasonal SST cycle, and we evaluate the relative strength of each. Entrainment cooling is generally

Figure 4.11: (a) Same as Figure 4.8a, except for SST averaged over the AS (Region 3a in Figure 4.7c). (b) Same as *a* except averaged over the west equatorial IO (Region 3b in Figure 4.7c). (c) Same as *a* except averaged over the southwest IO (Region 3c in Figure 4.7c). (d) Same as Figure 4.8d, except for SST averaged over the AS. (e) Same as *d* except averaged over the west equatorial IO. (f) Same as *d* except averaged over the southwest IO. Units are °C.

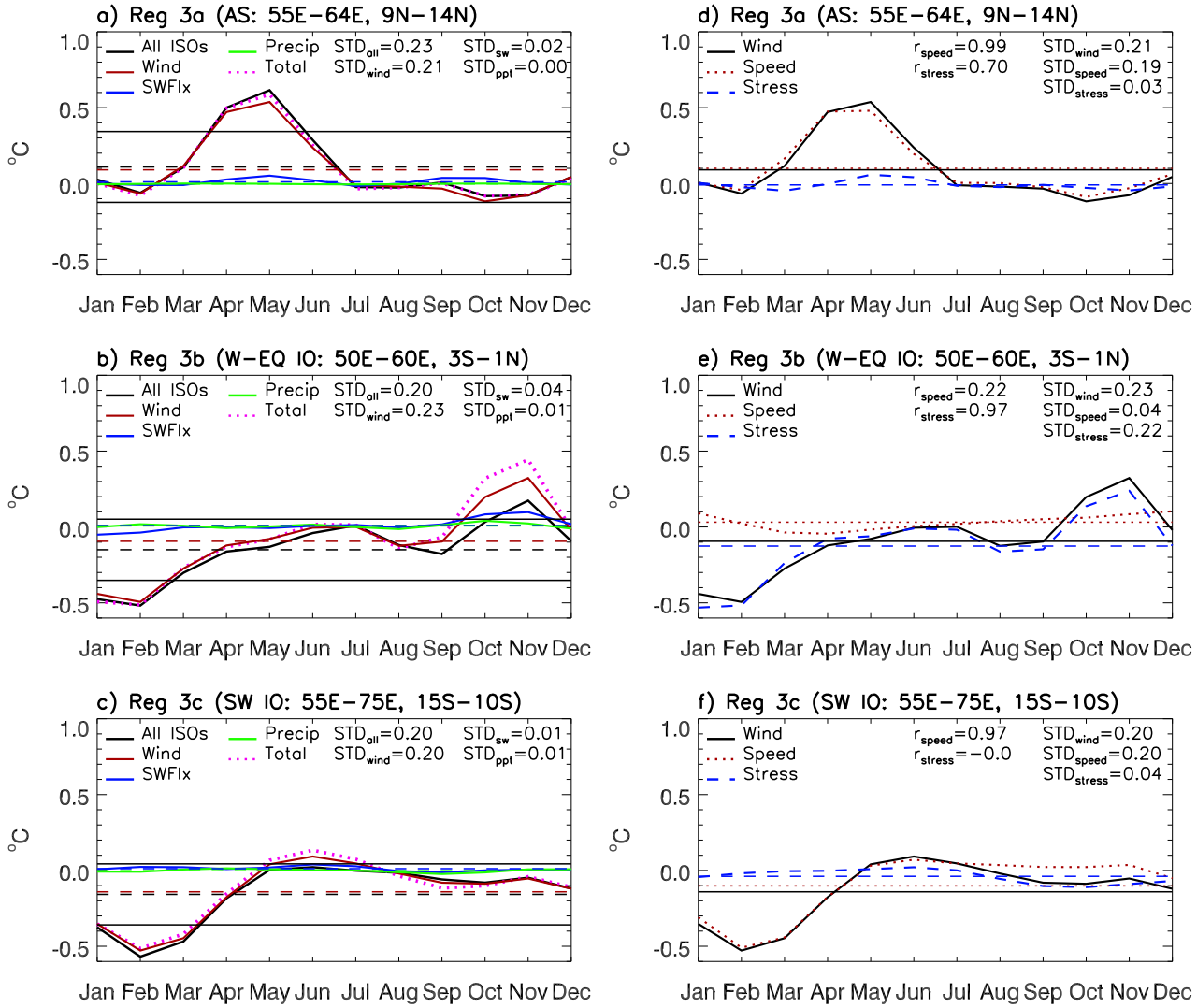

calculated from the vertical temperature gradient over a layer and from an entrainment velocity, which is in turn dependent on the vertical velocity at a depth h and on the total time derivative of h [Stevenson and Niiler, 1983]. For the surface mixed layer, the total time derivative of h (which includes the effects of horizontal advection on h) is dependent on the upwelling velocity at a depth hm and on the entrainment rate [Stevenson and Niiler, 1983]. In difference solution EXP3-EXP4, the model response to any forcing fields except for wind speed are removed. Because the upwelling velocity and currents associated with horizontal advection are functions of wind stress, they are approximately the same in both EXP3 and EXP4, and the difference solution removes these effects. Then, entrainment is primarily determined by the local time derivative of h. In this work, the term 'entrainment' is meant to describe the effects of the turbulent frictional velocity (u^*; calculated from wind speed) and stratification changes due to THF on the temperature of the mixed layer. Mixed layer thickness (hm) due only to wind speed is therefore used to diagnose the presence of entrainment in the model output - increased (decreased) entrainment cooling causes a thickening (thinning) of the mixed layer as increasing (decreasing) amounts of cool subsurface water are entrained into the surface mixed layer. The impact of the seasonal rectification of intraseasonal wind speed on entrainment is estimated by calculating the seasonal cycle of hm due only to intraseasonal wind speed (model difference solution EXP4-EXP3; Table 4.2).

The impacts of intraseasonal wind speed on THF are calculated with the formula $THF = HF_{EXP3} - HF_{EXP4}$, where HF is the net heat flux from EXP3 (low-pass wind stress) and EXP4 (low-pass wind stress and speed). In HYCOM, the model output net heat flux is the sum of THF and net radiative flux, where net radiative flux is an ISCCP-FD model forcing field. The net radiative flux portion of HF is the same for EXP3 and EXP4; only the turbulent heat fluxes can vary between the two experiments. Taking the difference between the two HF quantities isolates the changes in THF due only to intraseasonal wind speed. The seasonal cycle of the resulting THF quantity isolates the impact of intraseasonal wind speed on the seasonal cycle of turbulent heat fluxes. Increasingly negative THF indicates that more energy is leaving the ocean due primarily to increased evaporation. Because THF takes time to warm or cool the ocean, a one month lag is

considered in the following analysis. That is, the THF in April is used to evaluate the contribution of THF to an SST anomaly in May.

Changes in SST due to intraseasonal wind stress-induced upwelling are estimated using the formula $Tup_{3d} = w_{EISO}\frac{d}{dz}\left(T - \overline{T}\right)$ where Tup_{3d} is the change in SST over 3 days due to upwelling; w_{EISO} is the Ekman pumping velocity due to intraseasonal wind stress; $\frac{d}{dz}\left(T - \overline{T}\right)$ is the change in temperature variability over the depth of the mixed layer; and dt is the time step (3 days). The Ekman pumping velocity associated with intraseasonal wind stress curl is calculated with the equation $w_{EISO} = \frac{\partial}{\partial x}\left(\frac{\tau_{yISO}}{f}\right) - \frac{\partial}{\partial y}\left(\frac{\tau_{xISO}}{f}\right)$ where x is longitude, y is latitude, f is the Coriolis parameter at a given latitude, and τ_{xISO} and τ_{yISO} are intraseasonal zonal and meridional wind stress, respectively.

In equatorial regions like the western equatorial IO (Region 3b, Figure 4.7c), where the Ekman pumping velocity cannot be calculated, the effects of ISO-forced upwelling are approximated with the ISO wind stress-forced depth of the 20°C isotherm (d20; a widely used indicator of thermocline depth). A shallower d20 indicates that the thermocline is shoaling. If d20 is caused only by intraseasonal wind stress, then the thermocline shoaling must be due to equatorial upwelling. A one month lag is applied before evaluating d20 because of the time that it takes for upwelled water to cool the SST.

Intraseasonal wind stress can also change SST via horizontal advection. This is calculated with the equation $Tadv_{3d} = -\left[u_{ISO}\frac{d}{dx}\left(T - \overline{T}\right) + v_{ISO}\frac{d}{dy}\left(T - \overline{T}\right)\right]dt$, where u_{ISO} and v_{ISO} are intraseasonal wind stress-forced currents, x and y are longitude and latitude, dt is the time step (3 days), and Tup_{3d} is the change in SST over 3 days due to horizontal advection.

In the Arabian Sea and the BOB, the ISO-forced SST seasonal variations have a maximum in April and May (Figure 4.11a; BOB not shown), indicating that rectification is consistently large each April and May from 2002-2008. The similar timing in the Arabian Sea and the BOB is likely due to the strong influence of summer ISOs in the two regions. Because SSTs in the Arabian Sea already exceed 28°C, the ISO-forced seasonal cycle peak of 0.6°C in May can have an important effect on convection there. Consistent with the rectified hm, the large amplitude of the rectified

SST seasonal cycle during April and May in the Arabian Sea and the BOB is mostly caused by intraseasonal wind speed (Figure 4.11d), which suggests that anomalous THF and entrainment cooling are the major causes of the modeled seasonal warming, shortly before the onset of the Indian summer monsoon.

The seasonal variations of intraseasonal wind speed-forced hm (Figure 4.12b) indicate that reduced entrainment causes the mixed layer in the Arabian Sea (BOB) to shoal by up to 63m (0m) in May. At the same time, the ISO-forced THF in the Arabian Sea and the BOB is 0-10Wm^{-2} in April (Figure 4.12e). The seasonal cycles of upwelling and horizontal advection (Tup and Tadv) are negligible in the Arabian Sea and in the BOB in April and May (Figure 4.13b,e), which is expected because intraseasonal wind stress does not play a large role in these seasonal cycle peaks. Note that the magnitude of the seasonal SST peak is greater in the Arabian Sea than in the BOB, which explains the larger magnitudes of hm and THF in the Arabian Sea. Put together, the seasonal cycle of SST in the Arabian Sea and the BOB peaks in April and May, during the inter-monsoon period. ISOs weaken the seasonal winds, causing reduced entrainment (shoaling hm) and reduced evaporation (positive THF), and resulting in consistently warmer SSTs (Figures 4.8-4.9, 4.11-4.13).

In the west equatorial IO, the ISO-forced SST seasonal cycle has a minimum in January (-0.47°C) and February (-0.51°C), and a maximum in November (0.17°C) (Figure 4.11b). Different from the Arabian Sea, intraseasonal wind stress consistently causes the majority of the rectified seasonal cycle, though intraseasonal wind speed does contribute to the November SST seasonal cycle peak (Figure 4.11e). ISO wind speed-forced THF and entrainment play a negligible role in the cooling during January and February, while entrainment is somewhat reduced during the November warming (Figure 4.12). During January, d20 due to intraseasonal wind stress deepens, indicating that upwelling does not contribute to the cooling in January and February (Figure 4.13g). Downwelling contributes slightly to the warming in November. The rectified seasonal dT due to horizontal advection ranges from -0.1°C to -0.25°C during January and February, and it is mixed during November (Figure 4.13d,f). That is, both equatorial upwelling and horizontal advection due to intraseasonal wind stress contribute to the rectified seasonal SST minimum (maximum) in

Figure 4.12: (a-c) Selected months of the seasonal cycle of hm due only to intraseasonal wind speed (HYCOM difference solution EXP3-EXP4). Boxed regions correspond to the SST representative regions of interest in Figure 4.7c. See Section 4.4.4.3 for more details about this calculation. Units are m. (d-f) Same as *a-c* but for turbulent heat flux (THF). Units are Wm^{-2}.

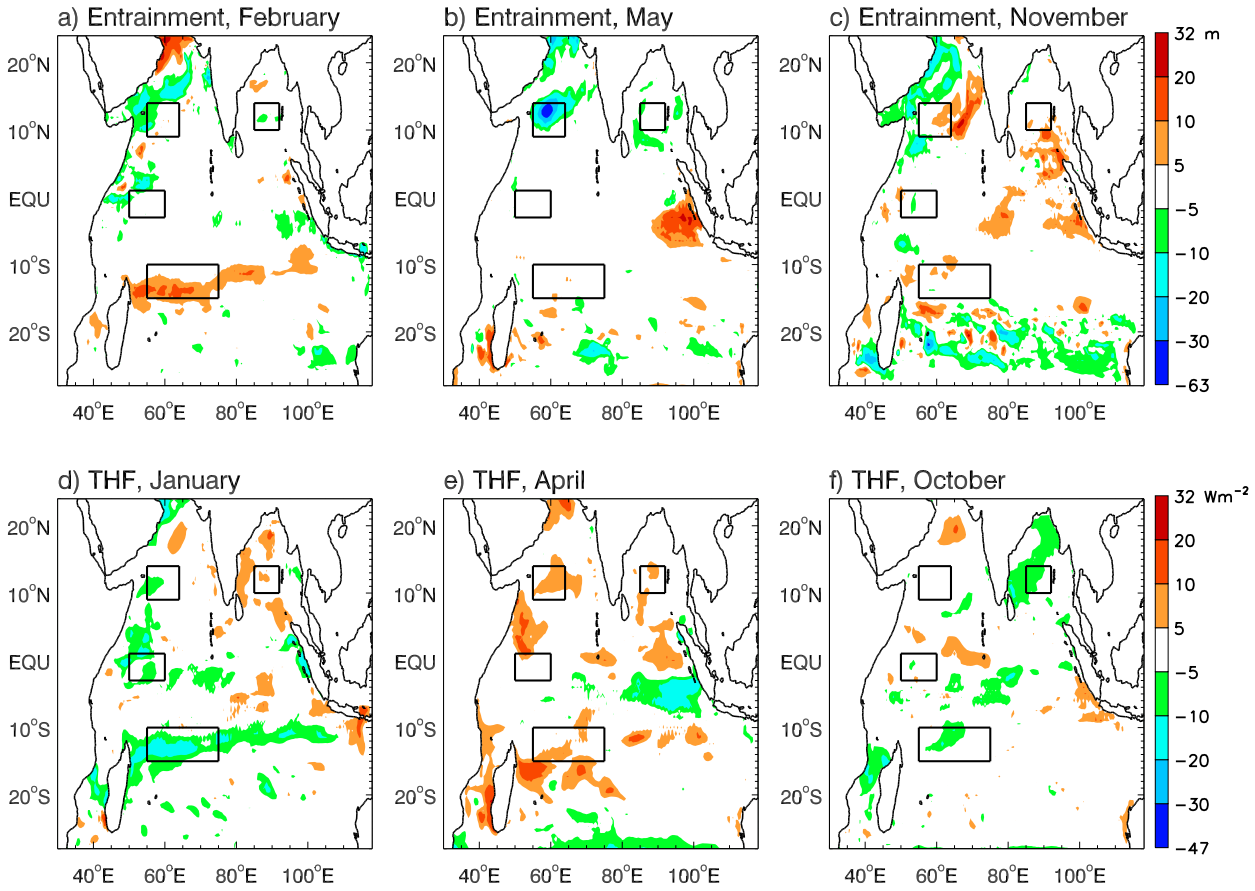

Figure 4.13: (a-c) Selected months of the seasonal cycle of the change in SST (dT) due only to upwelling forced by intraseasonal wind stress. Boxed regions correspond to the SST representative regions of interest in Figure 4.7c. See Section 4.4.4.3 for more details about this calculation. Units are °C. (d-f) Same as *a-c* but due only to horizontal advection forced by intraseasonal wind stress. Units are °C. (g-i) Same as *a-c* but for depth of the 20°C isotherm (d20). Units are m.

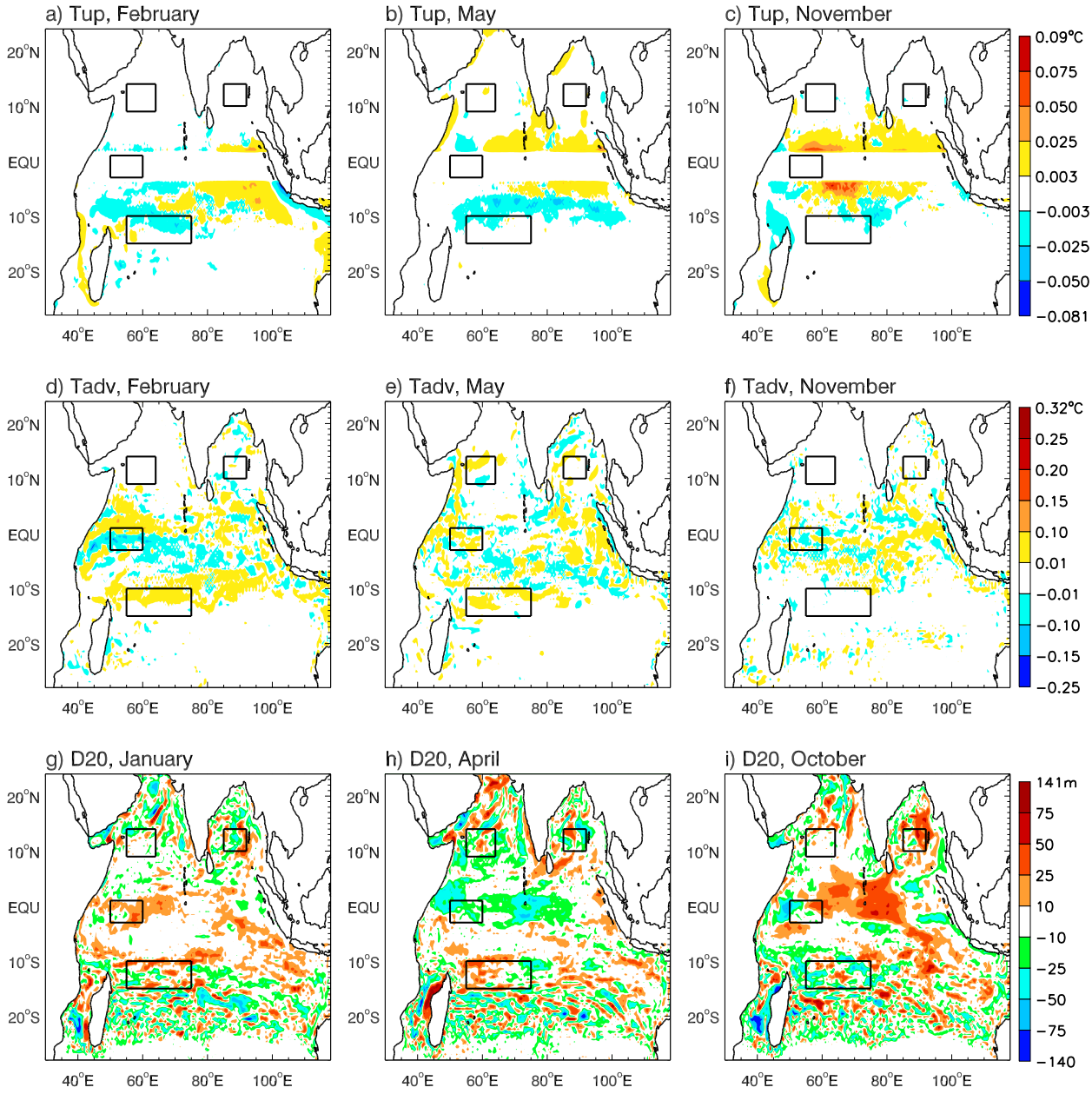

January and February (November), with entrainment due to intraseasonal wind speed contributing slightly during November.

The ISO-forced SST seasonal cycle in the southwest IO has a minimum from January-March, with peak cooling of 0.56°C in February (Figure 4.11c). As in the Arabian Sea, ISO-forced wind speed has a much larger impact than wind stress during each month (Figure 4.11f). Consistent with the dominance of intraseasonal wind speed, intraseasonal wind stress-induced upwelling and horizontal advection do not play significant roles in the seasonal SST cooling in the southwest IO (Figure 4.13a,d). Instead, the increased intraseasonal wind speed in January and February causes increased entrainment cooling (thickened hm) and negative THF (Figure 4.12a,d), which cause rectified seasonal SST cooling.

4.4.5 ISO Rectification on the Interannual Variability of the Upper Ocean

It is clear from Figure 4.6 that atmospheric ISOs rectify onto both the seasonal and the interannual variability of SST, hm, and upper ocean heat content. In order to more fully understand the rectification of ISOs onto the interannual variability of the upper IO, the interannual variability is calculated with equation 4.1 below:

$$T_{iann} = T_{monavg} - T_{monclim} \tag{4.1}$$

T_{monavg} and $T_{monclim}$ are the monthly average and monthly climatology time series, respectively, of 3-day model output data that has been low-pass filtered to 105 days. Monthly averaging the data (i.e. average of Jan 2002, average of Feb 2002, ..., average of December 2008) isolates the seasonal and interannual ocean response. Low-pass filtering the data beforehand ensures that the intraseasonal ocean response is removed. Because the monthly mean climatology (i.e. average January 2002-2008) isolates the seasonal cycle of the ocean response, removing it from the low-pass 105 day filtered, monthly averaged data isolates the interannual ocean response. If data from difference solution MR-EXP1 is used in the equation above, then the atmospheric ISO-forced interannual variability of the ocean is isolated. Other methods can be used to calculate the interannual

variability, such as harmonic analysis and filtering techniques, but we choose to use this simpler, more numerically clean technique.

As with the seasonal cycle analysis in Section 4.4.4 the standard deviations of ISO-forced interannual hm, upper ocean heat content, and SST are used to identify regions with the strongest rectified interannual variability, which are noted with boxes in Figure 4.14. Time series of region-averaged ISO-forced interannual SST, hm, and upper ocean heat content are used to determine the timing of strong rectification (Figures 18-20). Months with strong rectification are those in which the signal change is greater than one standard deviation, and they are evaluated to better understand the processes controlling the rectification of atmospheric ISOs onto interannual upper ocean variability.

4.4.5.1 ISO Rectification on Interannual Hm

Atmospheric ISOs exhibit strong rectification onto interannual hm in many regions of the IO. Here we choose three regions of interest: the Arabian Sea (56°E-66°E, 6°N-14°N), the east equatorial IO (93°E-99°E, 4°S-1°N), and the west equatorial IO (44°E-50°E, 5°S-3°N) (Figure 4.14a). These regions are similar to those with strong seasonal hm rectification (Figure 4.7a). The consistent rectification across timescales in these regions suggests that the interannual hm variability exists as changes in the amplitude of consistent hm shoaling or deepening from year to year. As with the rectification of atmospheric ISOs onto the seasonal cycle, the rectified interannual hm cycle is dominated by intraseasonal wind, rather than by intraseasonal SW radiation or precipitation (Figure 4.15a-c). However, there are exceptions in some regions and during some months, such as during January 2006 in the west equatorial IO, when intraseasonal precipitation contributes to the interannual hm signal (Figure 4.15c). The relative importance of ISO-forced wind speed and wind stress varies from region to region, and from month to month, but it is generally consistent with the results from the seasonal rectification analysis (Section 4.4.4; Figures 4.8 and 4.15d-f). In the Arabian Sea, ISOs tend to shoal the hm during 2002, 2003, and 2005, and they deepen the hm during 2004 and 2006-2008. ISO rectification onto interannual hm also exhibits strong seasonal-

Figure 4.14: Same as Figure 4.7 but for interannual (a) hm, (b) upper ocean heat content, and (c) SST. Units are °C for SST, m for hm, and $10^6 Jm^{-2}$ for heat content.

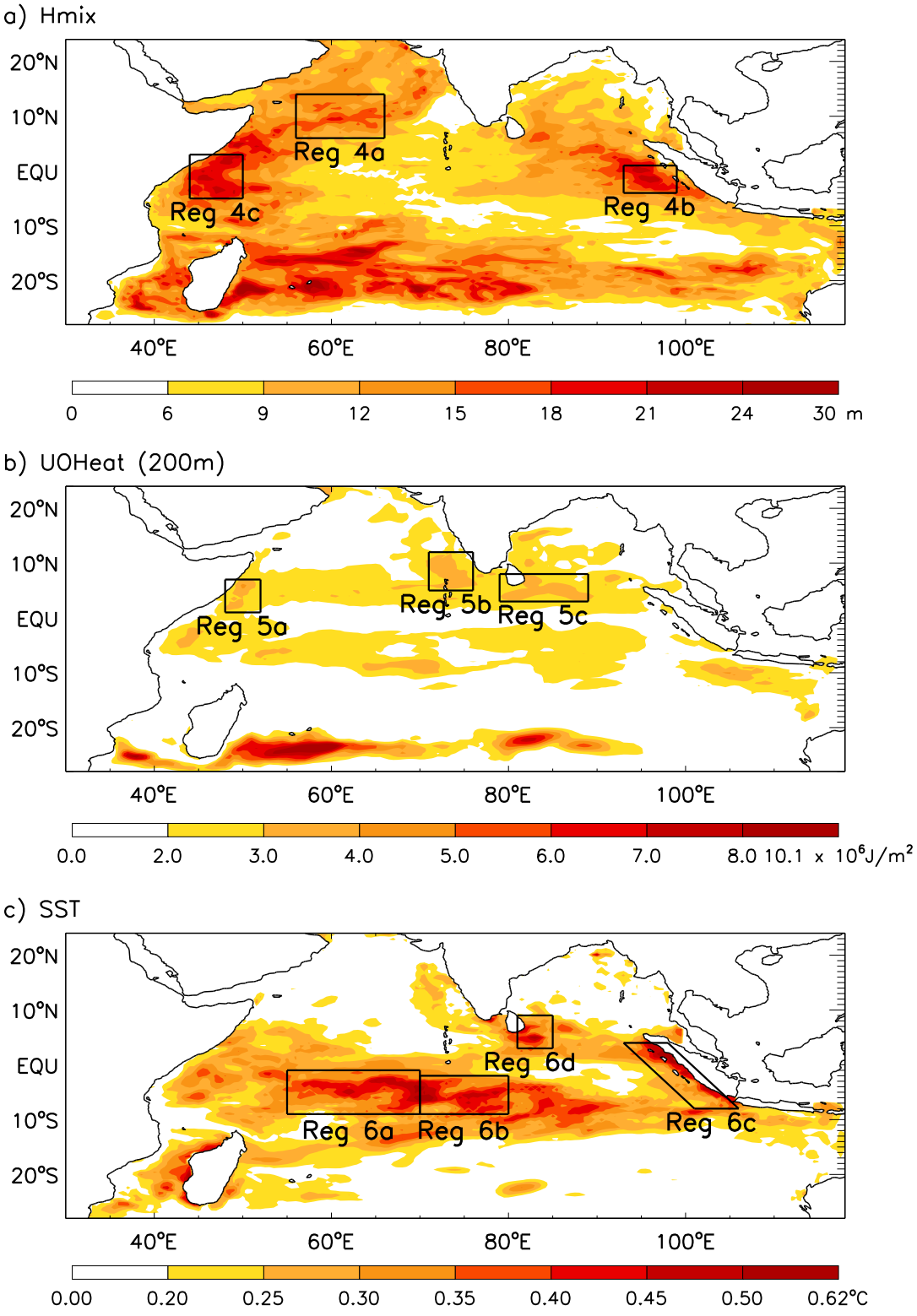

ity: strong rectification tends to occur during boreal fall and winter months in the Arabian Sea and the east equatorial IO, while it occurs during boreal spring and summer in the west equatorial IO (Figure 4.15a-c).

In the Arabian Sea, strong ISO-forced hm rectification occurs in October 2004, when hm deepens by 17.77m, and in November 2007, when hm shoals by 12.37m (Figure 4.15a). Consistent with the rectified seasonal cycle in the Arabian Sea (Section 4.4.4.1), changes in the entrainment rate due to intraseasonal wind speed play a much larger role in the rectified interannual hm signal during both months than upwelling, and horizontal advection, and shear-induced mixing due to wind stress (Figure 4.15d). Both intraseasonal wind stress and wind speed contribute approximately equally to the deepened hm in October 2004.

Strong ISO-forced interannual hm variability occurs in the east equatorial IO during November 2003 (hmix thickens by 27.86m) and December 2007 (hmix shoals by 20m) (Figure 4.15b). Consistent with the rectified hm seasonal cycle in the east equatorial IO, intraseasonal wind stress has a slightly larger impact on interannual hm during both months than changing entrainment due to intraseasonal wind speed (Figure 4.15e).

The strongest ISO-forced interannual hm signal in the west equatorial IO occurs during April 2003 (hm thickens 28.23m) and August 2007 (hm shoals 32m) (Figure 4.15c). Intraseasonal precipitation does play a very small role in the August 2007 shoaling, and it plays a more significant role in interannual hm rectification during early and mid 2006. Different from the processes controlling seasonal hm rectification, ISO-forced wind stress and speed both contribute equally to the April 2003 thickening. However, intraseasonal wind stress plays a much larger role than wind speed during August 2007, which is consistent with the dominant processes that controlled seasonal hm rectification in the region (Figures 4.8 and 4.15f).

4.4.5.2 ISO Rectification on Interannual Upper Ocean Heat Content

Strong ISO-forced interannual upper ocean heat content variability occurs in the IO within 15°S-15°N. Here, we choose three regions with maximum interannual variability: the west equa-

Figure 4.15: Same as Figure 4.8, except for interannual hm from 2002-2008 averaged over (a and d) the AS (Region 4a in Figure 4.14a), (b and e) the east equatorial IO (Region 4b in Figure 4.14a), and (c and f) the west equatorial IO (Region 4c in Figure 4.14a). Horizontal lines in *a-c* represent 1 STD for ISO-forced interannual hm, while those in *d-f* represent zero. Details about calculating interannual variability are in Section 4.4.5. Units are m.

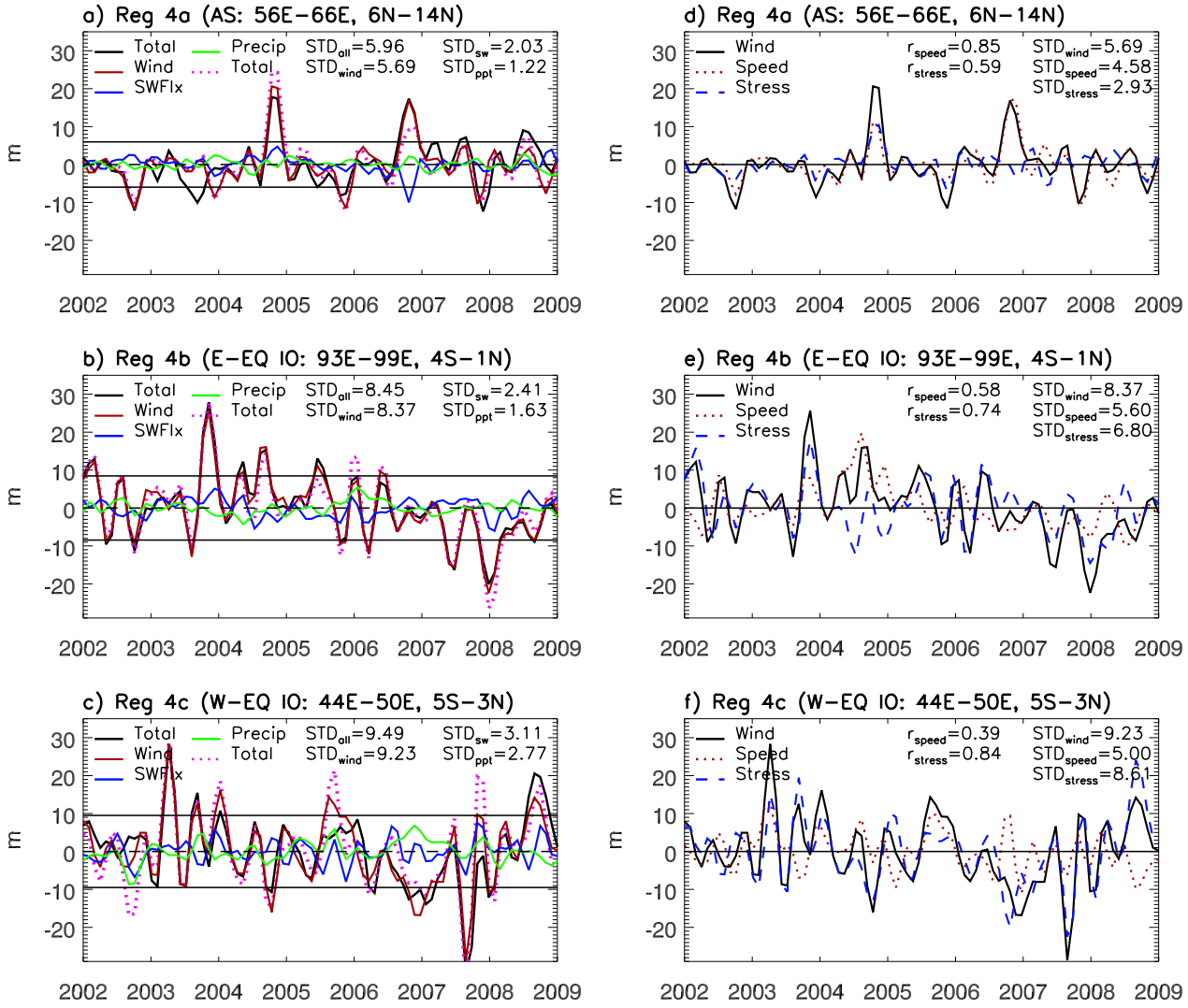

torial IO (48°E-52°E, 1°N-7°N), the southeast Arabian Sea (71°E-76°E, 5°N-12°N), and near Sri Lanka in the southwest BOB (79°E-89°E, 3°N-8°N) (Figure 4.14b). ISO rectification onto seasonal upper ocean heat content is also large in the southeast Arabian Sea (Figure 4.7b), indicating that the interannual variability there represents changes in the amplitude of the rectified seasonal signal from year to year. In general, strong interannual upper ocean heat content rectification occurs during boreal fall and winter when wintertime MJOs are strong, and this rectification is dominated by wind stress in all three regions (Figure 4.16). The deterministic role played by wind stress is consistent with the rectified seasonal variability of upper ocean heat content discussed in Section 4.4.4.2. However, intraseasonal SW radiation and precipitation do contribute significantly during some months, as in the western equatorial IO during boreal fall in 2003 and 2006 (Figure 4.16a-c).

4.4.5.3 ISO Rectification on Interannual SST

The largest ISO impacts on interannual SST are confined to regions from 10°S-10°N. Representative regions where ISO-forced interannual SST anomalies obtain their maxima include the west equatorial IO (55°E-70°E, 9°S-1°S), the central IO (70°E-80°E, 9°S-2°S), the east equatorial IO (94°E-99°E, 3°S-3°N), and the Sri Lanka Dome region (81°E-85°E, 3°N-9°N) (Figure 4.14c). The strongest rectification tends to occur in all of the regions of interest during the boreal late winter, spring, and summer months, with the exception of rectified cooling in the Sri Lanka Dome during October 2004 (Figure 4.17; Sri Lanka Dome not shown). Generally, entrainment and THF due to intraseasonal wind speed, and upwelling, horizontal advection, and shear-induced mixing due to intraseasonal wind stress, have a much larger impact on the rectified interannual SST signal than either intraseasonal SW radiation or precipitation (Figure 4.17). Intraseasonal SW radiation and precipitation do occasionally impact the interannual SST variability. For example, intraseasonal SW radiation contributes to the modeled interannual warming in the central IO during February 2008 (Figure 4.17b). The relative importance of intraseasonal wind speed and stress varies between regions and months (Figure 4.17d-f). As with the rectified seasonal SST analysis (Section 4.4.4.3), the apparent dominance of wind forcing lends itself to further analysis.

Figure 4.16: Same as Figure 4.15, except for interannual upper ocean heat content averaged over (a and d) the west equatorial IO (Region 5a in Figure 4.14b), (b and e) the southeast AS (Region 5b in Figure 4.14b), and (c and f) the southwest BOB (Region 5c in Figure 4.14b). Units are $10^6 Jm^{-2}$.

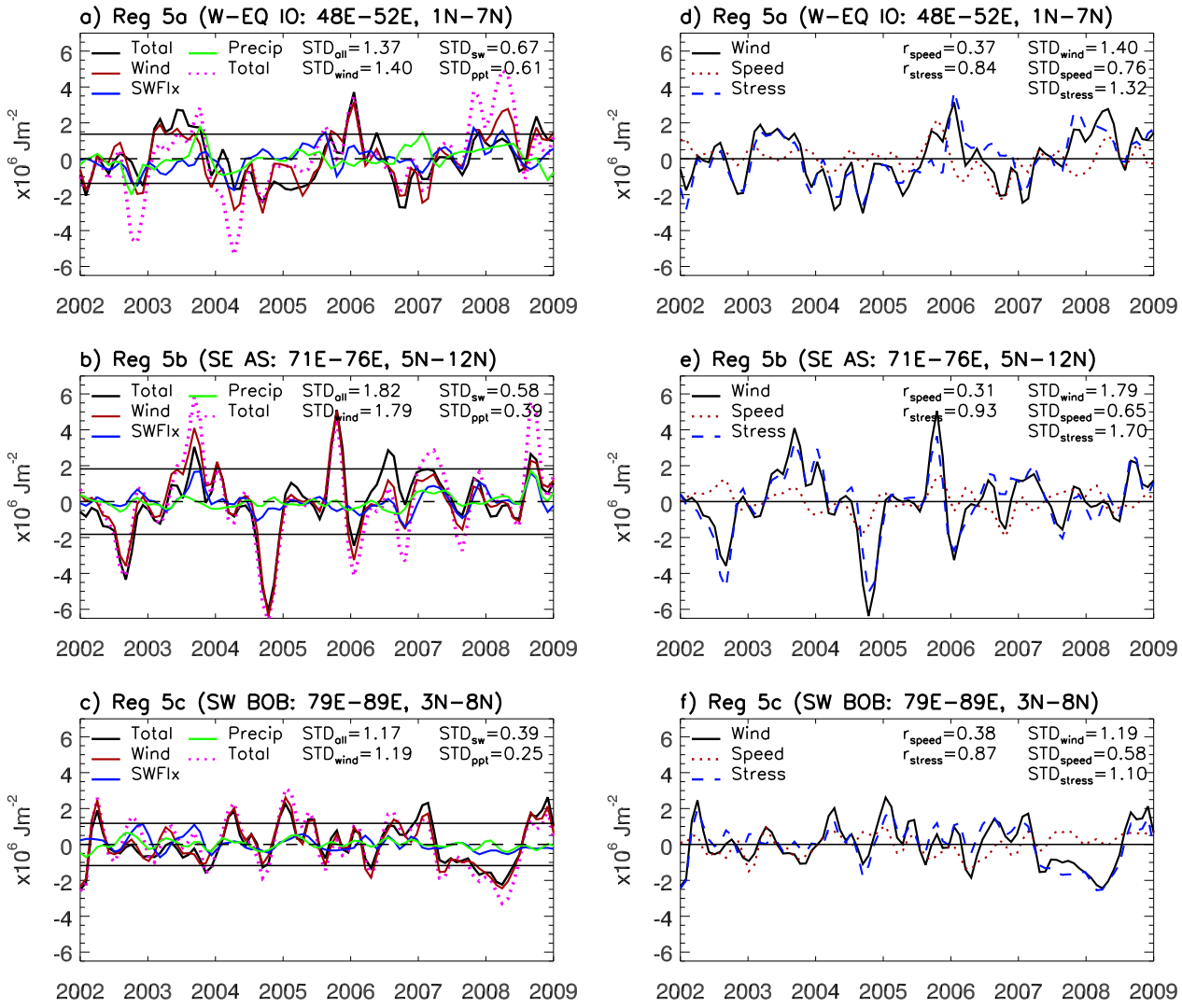

Figure 4.17: Same as Figure 4.16, except for SST averaged over (a and d) the west equatorial IO (Region 6a in Figure 4.14c), (b and e) the central IO (Region 6b in Figure 4.14c), and (c and f) the east equatorial IO (Region 6c in Figure 4.14c). Units are °C.

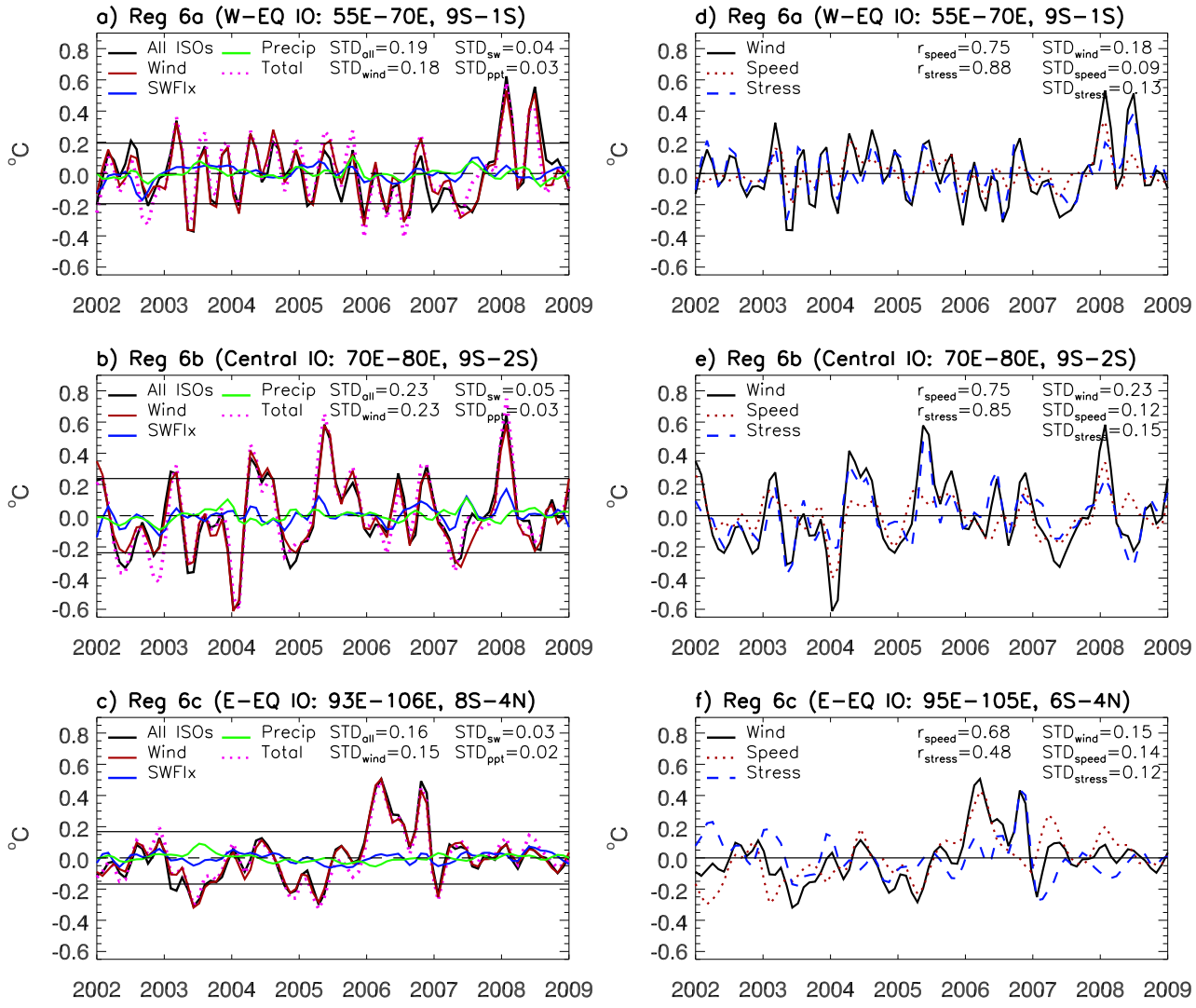

The impacts of intraseasonal wind processes (entrainment, THF, upwelling, horizontal advection, and mixing) on interannual SST are estimated with the same equations used in the regional SST seasonal cycle analysis (Section 4.4.4.3). Instead of isolating the seasonal impacts with monthly climatologies, the interannual impacts are isolated using equation 4.1. As in Section 4.4.4.3, in equatorial regions like the east equatorial IO (Region 6c in Figure 4.14c) , intraseasonal wind stress-forced d20 is used to evaluate the impacts of intraseasonal wind stress-forced upwelling.

During June 2003, strong cooling of $\sim$0.33°C occurs in both the west and east equatorial IO regions (Figure 4.17a,c), due approximately equally to increased intraseasonal wind speed and wind stress (Figure 4.17d,f). In the west equatorial IO, negative THF and upwelling cooling play much larger roles than entrainment cooling and horizontal advection, while entrainment, THF, upwelling, and horizontal advection all contribute in the east equatorial IO (Figures 4.18 and 4.19). During other months in all of the regions of interest, intraseasonal wind speed has a larger impact than wind stress (and vice versa) on the interannual rectification of ISOs. The dominance of processes like entrainment and upwelling vary from month-to-month. For example, strong rectified cooling (0.6°C) occurs during January 2004 in the central equatorial IO (Figure 4.17b). The reduced SSTs are most strongly forced by THF due to intraseasonal wind speed, and to a lesser extent by horizontal advection and upwelling due to intraseasonal wind stress (Figures 4.18 and 4.19b,e). In contrast, horizontal advection does not contribute significantly to the rectified warming ($\sim$0.63°C) found in the west and central equatorial IO during January 2008 (Figure 4.17a,b). These increased SSTs are most strongly forced by entrainment and THF due to intraseasonal wind speed, and by upwelling due to intraseasonal wind stress (Figures 4.18 and 4.19c,f).

4.4.6 ISO Rectification on the Indian Ocean Dipole (IOD)

Because the IOD is an internal mode of interannual variability in the IO, we briefly examine the impacts of atmospheric ISOs on the IOD here. The IOD can be evaluated with the dipole mode index (DMI), which is calculated as the difference in low-frequency SST between the west (50°E-

Figure 4.18: (a-c) Same as Figure 4.12, but for the interannual variability of hm due only to intraseasonal wind speed (HYCOM difference solution EXP3-EXP4). Boxed regions correspond to the SST representative regions of interest in Figure 4.14c. Units are m. (d-f) Same as *a-c* but for turbulent heat flux (THF). Units are Wm^{-2}.

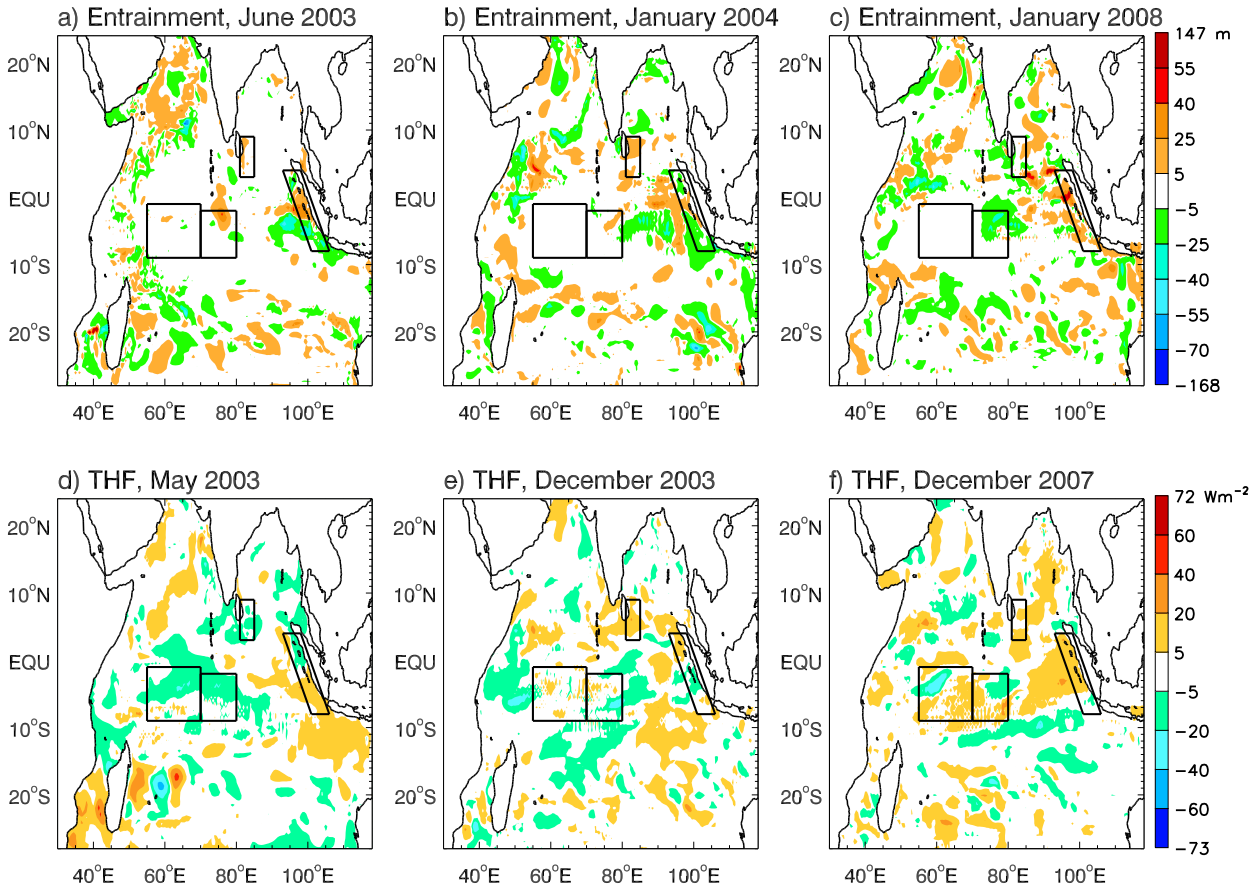

Figure 4.19: (a-c) Same as Figure 4.13, but for the interannual variability of (a-c) the change in SST (dT) due only to upwelling forced by intraseasonal wind stress. Boxed regions correspond to the SST representative regions of interest in Figure 4.14c. Units are °C. (d-f) Same as *a-c* but due only to horizontal advection forced by intraseasonal wind stress. Units are °C. (g-i) Same as *a-c* but for depth of the 20°C isotherm (d20). Units are m.

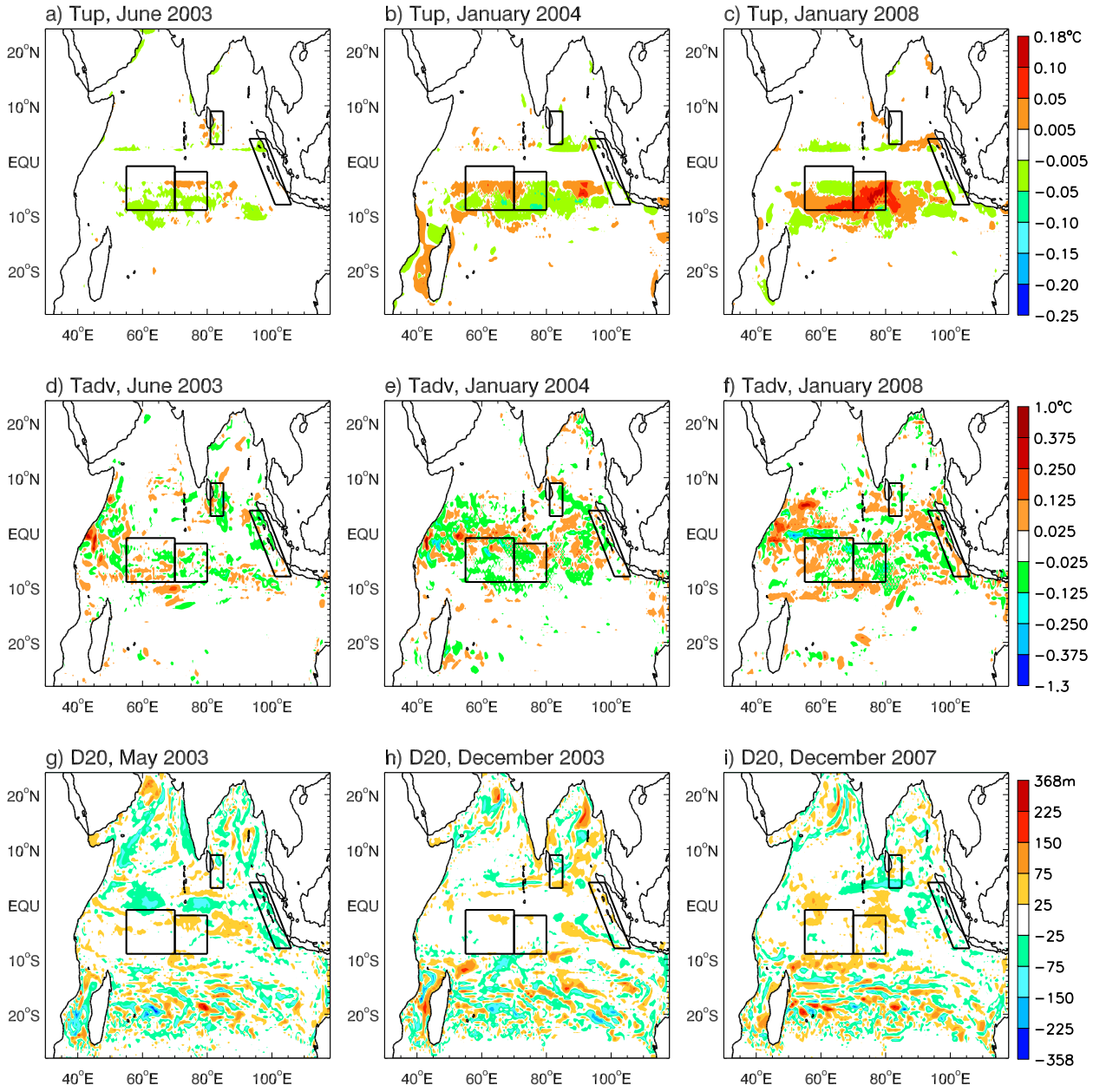

70°E, 10°S-10°N) and east (90°E-110°E, 10°S-Equator) dipole regions [Saji et al., 1999; Webster et al., 1999]. Because we are interested in ISO-forced changes in the mean DMI, the typical step of normalizing the DMI is not used, and the resulting index is referred to as the modified DMI. This modified DMI is calculated twice: once using the monthly averaged SST, and the other using the interannual SST. Both modified DMIs are calculated using SST data from HYCOM MR, HYCOM EXP1, and TRMM (Figure 4.20). The difference between MR and EXP1 (Figure 4.20, black solid and red dotted curves) shows the impact of ISOs on the DMI.

The calculated MR DMI matches the overall pattern of DMI calculated from observations, but the timing of IOD events appears to be shifted by several months. IOD events generally peak in October, while the events determined from the HYCOM DMI tend to peak in spring (see blue dashed and black solid curves during 2006, 2007, and 2008 in Figure 4.20). Excluding seasonal SSTs from the DMI calculations does not improve the timing of IOD events identified with the HYCOM DMI (Figure 4.20b). The DMI calculated from TRMM data shows positive IOD events with the correct fall timing in 2006, 2007, and 2008 (blue dashed curves in Figure 4.20). It should be noted that the model experiments only include atmospheric forcings over the IO, so important IOD forcings like the westerly wind bursts in the Pacific Ocean are excluded.

The amplitude of modeled IOD events can be much smaller than observed, which at times means that the model bias is larger than the modeled ISO impacts on the IOD. For example, during October 2006, the observed DMI is greater than 2°C, while the modeled DMI is $\sim$0.1°C and ISOs contribute $\sim$0.4°C to the modeled DMI. It appears that ISO impacts on the IOD are very small, as shown during months with a relatively small model bias like March 2005. However, the large model bias makes it difficult to conclude this with confidence. The large bias is likely due to problems in modeling the East IO with HYCOM. Time series of the interannual SST averaged over the east and west dipole regions reveal that SSTs are not well modeled over the east dipole region (Figure 4.21, black solid and red dotted curves). Correlation coefficients between HYCOM MR and TRMM interannual SSTs are 0.562 and 0.097 in the west and east dipole regions, respectively. As discussed in Section 4.3.1, forcing due to the ITF is included in the model experiments by relaxing the model

Figure 4.20: Modified Indian Ocean Dipole Mode Index (IOD DMI) for (a) seasonal + interannual (monthly averaged) and (b) interannual SST due to all forcing periods (MR, black curves), excluding ISOs (EXP1, red dotted curves), and from observed TRMMv4 0.25°x0.25° data (blue dashed curves). Horizontal lines in *a* represent the mean DMI due to each dataset. Horizontal black lines in *a* and *b* represent 1 STD for the MR DMI and are used to identify strong IOD events. The mean DMI due to each forcing is calculated and displayed in *a*. The STD due to each forcing is calculated and displayed in *a* and *b*. Units are °C.

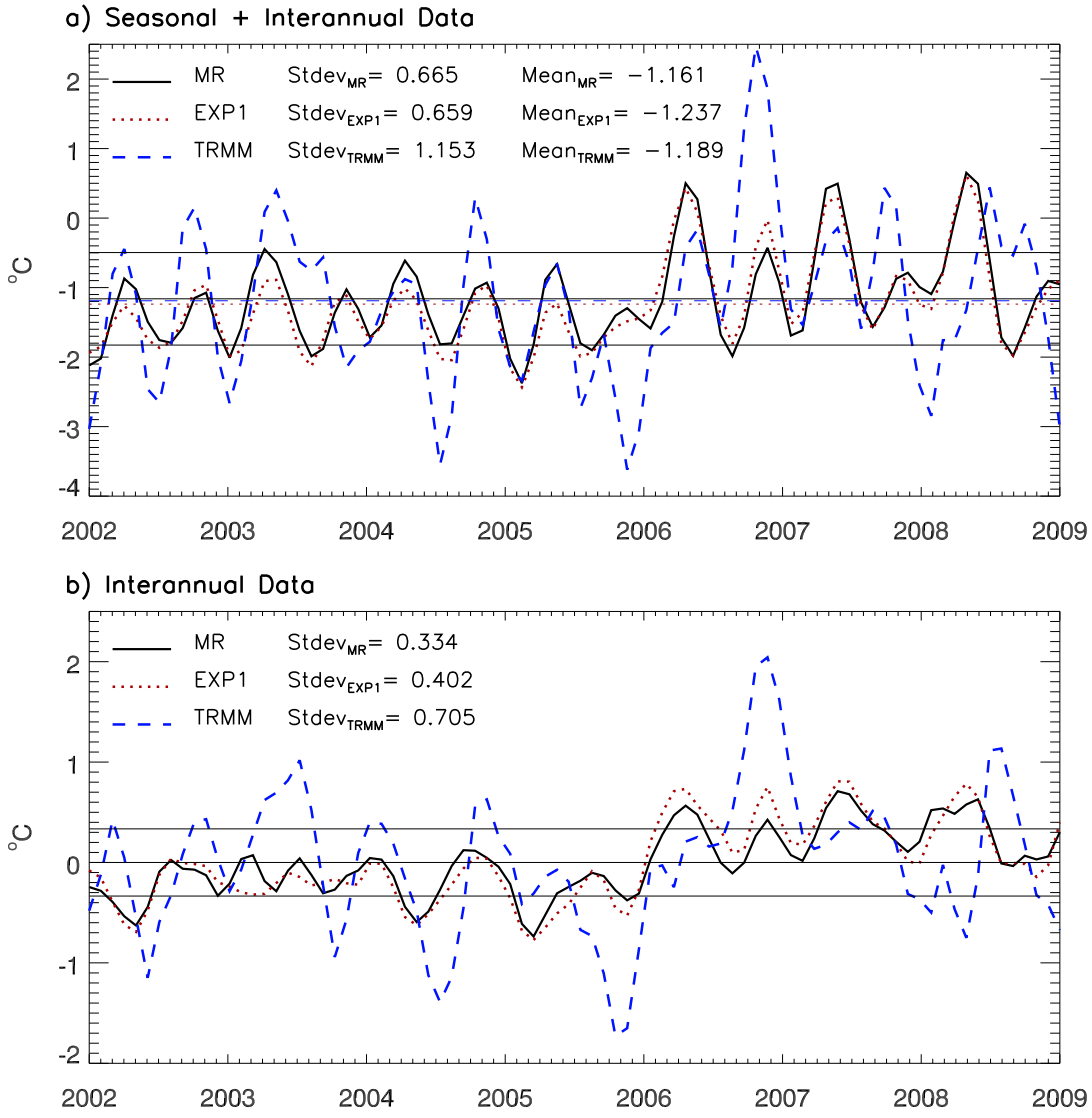

temperature and salinity to Levitus and Boyer [1994] and to Levitus et al. [1994] climatology. Expanding the model domain to include real atmospheric forcing in the ITF region would likely improve the model bias.

Atmospheric ISOs have a small impact on the mean DMI, increasing it by just 0.076°C (Figure 4.20a). In general, ISOs have a larger impact on the DMI when the index is weak than when it is strong (greater than 1 standard deviation; Figure 4.20). From 2002-2005, there is not a strong positive IOD event, but ISOs impact the DMI by 0.46°C in April 2003, 0.4°C in April 2004 and 0.56°C in May 2005. These changes account for 100% of the total DMI in March 2003, 65% of the total DMI in April 2004, and 85% of the total DMI in May 2005. By contrast, during strong IOD events in April 2006, May 2007, and April 2008, ISOs change the DMI by -0.07°C (13.5%), 0.2°C (39.7%), and 0.1°C (5%), respectively.

ISOs can enhance or weaken strong IOD events. For example, atmospheric ISOs increase the DMI during positive events in 2007 and 2008, but they reduce the positive DMI during April 2006. It is clear that factors other than atmospheric ISOs are dominant in determining IOD events. At the same time, atmospheric ISOs do contribute in a minor way to strong IOD events, and in a larger way when the DMI is small.

4.5 Summary and Conclusions

In the present study, the impacts of atmospheric ISOs on seasonal to interannual upper ocean variability are analyzed using a hierarchy of experiments with the OGCM HYCOM. Experiments are forced with different timescales and processes, as detailed in Table 4.1. Difference solutions that are calculated from the experiments (Table 4.2) allow us to isolate the ocean response to full ISOs and to a range of individual intraseasonal forcing fields. The low-frequency model response to these forcing fields is determined by calculating the seasonal and interannual variability from monthly mean climatology and monthly mean data. HYCOM model equations and other commonly used process equations are used to calculate the impacts of entrainment, THF, upwelling, and horizontal advection on ISO-forced seasonal and interannual SSTs in the IO.

Figure 4.21: Same as Figure 4.4c,d except (a) averaged over the west dipole region of the IO (50°E-70°E, 10°S-10°N), and (b) averaged over the east dipole region of the IO (90°E-110°E, 10°S-EQ). Units are °C.

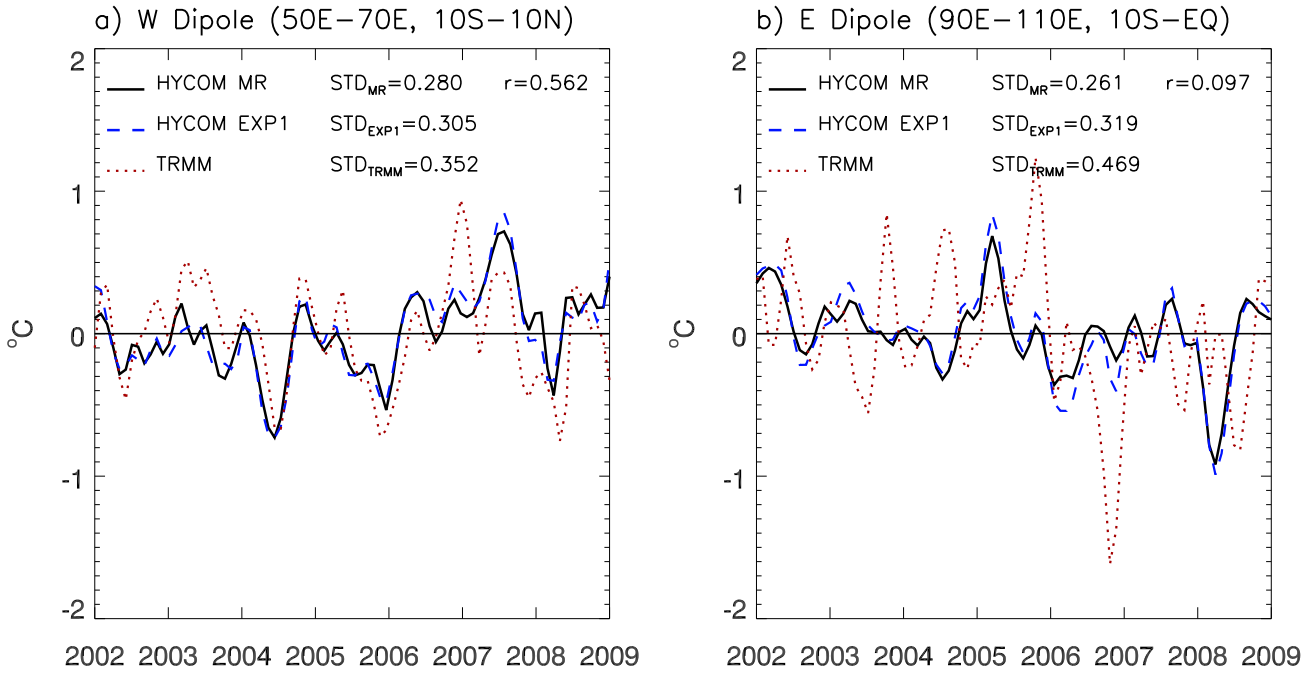

In general, the model indicates that atmospheric ISOs do rectify onto the mean and standard deviation of SST, hm, and upper ocean heat content, and the impacts of this rectification vary regionally (Figures 4.5 and 4.6). Spatial plots of the changes in mean SST, hm, upper ocean heat content, and mixed layer heat content due to ISOs (Figure 4.5) show that atmospheric ISOs warm (shoal) the mean SST (hm) by as much as 0.2°C (10m) in the AS and the BOB. The largest shifts in mean SST, hm, and mixed layer heat content due to ISOs occur along the Sumatran coastline, where SSTs cool by 0.1°C-0.9°C, hm thickens by 3m-12m, and mixed layer heat content increases by 5-25$\times 10^6 Jm^{-2}$. ISOs change the mean upper ocean heat content by up to -(+)5.5$\times 10^6 Jm^{-2}$ in the far north (south) IO near 55°E, and by up to $3\times 10^6 Jm^{-2}$ in the BOB and across the IO near 5°N.

The standard deviations of ISO-forced low frequency (seasonal + interannual) SST, hm, upper ocean heat content, and mixed layer heat content (Figure 4.6) reveal that low-frequency rectification of ISOs is also highly regional. The strongest ISO rectification onto low frequency variability occurs in many of the regions with the strongest ISO impacts on the mean state. Regions with the maximum ISO impact on the mean state and standard deviation of hm and mixed layer heat content are almost identical (Figure 4.5b,d and 4.6b,d). Even in regions where ISOs cause the mean SST to decrease, the mixed layer heat content increases as hm thickens. It appears that hm is the dominant factor in determining mixed layer heat content.

Atmospheric ISOs have a large impact on the modeled seasonal and interannual cycles of SST, hm, and upper ocean heat content in a number of climatically relevant representative regions of the IO (Figures 4.7 and 4.14). The standard deviations of ISO-forced seasonal SST, hm, and upper ocean heat content are used to identify regions with the strongest ISO rectification, and these are boxed in Figures 4.7 and 4.14. Further study focuses on the strength of rectification in these regions, and on the processes that cause it.

Time series of the region-averaged ISO-forced seasonal cycles and interannual variability of SST, hm, and upper ocean heat content are used to identify the months during which low-frequency rectification is consistently strong from 2002-2008. Similarly, time series that use the model differ-

ence solutions from Table 4.2 are used to determine the dominant processes that cause the observed rectification (Figures 4.8, 4.10, and 4.11; 4.15-4.17). In general, entrainment and THF due to intraseasonal wind speed, and upwelling and horizontal advection due to intraseasonal wind stress play a much larger role than intraseasonal SW radiation and precipitation in causing low-frequency rectification of atmospheric ISOs on SST, hm, and upper ocean heat content. However, the relative importance of wind speed and wind stress generally varies between signals, regions, and months. Exceptions to this are the rectified seasonal cycle of upper ocean heat content in all regions of interest, and the seasonal cycle of hm in the BOB, all of which are consistently dominated by intraseasonal wind stress (Figure 4.10).

To further evaluate the processes by which intraseasonal wind speed and stress cause seasonal to interannual SST rectification, we determine the relative strength of intraseasonally forced seasonal and interannual entrainment, THF, upwelling, and horizontal advection. In decomposing the processes by which intraseasonal wind speed and wind stress can change the low-frequency SST, we gain a better understanding of how the modeled rectification occurs. All four processes contribute in varying amounts to seasonal and interannual rectification from month to month, and from region to region.

There is consistently strong atmospheric ISO rectification onto the seasonal cycle of SST in the Arabian Sea and the BOB in April and May (Figure 4.11a). During these inter-monsoon months, the intraseasonally-forced seasonal SST warms by 0.6°C, which can impact convection over the already warm Arabian Sea. The rectified SST signal is most strongly forced by intraseasonal wind speed. Intraseasonal wind stress, precipitation, and SW radiation all play a reduced role (Figure 4.11a,d). During April and May in the Arabian Sea and the BOB, intraseasonal wind speeds decrease, causing reduced entrainment (shoaling hm; Figure 4.12) and increased THF due to reduced evaporation (Figure 4.12), and resulting in consistently warmer SSTs (Figure 4.11a,d).

The strongest ISO impacts on interannual SST are found in the Arabian Sea, the equatorial IO (with some overlap with the western dipole formation region), the east equatorial IO (near the eastern dipole formation region), and in the Sri Lanka Dome region (Figure 4.14c). Generally,

intraseasonal wind dominates intraseasonal SW radiation and precipitation, although the latter two processes contribute to interannual SST rectification during some months in some regions (Figure 4.17). Entrainment and THF due to intraseasonal wind speed and upwelling, horizontal advection, and mixing due to intraseasonal wind stress contribute in varying amounts to ISO rectification onto interannual SST.

The regions with strong atmospheric ISO rectification onto seasonal and interannual hm variability are very similar. In addition, there is strong rectification onto seasonal and interannual upper ocean heat content in the Arabian Sea. These similarities across timescales indicate that interannual hm and upper ocean heat content variability in these regions represent changes in the amplitude of the seasonal cycle of hm and upper ocean heat content from year to year (Figures 4.7 and 4.14).

Our model results show that atmospheric ISOs can have an important impact on the seasonal-to-interannual variability of the upper layers of the IO. This work presents results from a clean experimental design that can easily be reproduced using a range of models and forcing fields. Future work using coupled atmosphere-ocean models and using a range of different forcing products could be used to confirm the robustness of our results. It would also be valuable to use a similarly designed experiment to evaluate the impact of ISOs on known specific low-frequency features like the Wyrtki Jet, the IO thermocline ridge, and the IOD in more detail.

Chapter 5

Discussion and Conclusions

The work presented in this dissertation contributes to the relatively limited body of knowledge about atmosphere-ocean interactions in the Indian Ocean (IO). Increased understanding about these interactions can be important for understanding the initiation and propagation of atmospheric intraseasonal oscillations (ISOs), which have in turn been shown to contribute to the development, evolution, strength, and termination of major climate events like the Indian summer monsoon, the El Nino Southern Oscillation (ENSO), and the Indian Ocean Dipole (IOD). The impacts of ISOs on intraseasonal sea surface temperature (SST) variability, and the upper ocean mean and seasonal and interannual variability, are evaluated using the OGCM HYCOM and a range of observational datasets. The magnitude of these impacts and the processes that control the rectified and non-rectified upper ocean response are studied in detail.

It is hoped that the expanded insights about atmosphere-ocean interactions presented in this dissertation will contribute to improved modeling of atmospheric ISOs, and by extension, of climate-scale events in the IO and surrounding regions. The major findings of this dissertation research are summarized below.

5.1 Intraseasonal IO Response to Atmospheric ISOs During Boreal Summer

In Chapter 3, a series of seven experiments is set up and run for the years 1998-2004 using HYCOM, which is configured to the IO only (Table 3.1). Some experiments contain filtered datasets, and their output is used alone and in difference solutions to isolate the ocean's response

to ISOs, and to entrainment and turbulent heat flux (THF) due to intraseasonal wind speed, upwelling and horizontal advection (and possibly mixing induced by shear instabilities) due to wind stress, shortwave (SW) radiation, and precipitation. The intraseasonal ocean response to these forcing fields is determined by first low-pass filtering the model output to 105 days, which excludes periods less than 105 days, and then calculating the difference between the filtered and the unfiltered data to primarily isolate the ocean response with periods from 10-90 days (the intraseasonal response).

Comparisons between the submonthly and Madden-Julian Oscillation (MJO)-scale filtered forcing fields and ocean response show that while the boreal summer submonthly wind and radiation forcing is stronger than the MJO-scale forcing, the MJO-scale ocean response is stronger. The longer duration of the forcing associated with MJOs allows for them to force a larger amplitude ocean response than the shorter-lived but stronger Quasi-Biweekly Mode (QBM) forcing. Regions with strong intraseasonal convection and wind forcing often coincide with a strong intraseasonal SST response. The three regions with the strongest boreal summer forcing and responses are located in the Arabian Sea, the Bay of Bengal, and the east IO warm pool. In the Arabian Sea, the maximum warming (cooling) is 0.67°C (0.73°C), which is smaller than in the other two regions of interest. The reduced amplitude response in the Arabian Sea is likely because the mixed layer is thicker there than in the Bay of Bengal and the east IO warm pool, so forcings must act on a thicker layer to produce changes in SST. In the Bay of Bengal, the maximum warming (cooling) is 0.78°C (1.08°C), and in the eastern IO warm pool it is 0.83°C (1.09°C). The mean summer SSTs exceed 28°C-29°C in all three regions. As a result, these ISO-forced intraseasonal SST changes may have important implications for convection in the regions.

Generally, 30-90 day winds cause much larger 30-90 day SST variability than either 30-90 day SW radiation or precipitation during boreal summer in the IO. In the Arabian Sea, surface THF and entrainment cooling forced by changes in MJO wind speed have a slightly larger effect on 30-90 day SST than either upwelling or horizontal advection due to MJO-scale wind stress. The same relationship holds but is much stronger in the Bay of Bengal, while the effects of MJO

wind speed (entrainment and THF) and wind stress (upwelling, horizontal advection, and mixing induced by shear instability) are comparable in the east equatorial IO. The submonthly SST impacts of submonthly forcing fields are the same as the MJO-scale relationships described above, although they are somewhat weaker.

More detailed analysis of the IO response to specific MJO and submonthly events yields deeper insight into the air-sea interactions in the three regions of interest. For example, in the Bay of Bengal, the effects of THF caused by MJO wind speed appear to be larger than the effects of entrainment. The apparent importance of THF in the Bay of Bengal is attributed to the modeled and observed barrier layer and thin mixed layer there. The thin mixed layer is a result of strong stratification in the region. This strong stratification inhibits entrainment mixing, while the barrier layer means that any entrainment that does occur cannot have a large impact on the SST there.

5.2 Rectification of Atmospheric ISOs onto the Mean and Seasonal-to-Interannual Upper Ocean Variability

Extending from the work in Chapter 3, a similar set of HYCOM experiments is performed from 2000-2008 to evaluate the presence, strength, and processes that control the rectification of atmospheric ISOs onto the mean and seasonal-to-interannual variability of the upper IO (Table 4.1). As in Chapter 3, the model experiments contain both filtered and unfiltered forcings that are used alone and in difference solutions (Table 4.2) to calculate the full ocean response to ISOs and to individual intraseasonal forcing fields associated with the ISOs.

Results of this study show that atmospheric ISOs can cause significant rectification onto the mean and seasonal-to-interannual variability in the upper IO, and that the rectification is particularly strong in some regions. The regions with the strongest rectified signal vary between seasonal and interannual timescales, and between SST, hm, and upper ocean heat content. For example, atmospheric ISOs have a large impact on the seasonal cycle of SST in the Arabian Sea (0.6°C in May), the thermocline ridge region (-0.51°C in February and 0.17°C in November), the southwest IO (-0.56°C in March), and the Bay of Bengal (0.6°C in May). The maximum ISO-forced inter-

annual variability of SST occurs in the west equatorial IO (0.622°C), the central IO (0.644°C), the east equatorial IO (0.58°C), and in the Sri Lanka dome region (0.518°C).

Across both rectified timescales and their associated regions of interest, intraseasonal wind speed and wind stress have a much larger impact on the rectified SST, hm, and upper ocean heat content signals than intraseasonal SW radiation and precipitation. The rectified contributions of ISO-forced entrainment, THF, upwelling, and horizontal advection are estimated, and they show that all four processes contribute in varying amounts to strong seasonal and interannual events in the regions. However, none of these processes is consistently dominant. The mean and rectified variability of mixed layer heat content and hm have very similar spatial structures. When SSTs cool, hm thickens and mixed layer heat content thickens, suggesting that hm, rather than SST, controls mixed layer heat content. The mean rectified seasonal upper ocean heat content is consistently positive, which indicates that atmospheric ISOs may act as a heat pump, increasing the seasonal heat content of the upper ocean.

5.3 Future Work

The research presented in this dissertation lends itself to future work that falls into two distinct categories: evaluating the robustness of these conclusions, and expanding the scope of this work. The experimental design used in this work was carefully developed to cleanly separate the ocean response to individual forcing fields with specific time periods. For example, two model experiments were run in order to isolate the IO response to intraseasonal wind. The first, experiment MR, used the complete 3-day model forcing fields, while the second, experiment EXP4, excluded intraseasonal wind from the forcing fields. The difference between 'everything' (MR) and 'everything but' (EXP4) isolated the 'but' (intraseasonal wind). The framework developed in this research, and in Han et al. [2007], can easily be extended to any range of modeling projects. In addition, it allows for the results presented in this thesis to be verified using the same experimental design, but with different forcing fields or ocean models.

Following this, it would be valuable to complete additional HYCOM runs using other forcing

fields such as the recently released ERA-interim dataset [Simmons et al., 2007], cross-calibrated multiplatform (CCMP) 6-hourly merged satellite winds (1987-present; Atlas et al. [2011]), NASA Scatterometer/National Centers for Environmental Prediction (NSCAT/NCEP) 6-hourly winds [Milliff et al., 1999], and precipitation from the Tropical Rainfall Measuring Mission (TRMM) Multi-satellite Precipitation Analysis (TMPA; Huffman et al. [2007]). If our model results hold using multiple sets of forcing data, then the conclusions can be considered to be more robust. HYCOM could also be run using a range of different mixing schemes, such as the Krauss-Turner and Mellor-Yamada vertical mixing submodels [Kraus and Turner, 1967; Mellor and Yamada, 1982], and the Redi, Gent-McWilliams, and Fox-Kemper mesoscale mixing parameterizations [Redi, 1982; Gent and McWilliams, 1990; Fox-Kemper et al., 2011]. These mixing schemes might allow for more accurate modeling of smaller-scale processes, which could translate to more accurate model results. For example, small-scale mixing processes can impact the modeled mixed layer thickness, which can in turn affect the strength of entrainment or upwelling cooling in the mixed layer. Forcing an atmospheric GCM with the SST fields from HYCOM experiments with and without ISO forcing would shed some light on the air-sea interaction processes associated with ISO initiation and propagation, and on the role played by ISOs in the coupled ocean-atmosphere climate system. Running a coupled ocean-atmosphere GCM might allow for more realistic ISO-forced air-sea interactions, which could provide additional insights into the processes that control these interactions.

Considering the importance of the tropical Pacific Ocean in the development of the IOD and the impacts of ISOs on ENSO, it might also be valuable to repeat our HYCOM experiments with a larger model domain that encompasses both the IO and the tropical Pacific Ocean. A wider-domain HYCOM run would allow for a more detailed and accurate study of the impacts of ISOs on the IOD and ENSO. It would be interesting to evaluate why the impacts of ISOs appear to be smaller during strong DMI years than during weak DMI years. Other seasonal-to-interannual features in the IO would be interesting to evaluate. For example, the Wyrtki Jets discussed in Chapter 1 can have important implications for heat and water mass transport in the IO, and they tend to form during break periods between the Indian monsoon seasons. Because of the strong connections between

MJOs, the QBM, and the Indian summer monsoon, it is possible that atmospheric ISOs have an impact on the timing or strength of the Wyrtki Jets as well.

Bibliography

Annamalai, H., Liu, P., and Xie, S. P. (2005). Southwest Indian Ocean SST variability: Its local effect and remote influence on Asian monsoons. Journal of Climate, 18(20):4150--4167.

Ashok, K., Guan, Z. Y., and Yamagata, T. (2001). Impact of the Indian Ocean Dipole on the relationship between the Indian monsoon rainfall and ENSO. Geophysical Research Letters, 28(23):4499--4502.

Atlas, R., Hoffman, R. N., Ardizzone, J., Leidner, S. M., Jusem, J. C., Smith, D. K., and Gombos, D. (2011). A cross-calibrated, multiplatform ocean surface wind velocity product for meteorological and oceanographic applications. Bulletin of the American Meteorological Society, 28(23):157--154.

Bajuk, L. J. and Levoy, C. B. (1998). Seasonal and interannual variations in stratiform and convective clouds over the tropical Pacific and Indian Oceans from ship observations. Journal of Climate, 11(11):2922--2941.

Bhat, G. S., Gadgil, S., Kumar, P. V. H., Kalsi, S. R., Madhusoodanan, P., Murty, V. S. N., Rao, C., Babu, V. R., Rao, L. V. G., Rao, R. R., Ravichandran, M., Reddy, K. G., Rao, P. S., Sengupta, D., Sikka, D. R., Swain, J., and Vinayachandran, P. N. (2001). BOBMEX: The Bay of Bengal Monsoon Experiment. Bulletin of the American Meteorological Society, 82(10):2217--2243.

Bleck, R. (2002). An oceanic general circulation model framed in hybrid isopycnic-cartesian coordinates. Ocean Modelling, 4(1):55--88.

Boyer, T. P., Antonov, J. I., Baranova, O. K., Garcia, H. E., Johnson, D. R., Locarnini, R. A., Mishonov, A. V., O'Brien, T. D., Seidov, D., Smolyar, I. V., and Zweng, M. M. (2009). World Ocean Database 2009. In Levitus, S., editor, NOAA Atlas NESDIS 66, page 216. U.S. Gov. Printing Office, Wash., D.C.

Chatterjee, P. and Goswami, B. N. (2004). Structure, genesis and scale selection of the tropical quasi-biweekly mode. Quarterly Journal of the Royal Meteorological Society, 130(599):1171--1194.

Chen, T. C. and Chen, J. M. (1993). The 10-20-day mode of the 1979 Indian monsoon - its relation with the time-variation of monsoon rainfall. Monthly Weather Review, 121(9):2465--2482.

Del Genio, A. D. and Kovari, W. (2002). Climatic properties of tropical precipitating convection under varying environmental conditions. Journal of Climate, 15(18):2597--2615.

Donguy, J. R. and Meyers, G. (1995). Observations of geostrophic transport variability in the western tropical Indian Ocean. Deep Sea Research, Part I, 42(6):1007--1028.

Duchon, C. E. (1979). Lanczos filtering in one and 2 dimensions. Journal of Applied Meteorology, 18(8):1016--1022.

Duncan, B. and Han, W. Q. (2009). Indian Ocean intraseasonal sea surface temperature variability during boreal summer: Madden-Julian Oscillation versus submonthly forcing and processes. Journal of Geophysical Research-Oceans, 114.

Duvel, J. P., Roca, R., and Vialard, J. (2004). Ocean mixed layer temperature variations induced by intraseasonal convective perturbations over the Indian Ocean. Journal of the Atmospheric Sciences, 61(9):1004--1023.

Duvel, J. P. and Vialard, J. (2007). Indo-Pacific sea surface temperature perturbations associated with intraseasonal oscillations of tropical convection. Journal of Climate, 20(13):3056--3082.

Emanuel, K. (2001). Contribution of tropical cyclones to meridional heat transport by the oceans. Journal of Geophysical Research-Atmospheres, 106(D14):14771--14781.

Flatau, M., Flatau, P. J., Phoebus, P., and Niller, P. P. (1997). The feedback between equatorial convection and local radiative and evaporative processes: The implications for intraseasonal oscillations. Journal of the Atmospheric Sciences, 54(19):2373--2386.

Fox-Kemper, B., Danabasoglu, G., Ferrari, R., Griffies, S. M., Hallberg, R. W., Holland, M. M., Maltrud, M. E., Peacock, S., and Samuels, B. L. (2011). Parameterization of mixed layer eddies. III: Implementation and impact in global ocean climate simulations. Ocean Modelling, 39:61--78.

Fu, R., Delgenio, A. D., and Rossow, W. B. (1994). Influence of ocean surface conditions on atmospheric vertical thermodynamic structure and deep convection. Journal of Climate, 7(7):1092--1108.

Fu, X. H., Wang, B., Li, T., and McCreary, J. P. (2003). Coupling between northward-propagating, intraseasonal oscillations and sea surface temperature in the Indian Ocean. Journal of the Atmospheric Sciences, 60(15):1733--1753.

Gadgil, S., Vinayachandran, P. N., and Francis, P. A. (2004). Extremes of the Indian summer monsoon rainfall, ENSO and equatorial Indian Ocean oscillation. Geophysical Research Letters, 31(12).

Gent, P. R. and McWilliams, J. C. (1990). Isopycnal mixing in ocean circulation models. J. Phys. Oceanogr., 20:150□155.

Goddard, L. and Graham, N. E. (1999). The importance of the Indian Ocean for simulating precipitation anomalies over eastern and southern Africa. Journal of Geophysical Research, 104:19099--19116.

Gordon, A. L. (2005). Oceanography of the Indonesian Seas and their Throughflow. Oceanography, 18(4).

Halkides, D. J., Han, W. Q., Lee, T., and Masumoto, Y. (2007). Effects of sub-seasonal variability on seasonal-to-interannual Indian Ocean meridional heat transport. Geophysical Research Letters, 34(12).

Halkides, D. J. and Lee, T. (2011). Mechanisms controlling seasonal mixed layer temperature and salinity in the southwestern tropical Indian Ocean. Dynamics of Atmospheres and Oceans, 52(3):77--93.

Halliwell, G. R. (2004). Evaluation of vertical coordinate and vertical mixing algorithms in the HYbrid-Coordinate Ocean Model (HYCOM). Ocean Modelling, 7(3-4):285--322.

Han, W. Q. (2005). Origins and dynamics of the 90-day and 30-60-day variations in the equatorial Indian Ocean. Journal of Physical Oceanography, 35(5):708--728.

Han, W. Q., Lawrence, D. M., and Webster, P. J. (2001). Dynamical response of equatorial Indian Ocean to intraseasonal winds: zonal flow. Geophysical Research Letters, 28(22):4215--4218.

Han, W. Q., Liu, W. T., and Lin, J. L. (2006a). Impact of atmospheric submonthly oscillations on sea surface temperature of the tropical Indian Ocean. Geophysical Research Letters, 33(3).

Han, W. Q., McCreary, J. P., Anderson, D. L. T., and Mariano, A. J. (1999). Dynamics of the eastern surface jets in the equatorial Indian Ocean. Journal of Physical Oceanography, 29(9):2191--2209.

Han, W. Q., Shinoda, T., Fu, L. L., and McCreary, J. P. (2006b). Impact of atmospheric intraseasonal oscillations on the Indian Ocean dipole during the 1990s. Journal of Physical Oceanography, 36(4):670--690.

Han, W. Q., Webster, P., Lukas, R., Hacker, P., and Hu, A. X. (2004). Impact of atmospheric intraseasonal variability in the Indian Ocean: Low-frequency rectification in equatorial surface current and transport. Journal of Physical Oceanography, 34(6):1350--1372.

Han, W. Q., Webster, P. J., Lin, J. L., Liu, W. T., Fu, R., Yuan, D. L., and Hu, A. X. (2008). Dynamics of intraseasonal sea level and thermocline variability in the equatorial Atlantic during 2002-03. Journal of Physical Oceanography, 38(5):945--967.

Han, W. Q., Yuan, D. L., Liu, W. T., and Halkides, D. J. (2007). Intraseasonal variability of Indian Ocean sea surface temperature during boreal winter: Madden-Julian Oscillation versus submonthly forcing and processes. Journal of Geophysical Research-Oceans, 112(C4).

Harrison, D. E. and Vecchi, G. A. (2001). January 1999 Indian Ocean cooling event. Geophysical Research Letters, 28(19):3717--3720.

Hendon, H. H. and Glick, J. (1997). Intraseasonal air-sea interaction in the tropical Indian and Pacific Oceans. Journal of Climate, 10(4):647--661.

Hendon, H. H. and Salby, M. L. (1996). Planetary-scale circulations forced by intraseasonal variations of observed convection. Journal of the Atmospheric Sciences, 53(12):1751--1758.

Hermes, J. C. and Reason, C. J. C. (2008). Annual cycle of the South Indian Ocean (Seychelles-Chagos) thermocline ridge in a regional ocean model. Journal of Geophysical Research - Oceans, 113(C4).

Howden, S. D. and Murtugudde, R. (2001). Effects of river inputs into the Bay of Bengal. Journal of Geophysical Research-Oceans, 106(C9):19825--19843.

Huffman, G. J., Adler, R. F., Bolvin, D. T., Gu, G., Nelkin, E. J., Bowman, K. P., Stocker, E. F., and Wolff, D. B. (2007). The TRMM Multi-satellite Precipitation Analysis: Quasi-Global, Multi-Year, Combined-Sensor Precipitation Estimates at Fine Scale. Journal of Hydrometeorology, 8(C9):33--55.

Inness, P. M. and Slingo, J. M. (2003). Simulation of the Madden-Julian Oscillation in a coupled general circulation model. Part I: Comparison with observations and an atmosphere-only GCM. Journal of Climate, 16(3):345--364.

Jerlov, N. G. (1976). Marine Optics. Elsevier, New York.

Jochum, M. and Murtugudde, R. (2005). Internal variability of Indian Ocean SST. Journal of Climate, 18(18):3726--3738.

Jones, C., Waliser, D. E., and Gautier, C. (1998). The influence of the Madden-Julian Oscillation on ocean surface heat fluxes and sea surface temperature. Journal of Climate, 11(5):1057--1072.

Kara, A. B., Rochford, P. A., and Hurlburt, H. E. (2000). Efficient and accurate bulk parameterizations of air-sea fluxes for use in general circulation models. Journal of Atmospheric and Oceanic Technology, 17(10):1421--1438.

Kara, A. B., Wallcraft, A. J., and Hurlburt, H. E. (2005a). A new solar radiation penetration scheme for use in ocean mixed layer studies: An application to the Black Sea using a fine-resolution Hybrid Coordinate Ocean Model (HYCOM). Journal of Physical Oceanography, 35(1):13--32.

Kara, A. B., Wallcraft, A. J., and Hurlburt, H. E. (2005b). Sea surface temperature sensitivity to water turbidity from simulations of the turbid Black Sea using HYCOM. Journal of Physical Oceanography, 35(1):33--54.

Kemball-Cook, S. and Wang, B. (2001). Equatorial waves and air-sea interaction in the boreal summer intraseasonal oscillation. Journal of Climate, 14(13):2923--2942.

Kessler, W. S. (2005). The oceans. In Lau, W. K. M. and Waliser, D. E., editors, Intraseasonal Variability in the Atmosphere-Ocean Climate System, pages 175--222. Springer, New York.

Kessler, W. S. and Kleeman, R. (2000). Rectification of the Madden-Julian Oscillation into the ENSO cycle. Journal of Climate, 13(20):3560--3575.

Kessler, W. S., McPhaden, M. J., and Weickmann, K. M. (1995). Forcing of intraseasonal Kelvin waves in the equatorial Pacific. Journal of Geophysical Research-Oceans, 100(C6):10613--10631.

Kiladis, G. N. and Weickmann, K. M. (1997). Horizontal structure and seasonality of large-scale circulations associated with submonthly tropical convection. Monthly Weather Review, 125(9):1997--2013.

Kim, H. M., Hoyos, C. D., Webster, P. J., and Kang, I. S. (2010). Ocean-atmosphere coupling and the boreal winter MJO. Climate Dynamics, 35(5):771--784.

Klingaman, N. P., Woolnough, S. J., Weller, H., and Slingo, J. M. (2011). The impact of finer-resolution air-sea coupling on the intraseasonal oscillation of the Indian monsoon. Journal of Climate, 24(10):2451--2468.

Knauss, J. A. (1996). Introduction to Physical Oceanography. Prentice-Hall, New Jersey.

Kraus, E. B. and Turner, J. S. (1967). A one-dimensional model of seasonal thermocline 2. general theory and its consequences. Tellus, 19(1).

Krishnamurti, T. N., Oosterhof, D. K., and Mehta, A. V. (1988). Air sea interaction on the time scale of 30 to 50 days. Journal of the Atmospheric Sciences, 45(8):1304--1322.

Krishnamurti, T. N. and Subrahmanyam, D. (1982). The 30-50 day mode at 850 mb during MONEX. Journal of the Atmospheric Sciences, 39(9):2088--2095.

Kumar, K. K., Kumar, K. R., Ashrit, R. G., Deshpande, N. R., and Hansen, J. W. (2004). Climate impacts on Indian agriculture. International Journal of Climatology, 24(11):1375--1393.

Large, W. G., Danabasoglu, G., Doney, S. C., and McWilliams, J. C. (1997). Sensitivity to surface forcing and boundary layer mixing in a global ocean model: Annual-mean climatology. Journal of Physical Oceanography, 27(11):2418--2447.

Large, W. G., McWilliams, J. C., and Doney, S. C. (1994). Oceanic vertical mixing - a review and a model with a nonlocal boundary-layer parameterization. Reviews of Geophysics, 32(4):363--403.

Large, W. G. G. and Gent, P. R. (1999). Validation of vertical mixing in an equatorial ocean model using large eddy simulations and observations. Journal of Physical Oceanography, 29(3):449--464.

Lau, K. M. and Chan, P. H. (1985). Aspects of the 40-50 day oscillation during the northern winter as inferred from outgoing longwave radiation. Monthly Weather Review, 113(11):1889--1909.

Lau, K. M. and Chan, P. H. (1988). Intraseasonal and interannual variations of tropical convection - a possible link between the 40-50 day oscillation and ENSO. Journal of the Atmospheric Sciences, 45(3):506--521.

Lau, K. M. and Waliser, D. E. (2005). Intraseasonal Variability in the Atmosphere-Ocean System. Springer, New York.

Levitus, S. and Boyer, T. P. (1994). Temperature, NOAA Atlas NESDIS 4. In World Ocean Atlas 1994, volume 4, page 129. NOAA, Silver Spring, Md.

Levitus, S., Burgett, R., and Boyer, T. P. (1994). Salinity, NOAA Atlas NESDIS 3. In World Ocean Atlas 1994, volume 3, page 111. NOAA, Silver Spring, Md.

Li, T. M. and Wang, B. (1994). The influence of sea-surface temperature on the tropical intraseasonal oscillation - a numerical study. Monthly Weather Review, 122(10):2349--2362.

Liebmann, B. and Smith, C. A. (1996). Description of a complete (interpolated) outgoing longwave radiation dataset. Bulletin of the American Meteorological Society, 77(6):1275--1277.

Lin, J. L., Kiladis, G. N., Mapes, B. E., Weickmann, K. M., Sperber, K. R., Lin, W., Wheeler, M. C., Schubert, S. D., Del Genio, A., Donner, L. J., Emori, S., Gueremy, J. F., Hourdin, F., Rasch, P. J., Roeckner, E., and Scinocca, J. F. (2006). Tropical intraseasonal variability in 14 IPCC AR4 climate models. Part I: Convective signals. Journal of Climate, 19(12):2665--2690.

Livezey, R. E. and Chen, W. Y. (1983). Statistical field significance and its determination by monte-carlo techniques. Monthly Weather Review, 111(1):46--59.

Lukas, R. and Lindstrom, E. (1991). The mixed layer of the western equatorial Pacific-Ocean. Journal of Geophysical Research-Oceans, 96:3343--3357.

Luther, D. S., Harrison, D. E., and Knox, R. A. (1983). Zonal winds in the central equatorial Pacific and El-Nino. Science, 222(4621):327--330.

Madden, R. A. and Julian, P. R. (1971). Detection of a 40-50 day oscillation in zonal wind in tropical Pacific. Journal of the Atmospheric Sciences, 28(5):702--&.

Madden, R. A. and Julian, P. R. (1972). Description of global-scale circulation cells in tropics with a 40-50 day period. Journal of the Atmospheric Sciences, 29(6):1109--&.

Madden, R. A. and Julian, P. R. (1994). Observations of the 40-50-day tropical oscillation - a review. Monthly Weather Review, 122(5):814--837.

Masumoto, Y. and Meyers, G. (1998). Forced Rossby waves in the southern tropical Indian Ocean. Journal of Geophysical Research - Oceans, 103(C12):27589--27602.

McBride, J. (1987). The Australian summer monsoon. In Chang, C. P. and Krishnamurti, T. N., editors, Reviews of Monsoon Meteorology, pages 203--231. Oxford University Press, New York.

McCreary, J. P., Kundu, P. K., and Molinari, R. L. (1993). A numerical investigation of dynamics, thermodynamics, and mixed-layer processes in the Indian Ocean. Progress in Oceanography, 31(3):181--244.

McPhaden, M. J. (1982). Variability in the central equatorial Indian-Ocean, .2. Oceanic heat and turbulent energy balances. Journal of Marine Research, 40(2):403--419.

McPhaden, M. J. (1999). Genesis and evolution of the 1997-98 El Nino. Science, 283(5404):950--954.

Mellor, G. L. and Yamada, T. (1982). Development of a turbulence closure-model for geophysical fluid problems. Reviews of Geophysics, 20(4):851--875.

Milliff, R. F., Large, W. G., Morzel, J., Danabasoglu, G., and Chin, T. M. (1999). Ocean general circulation model sensitivity to forcing from scatterometer winds. J. Geophys. Res., 104(C5):11337--11358.

Moore, A. M. and Kleeman, R. (1999). Stochastic forcing of ENSO by the intraseasonal oscillation. Journal of Climate, 12(5):1199--1220.

Murakami, T. and Frydrych, M. (1974). Preferred period of upper wind fluctuations during summer monsoon. Journal of the Atmospheric Sciences, 31(6):1549--1555.

Murtugudde, R., McCreary, J. P., and Busalacchi, A. J. (2000). Oceanic processes associated with anomalous events in the Indian Ocean with relevance to 1997-1998. Journal of Geophysical Research-Oceans, 105(C2):3295--3306.

Nagura, M. and McPhaden, M. J. (2010). Wyrtki jet dynamics: Seasonal variability. Journal of Geophysical Research-Oceans, 115.

Numaguti, A. (1995). Characteristics of 4-20-day-period disturbances observed in the equatorial Pacific during the TOGA COARE IOP. Journal of the Meteorological Society of Japan, 73(2B):353--377.

O'Brien, J. J. and Hurlburt, H. E. (1974). Equatorial Jet in Indian Ocean - Theory. Science, 184(4141):1075--1077.

Prasad, T. G. and Hogan, P. J. (2007). Upper-ocean response to Hurricane Ivan in a 1/25 degrees nested Gulf of Mexico HYCOM. Journal of Geophysical Research-Oceans, 112(C4).

Price, J. F. (1981). Upper ocean response to a hurricane. Journal of Physical Oceanography, 11:153--175.

Rao, R. R. and Sivakumar, R. (1999). On the possible mechanisms of the evolution of a mini-warm pool during the pre-summer monsoon season and the genesis of onset vortex in the south-eastern Arabian Sea. Quarterly Journal of the Royal Meteorological Society, 125(555):787--809.

Rao, S. A., Luo, J. J., Behera, S. K., and Yamagata, T. (2009). Generation and termination of Indian Ocean Dipole events in 2003, 2006 and 2007. Climate Dynamics, 33(6):751--767.

Rao, S. A. and Yamagata, T. (2004). Abrupt termination of Indian Ocean dipole events in response to intraseasonal disturbances. Geophysical Research Letters, 31(19):4.

Redi, M. H. (1982). Oceanic isopycnal mixing by coordinate rotation. Journal of Physical Oceanography, 12:1154--1158.

Saji, N. H., Goswami, B. N., Vinayachandran, P. N., and Yamagata, T. (1999). A dipole mode in the tropical Indian Ocean. Nature, 401(6751):360--363.

Saji, N. H., Xie, S. P., and Tam, C. Y. (2006). Satellite observations of intense intraseasonal cooling events in the tropical south Indian Ocean. Geophysical Research Letters, 33(14).

Schiller, A. and Godfrey, J. S. (2003). Indian Ocean intraseasonal variability in an ocean general circulation model. Journal of Climate, 16(1):21--39.

Schott, F. A., Xie, S. P., and McCreary, J. P. (2009). Indian Ocean circulation and climate variability. Reviews of Geophysics, 47.

Selvaraju, R. (2003). Impact of El Nino-Southern Oscillation on Indian foodgrain production. International Journal of Climatology, 23(2):187--206.

Sengupta, D., Goswami, B. N., and Senan, R. (2001). Coherent intraseasonal oscillations of ocean and atmosphere during the Asian summer monsoon. Geophysical Research Letters, 28(21):4127--4130.

Shaji, C., Wang, C., Halliwell, G. R., and Wallcraft, A. (2005). Simulation of tropical Pacific and Atlantic oceans using a Hybrid Coordinate Ocean Model. Ocean Modelling, 9(3):253--282.

Shinoda, T. and Han, W. Q. (2005). Influence of the Indian Ocean dipole on atmospheric subseasonal variability. Journal of Climate, 18(18):3891--3909.

Shinoda, T. and Hendon, H. H. (1998). Mixed layer modeling of intraseasonal variability in the tropical Western Pacific and Indian Oceans. Journal of Climate, 11(10):2668--2685.

Shinoda, T. and Hendon, H. H. (2002). Rectified wind forcing and latent heat flux produced by the Madden-Julian Oscillation. Journal of Climate, 15:3500--3508.

Shinoda, T., Hendon, H. H., and Glick, J. (1998). Intraseasonal variability of surface fluxes and sea surface temperature in the tropical western Pacific and Indian Oceans. Journal of Climate, 11(7):1685--1702.

Sikka, D. R. and Gadgil, S. (1980). On the maximum cloud zone and the ITCZ over Indian longitudes during the southwest monsoon. Monthly Weather Review, 108(11):1840--1853.

Simmons, A., Uppala, S., Dee, D., and Kobayashi, S. (2007). ERA-Interim: New ECMWF reanalysis products from 1989 onwards. ECMWF Newsletter, 110:25--35.

Slingo, J. M., Sperber, K. R., Boyle, J. S., Ceron, J. P., Dix, M., Dugas, B., Ebisuzaki, W., Fyfe, J., Gregory, D., Gueremy, J. F., Hack, J., Harzallah, A., Inness, P., Kitoh, A., Lau, W. K. M., McAvaney, B., Madden, R., Matthews, A., Palmer, T. N., Park, C. K., Randall, D., and Renno, N. (1996). Intraseasonal oscillations in 15 atmospheric general circulation models: Results from an AMIP diagnostic subproject. Climate Dynamics, 12(5):325--357.

Sperber, K. R., Gualdi, S., Legutke, S., and Gayler, V. (2005). The Madden-Julian oscillation in ECHAM4 coupled and uncoupled general circulation models. Climate Dynamics, 25(2-3):117--140.

Sprintall, J. and Tomczak, M. (1992). Evidence of the barrier layer in the surface-layer of the tropics. Journal of Geophysical Research-Oceans, 97(C5):7305--7316.

Sriver, R. L. and Huber, M. (2007). Observational evidence for an ocean heat pump induced by tropical cyclones. Nature, 447(7144):577--580.

Stevenson, J. W. and Niiler, P. P. (1983). Upper ocean heat budget during the Hawaii-to-Tahiti shuttle experiment. Journal of Physical Oceanography, 13(10):1894--1907.

Takayabu, Y. N., Iguchi, T., Kachi, M., Shibata, A., and Kanzawa, H. (1999). Abrupt termination of the 1997-98 El Nino in response to a Madden-Julian Oscillation. Nature, 402(6759):279--282.

Tang, W. and Liu, W. T. (1996). Objective interpolation of scatterometer winds. In Publ. 96-19, page 16. Jet Propulsion Lab, Pasadena, CA.

Vialard, J., Foltz, G. R., McPhaden, M. J., Duvel, D. P., and Montegut, C. D. (2008). Strong Indian Ocean sea surface temperature signals associated with the Madden-Julian Oscillation in late 2007 and early 2008. Geophysical Research Letters, 35(19).

Vincent, D. G., Fink, A., Schrage, J. M., and Speth, P. (1998). High- and low-frequency intraseasonal variance of OLR on annual and ENSO timescales. Journal of Climate, 11(5):968--986.

Waliser, D. E., Lau, K. M., and Kim, J. H. (1999). The influence of coupled sea surface temperatures on the Madden-Julian Oscillation: A model perturbation experiment. Journal of the Atmospheric Sciences, 56(3):333--358.

Waliser, D. E., Murtugudde, R., and Lucas, L. E. (2003). Indo-Pacific Ocean response to atmospheric intraseasonal variability: 1. Austral summer and the Madden-Julian Oscillation. Journal of Geophysical Research-Oceans, 108(C5).

Waliser, D. E., Murtugudde, R., and Lucas, L. E. (2004). Indo-Pacific Ocean response to atmospheric intraseasonal variability: 2. Boreal summer and the Intraseasonal Oscillation. Journal of Geophysical Research-Oceans, 109(C3).

Wallcraft, A. J., Metzger, E. J., and Carroll, S. N. (2009). Software Design Description for the HYbrid Coordinate Ocean Model (HYCOM) Version 2.2. Technical Report NRL/MR/7320--09-9166, Naval Research Laboratory, Oceanography Division, Stennis Space Center, MS.

Wang, B. and Xie, X. S. (1997). A model for the boreal summer intraseasonal oscillation. Journal of the Atmospheric Sciences, 54(1):72--86.

Wang, B. and Xie, X. S. (1998). Coupled modes of the warm pool climate system. Part 1: The role of air-sea interaction in maintaining Madden-Julian Oscillation. Journal of Climate, 11(8):2116--2135.

Webster, P. J. (1983). Mechanisms of monsoon low-frequency variability - surface hydrological effects. Journal of the Atmospheric Sciences, 40(9):2110--2124.

Webster, P. J., Bradley, E. F., Fairall, C. W., Godfrey, J. S., Hacker, P., Houze, R. A., Lukas, R., Serra, Y., Hummon, J. M., Lawrence, T. D. M., Russell, C. A., Ryan, M. N., Sahami, K., and Zuidema, P. (2002). The JASMINE pilot study. Bulletin of the American Meteorological Society, 83(11):1603--1630.

Webster, P. J. and Hoyos, C. D. (2004). Prediction of monsoon rainfall and river discharge on 15-30-day time scales. Bulletin of the American Meteorological Society, 85(11):1745--+.

Webster, P. J., Moore, A. M., Loschnigg, J. P., and Leben, R. R. (1999). Coupled ocean-atmosphere dynamics in the Indian Ocean during 1997-98. Nature, 401(6751):356--360.

Wheeler, M. and Kiladis, G. N. (1999). Convectively coupled equatorial waves: Analysis of clouds and temperature in the wavenumber-frequency domain. Journal of the Atmospheric Sciences, 56(3):374--399.

Woodberry, K. E., Luther, M. E., and O'Brien, J. J. (1989). The wind-driven seasonal circulation in the southern tropical Indian Ocean. Journal of Geophysical Research, 94(17):17,985--18,002.

Woolnough, S. J., Slingo, J. M., and Hoskins, B. J. (2000). The relationship between convection and sea surface temperature on intraseasonal timescales. Journal of Climate, 13(12):2086--2104.

Woolnough, S. J., Slingo, J. M., and Hoskins, B. J. (2001). The organization of tropical convection by intraseasonal sea surface temperature anomalies. Quarterly Journal of the Royal Meteorological Society, 127(573):887--907.

Wyrtki, K. (1973). An equatorial jet in the Indian Ocean. Science, 181:262--264.

Xie, P. P. and Arkin, P. A. (1996). Analyses of global monthly precipitation using gauge observations, satellite estimates, and numerical model predictions. Journal of Climate, 9(4):840--858.

Yasunari, T. (1981). Structure of an Indian summer monsoon system with around 40-day period. Journal of the Meteorological Society Japan, 59:336--354.

Yu, L. S. and Rienecker, M. M. (2000). Indian Ocean warming of 1997-1998. Journal of Geophysical Research-Oceans, 105(C7):16923--16939.

Yuan, D. L. and Han, W. Q. (2006). Roles of equatorial waves and western boundary reflection in the seasonal circulation of the equatorial Indian Ocean. Journal of Physical Oceanography, 36(5):930--944.

Zavala-Garay, J., Zhang, C., Moore, A. M., and Kleeman, R. (2005). The linear response of ENSO to the Madden-Julian Oscillation. Journal of Climate, 18(13):2441--2459.

Zelle, H., Appeldoorn, G., Burgers, G., and van Oldenborgh, G. J. (2004). The relationship between sea surface temperature and thermocline depth in the eastern equatorial Pacific. Journal of Physical Oceanography, 34(3):643--655.

Zhang, Y. C., Rossow, W. B., Lacis, A. A., Oinas, V., and Mishchenko, M. I. (2004). Calculation of radiative fluxes from the surface to top of atmosphere based on ISCCP and other global data sets: Refinements of the radiative transfer model and the input data. Journal of Geophysical Research-Atmospheres, 109(D19).